Silicon-organic hybrid electro-optic modulators for high-speed communication systems

Zur Erlangung des akademischen Grades eines

DOKTORS DER INGENIEURWISSENSCHAFTEN
(Dr.-Ing.)

von der KIT-Fakultät für
Elektrotechnik und Informationstechnik
des Karlsruher Instituts für Technologie (KIT)

angenommene

DISSERTATION

von

Heiner Zwickel, M.Sc.
geb. in Lörrach

Tag der mündlichen Prüfung: 03.03.2020

Hauptreferent: Prof. Dr.-Ing. Christian Koos
Korreferent: Prof. Dr.-Ing. Dr. h. c. Wolfgang Freude
Korreferent: Prof. Dr.-Ing. Thomas Zwick

Table of contents

Kurzfassung v

Preface ix

Achievements of the present work xi

1 Introduction 1

2 Theoretical and technological background 7
- 2.1 Electro-optic interaction in silicon and hybrid silicon material systems 7
  - 2.1.1 Field-induced effects 8
  - 2.1.2 Carrier-induced effects 9
  - 2.1.3 Thermo-optic effect 11
  - 2.1.4 Hybrid silicon material systems 11
- 2.2 Principle of Mach-Zehnder and IQ modulators 16
  - 2.2.1 Push-pull operation 19
  - 2.2.2 IQ modulator 21
  - 2.2.3 Basic performance metrics for MZMs 22
- 2.3 Silicon-photonic Mach-Zehnder modulators: State of the art 27
- 2.4 SOH modulator device principles 34
- 2.5 Transmission-line-driven electro-optic modulators 39
  - 2.5.1 Electrical transmission lines 39
  - 2.5.2 Telegrapher equation and characteristic impedance . 40
  - 2.5.3 Matrix description of transmission line 42
  - 2.5.4 Voltage along a terminated lossy transmission line . 44
  - 2.5.5 Traveling-wave electro-optic modulators 46
- 2.6 Optical modulation formats for digital communications . . . 49

3 Model of traveling-wave SOH modulators **55**
3.1 Introduction 56
3.2 Device principle and model based on distributed-element equivalent circuit 58
3.3 Electrical characterization and fitting procedure 65
3.4 Measured and modeled electro-optic response 72
3.5 Design guidelines 75
3.5.1 Overcoming bandwidth limitations 75
3.5.2 Optimized doping profiles for low-loss modulators . 81
3.6 Summary 86
3.7 Mathematical relations for de-embedding the radio-frequency characteristics of on-chip modulators 88
3.8 Low-frequency characteristic impedance of a transmission line 89
3.9 Loss parameter of the RC element 90

4 SOH modulators for intensity-modulation/direct-detection links **93**
4.1 Introduction 94
4.2 Silicon-organic hybrid Mach-Zehnder modulators 97
4.3 Non-return-to-zero (NRZ) on-off keying (OOK) with an SOH MZM 100
4.4 Non-return-to-zero (NRZ) PAM4 signaling with an SOH MZM 103
4.5 Demonstration of three-level intensity-modulated duobinary (IDB) 105
4.6 Summary 107
4.7 Comparison of IM/DD modulation formats 108
4.8 Power consumption of SOH modulators 113

5 Packaging of SOH modulators **117**
5.1 Introduction 118
5.2 Concept, fabrication, and assembly 120
5.2.1 SOH Mach-Zehnder modulator 120
5.2.2 High-frequency PCB 122
5.2.3 Assembly 124
5.3 Optical, DC, and small-signal characterization of module . . 125

5.4 Intensity-modulated and coherent signaling 128
5.5 Summary 130

6 Summary and outlook 133

Bibliography 137

Glossary 157

Acknowledgements (German) 165

List of publications 169
Journal publications 169
Conference publications 171

Kurzfassung

Der Austausch von Informationen über globale Kommunikationsnetze ist für viele alltägliche Lebensbereiche selbstverständlich geworden. Die Informationen werden dabei mit immer weiter wachsender Geschwindigkeit und in zunehmendem Umfang geteilt. Durch den enormen Anstieg des Datenverkehrs kommt verstärkt optische Nachrichtentechnik zum Einsatz. Sie bietet gegenüber elektronischen Übertragungsverfahren entscheidende Vorteile bezüglich der Übertragungsdistanz und -kapazität. Wurde optische Übertragung zunächst nur für die Kommunikation über weite Strecken eingesetzt, machen sich die Nachteile elektronischer Verfahren mit dem stark anwachsenden Datenverkehr auch zunehmend über kürzere Strecken bemerkbar, sodass auch dort vermehrt optische Kommunikationssysteme zum Einsatz kommen. Insgesamt nimmt die Anzahl der photonischen Komponenten, die in Kommunikationsanwendungen eingesetzt werden, dadurch rapide zu. Dies führt dazu, dass die einzelnen Bauteile kostengünstiger, energieeffizienter sowie kompakter werden müssen. Ähnlich zur Entwicklung in der Mikroelektronik, wo immer stärkere Miniaturisierung zu einer dramatischen Leistungssteigerung bei gleichzeitiger Reduktion von Kosten, Platzbedarf und Energieverbrauch geführt hat, soll dies in der Photonik durch die Anwendung von integrierten photonischen Schaltkreisen erreicht werden.

Integrierte photonische Schaltkreise zeichnen sich durch hohe Funktionalität bei geringem Platzbedarf aus und ermöglichen eine kostengünstige Massenfertigung. Sie sind daher von erheblichem wissenschaftlichen, technischen und kommerziellen Interesse. Insbesondere die Integration auf Siliziumsubstraten verspricht dabei hohe Integrationsdichten, kombiniert mit der Möglichkeit zur Ko-Integration photonischer und elektronischer Schaltkreise. Ein entscheidender Vorteil ist dabei, dass Silizium seit Jahrzehnten das dominierende Material in der Halbleiterindustrie und eines der häufigsten Elemente der Erdkruste ist. Vorteilhaft ist also neben der guten Verfügbarkeit des Materials, insbesondere die Existenz von etablierten und zuverlässigen Prozessen aus der Mikroelektronik, speziell der CMOS-Fertigung, zur lithographischen Strukturierung. Zudem bietet Silizium viele für die integrierte Photonik günstige physikalische Eigenschaften. Beispielsweise die Transparenz im für die Datenübertragung technisch relevanten Spektralbereiche im Nahinfraroten zwischen 1260 nm und 1625 nm und einen hohen Brechungsindexkontrast zu Siliziumdioxid. Die unter dem Begriff Siliziumphotonik zusammengefasste Technologie ist daher eine vielversprechende Plattform für integrierte photonische Schaltkreise.

Eines der wichtigsten Bauteile in der optischen Nachrichtentechnik ist der elektro-optische (EO) Modulator. An der Schnittstelle zwischen Elektronik und Optik ist er das zentrale Element in optischen Sendern. Neben geringen Herstellungskosten, geringem Platzbedarf und guter Energieeffizienz ist eine hohe Modulationsgeschwindigkeit eine essentielle Fähigkeit des Modulators, da diese hohe Bandbreiten in der Datenübertragung ermöglicht.

Da Silizium aufgrund der punktsymmetrischen Kristallstruktur keine optische Nichtlinearität zweiter Ordnung aufweist, ist in reinem Silizium kein linearer EO Effekt (Pockels-Effekt) verfügbar. Elektro-optische Modulatoren aus Silizium basieren daher darauf, dass die Konzentration freier Ladungsträger in einem Siliziumwellenleiter moduliert wird, was beispielsweise durch Anlegen einer Spannung an einen pn-Übergang realisiert werden kann. Die Änderung der Konzentration freier Ladungsträger führt dabei zu einer Variation des optischen Brechungsindex (Plasmadispersions-Effekt). Dieser Effekt ist jedoch nicht effizient, wodurch die Energieeffizienz reiner Siliziummodulatoren insgesamt limitiert ist. Durch die heterogene Integration von Silizium mit weiteren Materialien lässt sich die Siliziumphotonik-Plattform erweitern. Organische EO Materialien lassen sich durch molekulares Design gezielt auf einen starken linearen EO Effekt hin optimieren. Durch die Kombination von Silizium-Nanowellenleitern und organischen EO Materialien lassen sich Hybridbauteile realisieren, welche wesentlich energieeffizienter als reine Siliziummodulatoren sind. In der englischsprachigen Fachliteratur werden diese Bauteile auch als *silicon-organic hybrid* (SOH) bezeichnet.

Die vorliegende Arbeit befasst sich mit SOH-Modulatoren und deren praktischer Anwendung in der optischen Hochgeschwindigkeitskommunikation. In vorausgehenden Arbeiten wurden die fundamentalen Prinzipien von SOH-Modulatoren untersucht und deren grundlegende Einsetzbarkeit für die optische Datenübertragung gezeigt. Die vorliegende Arbeit baut darauf auf und adressiert gezielt Aspekte, die für einen praktischen Einsatz von SOH-

Bauteilen in optischen Kommunikationssystemen von großer Bedeutung sind: Um ein zielgerichtetes Design der Bauteile zu ermöglichen und grundlegende Zielkonflikte im Design zu erkennen, wird ein Modell für das dynamische EO Verhalten der Modulatoren entwickelt und experimentell verifiziert. Für die breitbandige Aufbau- und Verbindungstechnik werden Konzepte zur elektrischen Anbindung schneller SOH-Modulatoren entwickelt und demonstriert. Verschiedene Modulationsformate werden bei Bruttodatenraten von bis zu 160 Gbit/s erfolgreich getestet und demonstrieren die Eignung von SOH-Modulatoren für praktische Anwendungsszenarien.

Kapitel 1 gibt eine kurze Einführung in das Gebiet der Siliziumphotonik und deren Bedeutung für die optische Datenübertragung.

Kapitel 2 beschreibt die theoretischen und technologischen Grundlagen elektrooptischer Bauteile auf Basis der Siliziumphotonik. Dies umfasst einen Überblick über den zugehörigen Stand der Wissenschaft und Technik sowie die für die nachfolgenden Kapitel relevanten Konzepte aus der Hochfrequenz- und der Nachrichtentechnik.

Kapitel 3 führt ein quantitatives Modell zur Beschreibung der dynamischen elektrischen und EO Eigenschaften von SOH-Modulatoren ein. Das Modell wird experimentell verifiziert und dient als Grundlage für verbesserte Bauteildesigns zukünftiger SOH-Modulatoren, mit denen sich Bandbreiten von mehr als 100 GHz und π-Spannungen von unter 1 V erreichen lassen.

Kapitel 4 demonstriert die Eignung von SOH-Modulatoren für technisch relevante Intensitätsmodulation/Direktempfang-Verfahren (engl. *intensity modulation/direct detection*, IM/DD), die insbesondere für hochgradig skalierbare Übertragungssysteme mit kleinen und mittleren Reichweiten (board-to-board, rack-to-rack) interessant sind. In diesem Zusammenhang werden verschiedene IM/DD-Modulationsformate experimentell getestet und dabei Bruttodatenraten von bis zu 120 Gbit/s demonstriert.

Kapitel 5 befasst sich mit der elektrischen Aufbau- und Verbindungstechnik für SOH-Modulatoren. Dies erfordert Platinen mit guten Hochfrequenzeigenschaften und kleinen Strukturgrößen, um eine hohe Integrationsdichte zu erreichen. Ein Verfahren zur Herstellung von hochfrequenztechnisch breitbandigen Keramikplatinen mit hoher räumlicher Auflösung wird vorgestellt. Mit Hilfe dieser Keramikplatinen wird ein mit Bonddrähten elektrisch angebundener

SOH-Modulator vorgestellt und damit eine Bruttodatenrate von 160 Gbit/s demonstriert.

Kapitel 6 fasst die vorliegende Arbeit zusammen und gibt einen Ausblick auf zukünftig notwendige Schritte, um die Anwendungsreife von SOH-Modulatoren zu erreichen. Zudem werden potentielle weitere Anwendungsfelder für SOH-Modulatoren diskutiert.

Preface

Information is exchanged at unprecedented speed and volume due to a growing number of users and data-hungry applications. This leads to an increasing use of optical communications because it offers advantages over electronic links in terms of transmission distance and bandwidth. The vast increase in the amount of data transmitted using optical communications leads to an enormous increase in the number of deployed photonic components. This demands low-cost and energy-efficient devices with small footprints. All these requirements are expected to be met by photonic integrated circuits (PICs).

Photonic integrated circuits realized on optical microchips offer many functionalities in a compact and cost-efficient way. In anticipation of mass production and scalability, silicon photonics (SiP) is considered to be particularly promising. Silicon has been the leading material in the semiconductor industry for decades and is one of the most abundant materials in the earth's crust. Mature fabrication technology developed for complementary metal-oxide-semiconductor (CMOS) microelectronics on silicon substrates offers large wafers and high yield, and can be used to structure photonic integrated circuits as well.

The electro-optic (EO) modulator is a key component for EO systems and in particular for optical communication as it translates signals from the electrical domain to the optical domain. All-silicon modulators suffer from the lack of a second-order optical nonlinearity in silicon which is required for a linear EO effect (Pockels effect). Therefore all-silicon EO modulators have to rely on the inefficient plasma-dispersion effect. This limits the energy efficiency of all-silicon EO modulators. To make silicon more versatile, additional materials can be heterogeneously integrated to the silicon platform. Combining organic EO materials with silicon structures in the so-called silicon-organic hybrid (SOH) integration approach enables high-speed, low-power EO modulators. The silicon base structure can be fabricated in highly standardized, reliable and scalable fabrication processes. The organic material can be molecularlyengineered to have a strong Pockels effect. This organic EO material can be added to the silicon structures in a simple post-processing step and enriches the silicon-platform by an efficient EO effect. SOH modulators exhibit excellent energy efficiency and small footprint and outperform all-silicon modulators.

Previous work has investigated fundamental principles of SOH modulators and demonstrated their basic usability for optical communication. This thesis builds upon this earlier work and addresses aspects that are specifically relevant for the use of SOH modulators in practical high-speed optical communication systems:

Chapter 1 gives a short introduction to the field of SiP and its relevance for optical communications.

Chapter 2 lays the theoretical and technological foundation for the following chapters and reviews the state of the art of silicon EO Mach-Zehnder modulators.

Chapter 3 introduces a quantitative model describing the dynamic electrical and EO behavior of SOH modulators. The model is experimentally verified. Design guidelines for future modulators with bandwidths of more than 100 GHz and π-voltages below 1 V are derived.

Chapter 4 demonstrates the suitability of SOH modulators for technically relevant intensity-modulation and direct-detection (IM/DD) systems that are of particular interest for mid-range and short-range communication. Various IM/DD formats are investigated, and line rates up to 120 Gbit/s are experimentally demonstrated.

Chapter 5 presents an electrical packaging concept for SOH modulators. This requires high-density printed circuit boards (PCBs) capable of transmitting high-speed radio frequency (RF) signals to interface the modulator. A manufacturing process for such PCBs based on a ceramic substrate is shown. An electrically packaged SOH modulator is demonstrated to operate at line rates up to 160 Gbit/s.

Chapter 6 summarizes the work in this thesis and outlines further steps in the development of SOH modulators for practical applications. Potential further application areas beyond traditional optical communication are briefly discussed.

Achievements of the present work

In this thesis, integrated electro-optic (EO) modulators on the silicon-organic hybrid (SOH) platform were investigated with a focus on aspects that are specifically relevant for the use of SOH modulators in practical high-speed optical communication systems. A reliable model describing the electro-optic behavior of SOH modulators quantitatively was developed and experimentally confirmed. The model allows to identify and to overcome device limitations and to design optimized transmission systems using SOH modulators. To realize technically simple, power-efficient and spectrally-efficient high-speed optical links, various intensity-modulation and direct-detection (IM/DD) formats were analyzed and experimentally demonstrated using SOH modulators. To improve the practical usability of the densely integrated modulators, a concept for electrical packaging was developed and demonstrated.

A concise overview of the major achievements is given in the following list:

- **Development and first experimental verification of a model of the EO behavior of SOH modulators:**
  A reliable quantitative model of SOH slot-waveguide modulators that accounts for the various bandwidth-limiting effects is formulated and experimentally verified, see Chapter 3, Section 3.2 to 3.4 [J1]. To the best of our knowledge, this work represents the first experimental validation of a general model of slot-waveguide modulators. This model allows deriving electro-optic properties from purely electrical measurements, which represents a key step towards fast and reliable wafer-level characterization of SOH modulators using standard wafer prober without the need for EO measurements.

- **Model-based optimization of SOH modulators and formulation of design guidelines for future devices with greatly improved performance:**
  The model allows identifying poorly designed doping profiles as the

main reason for a limited bandwidth. Guidelines for an optimized design, trading optical loss due to free-carrier absorption, for EO bandwidth, and for π-voltage are presented, see Chapter 3, Section 3.5 [J1]. Based on the model, future devices can be expected to be shorter than 1 mm while having π-voltages of less than 1 V and bandwidths of more than 100 GHz.

- **First demonstration of a data rate as high as 120 Gbit/s using IM/DD and SOH modulators:**
  Various IM/DD formats are demonstrated using SOH modulators. Using intensity-modulated duobinary (IDB) signaling allows to use the electrical bandwidth of a BiCMOS signal conditioning chip efficiently. A line rate of 100 Gbit/s is demonstrated using IDB, see Chapter 4, Section 4.5. This represents the first demonstration of signaling using SOH modulators without laboratory-style test and measurement equipment for signal generation. Further, using a high-speed arbitrary waveform generator (AWG), four-level pulse-amplitude modulation (PAM4) is demonstrated with a line rate of 120 Gbit/s [J2], see Chapter 4, Section 4.4 [J2].

- **Highest line rate achieved with a sub-millimeter Mach-Zehnder modulator (MZM) on the silicon photonic platform:**
  The line rate of 120 Gbit/s represented the highest data rate achieved with an MZM shorter than 1 mm on the silicon photonic platform [J2].

- **First demonstration of a broadband electrical packaging concept for densely integrated SOH modulators:**
  An electrical packaging concept enabling high-density radio frequency (RF) interfaces between on-chip SOH modulators and external circuits is demonstrated in a set of experiments. A fabrication process for high-resolution Al_2O_3 printed circuit boards (PCBs) is presented, see Chapter 5, Section 5.2.2 [J3].

- **Demonstration of the highest data rates achieved with wire-bond-based electrical silicon-photonic modulator package:**
  Using an electrically packaged SOH modulator, line rates (symbol rates) of 128 Gbit/s (64 GBd) using quadrature-phase-shift-keying (QPSK) modulation, and line rates (symbol rates) of 160 Gbit/s (40 GBd) using 16-state quadrature amplitude modulation (16QAM) are demonstrated, see Chapter 5, Section 5.4. This is among the highest symbol and line

rates demonstrated so far with electrically-packaged silicon-photonic modulators (including technically complex flip-chip approaches rather than wire bonding). It represents the highest symbol rate of published signaling demonstrations using a silicon-photonic modulator packaged with wire bonds [J3].

1 Introduction

The exchange of information across global communication networks at unprecedented speed and volume is essential in almost every aspect of our life. Information is generated and shared virtually instantaneously, and the number of devices actively contributing to data traffic is growing vastly [1]. The communication networks spanning the entire globe were enabled by a series of groundbreaking technological innovations. Most important was the invention of silica glass fibers in the 1970s[1] that offer low signal attenuation of approximately 0.2 dB/km at the telecom wavelengths around 1.55 µm [5] and tens of THz of bandwidth. Stable operation of semiconductor lasers at room temperature was realized in the 1980s [6, 7]. In addition, the maturity of erbium-doped fiber amplifiers (EDFAs)[2], reached in the 1990s [8], enabled scaling of the network reach and capacity by supporting long-distance fiber connections and wavelength-division multiplexing (WDM).

Already at the time those innovations happened, photonic integration was perceived as the next technological innovation [9, 10] with the potential to fundamentally change not only optical communications but the entire field of photonics – much like electronic integration has changed the way we generate, compute and store digital data. The transformative power of photonic integrated circuits (PICs) lies in the potential to offer more and more functionality in a compact and cost-efficient way, with the potential for scalability and mass production, in analogy to Moore's law in microelectronics [11].

---

[1] In 1966 Kao *et al.* suggested that losses of optical fibers could be reduced drastically by removing impurities from silica glass [2]. He was awarded the 2009 Nobel Prize in Physics [3]. In the following years many industrial laboratories (most prominently CORNING) successfully reduced optical losses [4, 5].

[2] EDFAs are good for broadband amplification in the optical C-band from 1535 nm to 1564 nm, corresponding to 4 THz bandwidth

However, in the early years, the internet and therefore the requirements for hardware looked different. Web pages were static and only a very limited number of devices was connected to the internet. Optical communication was almost exclusively used for long-distance transmission where higher cost and bulky devices could be tolerated. Shorter communication links were still realized using electrical transmission lines and as a result the demand for PICs was limited. In addition, technological limitations led only to a slow increase in integration density and to a fragmentation in application specific material platforms. Oftentimes, a particular technology could only be used to build one specific component. Till today, the light sources still need direct-bandgap III-V semiconductors. This made the III-V material InP the most complete platform for photonic integration, offering passive components as well as lasers, detectors and electro-optic (EO) modulators. Complex PICs with more than 50 elementary photonic components integrated on a chip were presented as a commercial product by INFINERA in 2005 [12]. However, the integration density is many orders of magnitude smaller than what is achieved in current generation electronic integrated circuits (EICs) with e.g. 18 billion elementary elements, the transistors, in a central processing unit (CPU)[3]. The technologically complex epitaxial growth process and the small wafer size are often mentioned as the main obstacle for the scalability and the yield of the InP platform and hinder the co-integration with complementary metal-oxide-semiconductor (CMOS) electronics which is based on Si substrates.

However, the desire for a scalable photonic integration platform and the demand for low-cost PICs is growing. With the evolution of the internet from a network with static web pages and passive end-users to the modern web with cloud services, user-adapted dynamic web pages, video streaming, 5G networks, and internet of things (IoT), the bandwidth requirements increased rapidly, in particular for short-reach links. Nowadays, service providers like, e.g., GOOGLE, FACEBOOK, AMAZON or ALIBABA operate warehouse-scale data centers, and about 70% of the global data center traffic remains within data centers [13]. All this requires an enormous amount of deployed photonic components, in particular for short transmission spans, so that cost, footprint and energy-consumption of the devices become even more crucial.

---

[3] QUALCOMMS Centriq processor, based on SAMSUNGS 10 nm FinFET process has 18 billion transistors on 398 mm^2.

Leveraging the mature CMOS processes, initially developed for microelectronics, photonic structures on the silicon platform can be realized. This comes with a number of outstanding advantages that lead eventually to low-cost mass-production of high-speed, energy-efficient PICs. The high refractive index contrast between Si and SiO_2 allows extremely compact waveguides and high integration densities [14]. The transparency at telecom wavelengths makes silicon a perfect material for optical communication devices. Most importantly, due to the sophisticated process control of CMOS manufacturing, PICs can be fabricated with high yield on large wafers. Large wafers and high yield are ultimately related to low manufacturing costs. Additionally, standardized processes enable so-called “fab-less” approaches where device development and design is decoupled from the fabrication. The fabrication is done in a few large, highly-developed foundries. Strictly defined design and process parameters guarantee reliable quality and allow to provide libraries of read-to-used devices. A broad spectrum of applications can be covered with one single platform allowing to overcome the fragmentation into application-specific technologies which cannot be consolidated.

Silicon-Photonics (SiP) was predicted to achieve the necessary technical breakthroughs and become an economic success for a long time [10, 15]. But only in recent years silicon PICs have finally transitioned from a pure research topic to commercially deployed products with both, well established companies and start-ups, bringing products to the market[4]. Two major drawbacks of silicon make it hard to implement SiP as a complete photonic platform and might have slowed down commercial exploitation: First, the indirect bandgap of silicon does not allow light emission. Second, silicon does not show a linear EO effect (Pockels effect) because the centro-symmetric crystal structure leads to a vanishing second-order optical nonlinearity. The linear EO effect, however, is favorable for efficient control and manipulation of light. This deficiency makes it hard to build high-speed and energy-efficient EO modulators in silicon which are key elements in optical communication systems where an increasing level of sophistication is used to encode information onto light. To bypass the lack of a Pockels effect, EO modulation in silicon is most commonly achieved by the plasma-dispersion effect [16], which is inherently limited in its efficiency.

---

[4] e.g. INTEL, TERAXION, LUMENTUM, KAIAM, LUXTERA, ACACIA and AYARLABS

To make silicon more versatile, additional materials can be heterogeneously integrated on the silicon platform [17]. Bonding III-V materials, ferro-electric Perovskites or graphene adds efficient EO activity to the silicon platform but requires major modifications to the fabrication process. Cladding silicon waveguides with highly-efficient, chemically-engineered organic EO materials in a back-end-of-line (BEOL) process, however, requires no modifications of the fabrication process. This so-called silicon-organic hybrid (SOH) approach allows increasing the efficiency of the modulator by an order of magnitude compared to conventional high-speed SiP modulators based on the plasma dispersion effect [18]. SOH modulators can be combined with the full portfolio of SiP components available in commercial fabrication runs[5]. High-speed SOH modulators with sub-millimeter device lengths were previously demonstrated to offer line rates of 100 Gbit/s using on-off-keying (OOK) modulation and up to 400 Gbit/s using 16QAM [19] in laboratory experiments. Recent progress in the stability of organic EO materials in SOH modulators [20, 21] makes them a promising candidate for power-efficient, high-speed integrated modulators.

However, several aspects that are specifically relevant for the use of SOH modulators in high-speed optical communication systems still need to be investigated. A reliable and experimentally verified model describing the SOH modulator is still missing. High-speed signaling demonstrations were so far based on laboratory-style test and measurement equipment rather than electronic integrated circuits (ICs) that could be integrated with the modulator. Further, there is no practical solution for electrical packaging of densely integrated SOH modulators available. The work in this thesis addresses these aspects concerning SOH modulators that are crucial for further development of the devices and to ensure their compatibility with practical application scenarios.

In Chapter 2 the theoretical and technological background is covered with an overview of EO effects in silicon and hybrid silicon systems, followed by a brief review of state-of-the-art silicon EO Mach-Zehnder modulators (MZMs). In addition, physical and mathematical relations required in the following chapters are introduced. In Chapter 3 a full model, describing the electrical and EO

---

[5] Typically available components in SiP comprise active components such as modulators and SiGe photodiodes as well as a number of passive structures such as waveguides, splitters, filter, and fiber coupling structures.

behavior of the SOH modulator is derived and experimentally verified. The model allows identifying the key device limitations and to formulate design guidelines for optimized performance with respect to bandwidth, operation voltage, and optical insertion loss. Experimentally verified quantitative models are also essential for the design and the optimization of advanced transceiver systems where driver circuits and modulators have to be considered jointly to achieve best system performance. Further, the model allows deriving EO properties from purely electrical measurements, which is advantageous for wafer level characterization using standard wafer prober. In Chapter 4 the efficiency of the total transmission system is considered. To reduce the overall complexity, intensity-modulation and direct-detection (IM/DD) formats with high spectral efficiency are considered to allow the use of low-cost electronics while maintaining a high data rate. Various IM/DD formats are investigated, both theoretically and experimentally. Finally, the high integration density of SOH modulators is a challenge for broadband electrical packaging, which is investigated in Chapter 5. An electrical packaging concept that enables high-density radio frequency (RF) interfaces between on-chip SOH devices and external circuits is presented. This concept combines high-resolution Al_2O_3 printed-circuit boards with technically simple metal wire bonds. It is validated in a set of experimental demonstrations including high-speed signaling.

2 Theoretical and technological background

This chapter covers the technological and theoretical background as well as some physical relations and their mathematical representation. It is structured as follows: In Section 2.1 the various interactions between electrical and optical signals in Si are introduced, and their usability to build electro-optic (EO) modulators is discussed. To overcome limitations of pure Si, it can be combined with additional materials. These hybrid material systems are discussed as well with special emphasis on organic EO materials. In Section 2.2 the principles of Mach-Zehnder modulators (MZMs) and in-phase/quadrature-phase (IQ)-modulators are presented along with relevant quality metrics for MZMs. Section 2.3 gives an overview of the state-of-the-art of silicon photonics (SiP) MZMs. In Section 2.4 the concept of SOH modulators is introduced eventually. Section 2.5 covers relevant concepts of microwave engineering and the required mathematical representations to model SOH modulators. Finally, Section 2.6 gives a short summary of modulation formats used for optical communications.

2.1 Electro-optic interaction in silicon and hybrid silicon material systems

Silicon offers a number of advantageous properties to realize photonic integrated circuits (PICs). Most importantly the bandgap of 1.12 eV [22] makes silicon transparent at the telecom wavelengths around 1.55 µm and 1.3 µm. In addition, the high refractive-index contrast of silicon with its oxide leads to compact waveguides with small bending radii and is hence important for dense integration [14]. Further, the advanced manufacturing technologies from the CMOS microelectronics industry allow cost-efficient and scalable production as well as co-integration with electronic circuits [15, 23–25]. However, due to its centro-symmetric crystal structure, Si lacks a second-order nonlinearity and therefore does not exhibit a linear EO effect (Pockels effect) [26], which is typically used in traditional EO phase modulators and Mach-Zehnder devices made e.g. from $LiNbO_3$. Consequently, silicon-based devices that exploit interaction of electrical and optical signals in silicon have to rely on other interaction mechanisms [27]. The following list gives a brief overview of the physical mechanisms that allow to influence the refractive index (electro-refraction) or the absorption (electro-absorption) by means of an applied voltage or current. Absorption and refraction are intrinsically linked by the Kramers-Kronig relation [26]. This allows us to first consider how the absorption spectrum of silicon is affected by a particular physical effect. In a second step, the influence on the real part of the refractive index can then be derived using Kramers-Kronig relations. A phase modulation which is achieved by manipulation of the real part of the refractive index can always be converted into amplitude or intensity modulation by using an interferometric or resonant scheme, see Section 2.3.

Subsection 2.1.1 to Subsection 2.1.3 discuss the EO interaction available in pure Si. Subsection 2.1.4 discusses the effects that become available if Si is combined with addition materials.

2.1.1 Field-induced effects

Field effects are generally preferred for EO modulators because they can be used with negligible or very small current flow leading to small energy consumption in practical devices.

- **Franz-Keldysh effect:** If an external electric field is applied to a bulk semiconductor, the band edges become spatially tilted. This perturbation in the band diagram allows tunneling of carriers between valence and conduction band states. The wavefunctions of electrons leak into the bandgap. Photons with energies below the bandgap energy then have a non-vanishing probability for being absorbed and the effective bandgap is reduced. The absorption spectrum is red-shifted [28]. However, the Franz-Keldysh effect in Si is weak and does not contribute significantly to electro-optic modulation in Si modulators [27, 29].

- **Electro-optic Kerr effect:** Crystalline silicon exhibits a third-order optical nonlinearity. This leads to a quadratic electro-optic effect where the optical refractive index can be modified by an external electric field. The change in refractive index is proportional to the external field squared [26]. The Kerr effect is weak and listed here for completeness. It cannot be used for practical electro-optic modulators.

- **Pockels effect:** As discussed above, the centro-symmetry of crystalline silicon in its natural state leads to a vanishing second-order susceptibility, and therefore silicon does not exhibit a Pockels-effect. Special fabrication techniques, however, can induce strain in the Si crystal, typically by deposition of a SiN layer onto the Si layer [30]. The induced stress due to crystal lattice mismatch breaks the centro-symmetry and thus strained silicon systems can exhibit a Pockels effect [31]. The strength of the strain induced Pockels effect is still subject of ongoing investigations [31] and too small for practical modulators.

2.1.2 Carrier-induced effects

The effects listed below contribute to the dependence of the absorption spectrum on the concentration of free carriers present in Si. Due to the Kramers-Kronig relation, also the real part of the refractive index is affected by a change in the absorption spectrum.

- **Free-carrier absorption:** If free carriers are present in Si, they can be exited to higher energy states by absorption of a photon. The probability for absorption of a photon depends on the density of free carriers and thus the absorption spectrum depends on the density of free carriers. This effect has the strongest contribution to the interaction between electrical and optical signals in state-of-the-art Si modulators, see Section 2.3.

- **Burstein-Moss-band-filling:** Electrons in energy states in the valence band can be exited into higher energy states in the conduction band if they absorb a photon with energy larger than the bandgap energy. For such an electronic transition to happen, the respective energy state in the conduction band has to be unoccupied. The excited electrons relax into lower-energy states in the conduction band and fill the energy states close to the band edge first. Therefore, photon energies higher than the band gap energy are required for further electronic transitions in the presence of free carriers. The absorption spectrum is blue-shifted.

- **Coulomb interaction:** The free carriers present in a semiconductor interact due to the Coulomb force between the charged carriers [32]. In addition, free carriers interact with impurities. The strength of these interactions depends on the carrier concentration and affects the absorption spectrum. Therefore, a modification of the carrier concentration directly changes the absorption spectrum. Soref and Bennett show that the interaction of free carriers with impurities is most relevant and leads to a red shift of the absorption spectrum [27].

Changes in the absorption in a semiconductor due to free-carrier absorption can be described by a Drude-Lorenz model [33]. For a vacuum wavelength λ_0, the change in refraction Δn and in absorption $\Delta\alpha^{(\mathrm{pwr})}$ due to a change ΔN_e in the free electron concentration N_e and a change ΔN_h in the free hole concentration N_h is given by [27]

$$\Delta n = -\frac{\mathrm{e}^2\lambda_0^2}{8\pi^2\mathrm{c}^2\epsilon_0 n}\left(\frac{\Delta N_\mathrm{e}}{m_\mathrm{e}^*} + \frac{\Delta N_\mathrm{h}}{m_\mathrm{h}^*}\right) \tag{2.1}$$

and

$$\Delta\alpha^{(\mathrm{pwr})} = \frac{\mathrm{e}^3\lambda_0^2}{4\pi^2\mathrm{c}^3\epsilon_0 n}\left(\frac{\Delta N_\mathrm{e}}{m_\mathrm{e}^{*2}\mu_\mathrm{e}} + \frac{\Delta N_\mathrm{h}}{m_\mathrm{h}^{*2}\mu_\mathrm{h}}\right), \tag{2.2}$$

with m_e^* and m_h^* being the electron and hole conductivity effective masses and μ_e and μ_h being the electron and hole mobility. Note that $\alpha^{(\mathrm{pwr})}$ is the absorption parameter for power. Soref and Bennett further studied experimental absorption curves and empirically derived correction factors that need to be applied to Eq. 2.1 and 2.2 to take all carrier-induced effects (free-carrier absorption, band-filling, and Coulomb interactions) on refraction and absorption into account [27]. The empirical equation is in good agreement with the Drude-Lorenz model and is widely used to model carrier-induced EO effects in Si [29]. The simple Drude-Lorenz model, see Eq. 2.1 and Eq. 2.2, is therefore sufficient to describe the qualitative dependencies of absorption and refraction on the density, the conductivity effective mass, and the mobility of the carriers in Si [16]. The combination of all carrier-induced effects is often referred to as **plasma-dispersion effect**. In Si EO modulators, carrier injection, carrier removal or carrier depletion is typically exploited (e.g., in pn-junctions or silicon-insulator-silicon (SIS)-structures, see Section 2.3) to manipulate the absorption and the refractive index inside an optical waveguide.

2.1.3 Thermo-optic effect

Silicon shows a very strong thermo-optic effect (the refractive index depends heavily on the temperature), which can be exploited for achieving electro-optic interactions by electrical heating of silicon [29]. However, the thermo-optic effect is slow and unsuitable for realizing high-speed EO modulators [29]. Additionally, it can be difficult to reach a localized heating and to maintain a power efficient operation of electro-optic modulators based on the thermo-electric effect.

2.1.4 Hybrid silicon material systems

To overcome the inherent limitation of Si, it can be combined with additional materials providing e.g. a second-order optical nonlinearity. Preferably, a material with very high EO efficiency is chosen along with an integration process that preserves most of the advantages of standard silicon-photonic processes. Promising candidates for silicon-hybrid integration are:

- **Inorganic dielectric crystals:** $LiNbO_3$ has been the most widely used material for conventional EO modulators for decades [34]. It exhibits a large second-order nonlinearity but is difficult to process, and the fabrication of micro-structured devices is hardly possible [34]. Typically ion indiffusion or proton-exchange is used to form optical waveguides in the crystalline material [34, 35]. In recent years, thin films of $LiNbO_3$ have been successfully bonded to silicon dioxide substrates leading to compact and efficient EO modulators that could potentially be integrated into a silicon photonic process [36]. In contrast to $LiNbO_3$, the material barium titanate (BTO, chem. $BaTi0_3$) can be epitaxially grown on silicon substrates [37]. Due to the extremely high EO coefficient of BTO [38], it has emerged as a promising candidate for integrated high-performance

Si hybrid modulators [39], see Section 2.3, but the fabrication is not compatible with standard SiP processes.

- **III-V semiconductors:** While III-V materials like GaAs or InP are typically used as a monolithic platform to realize EO modulators on InP or GaAs substrates [40,41], they can also be used in hybrid silicon systems. Hybrid III-V-silicon systems can either use Si substrates and waveguides while the entire EO activity is provided by III-V structures [42]. In this case, the EO activity in III-V materials often originates in a strong Franz-Keldysh effect. Alternatively, on one side of a p-doped-intrinsic-n-doped (PIN) modulator or a silicon-insulator-silicon capacitor (SISCAP) modulator, the doped silicon is replaced by a III-V material [43], see Section 2.3.

- **Organic EO materials:** Organic EO materials can either be liquid crystalline (LC) materials or organic chromophores. Liquid crystals show a large EO effect and can be integrated with silicon waveguides to form EO modulators [44, 45], but the response time is slow because of the collective molecular mass that needs to be moved [46]. A significant increase in response-time can be achieved with organic EO chromophores. The individual chromophore consists of a donor group and an acceptor group linked by a π-conjugate bridge. Exposed to an external varying E-field, the chromophore has a response time limited only by the phase-relaxation time of the π-electron system which is in the order of ten femtoseconds [46]. This allows in principle tens of THz EO bandwidths. Modern organic EO materials reach bulk EO coefficients of $r_{33} = 550\,\mathrm{pm/V}$ [47] and can be combined with silicon waveguides to form silicon-organic hybrid (SOH) devices [48–51]. SOH integration using chromophore-based EO materials is the approach used throughout this thesis. This class of organic EO materials is therefore introduced in more detail. The following paragraph is based on references [46, 52] and [53].

  EO chromophores can either be embedded in a host material or attached to a polymer backbone to form a polymer composite material [54]. Alternatively, they can be used as high number density neat (pure) chromophore material [48]. In any case, essential for the EO activity is the existence of a donor and acceptor group in the chromophore and electron transfer between these groups to form a molecular dipole [53]. The molecular dipole moment **p** reacts to an external electric field **E** and can be expressed in simplified notation for complex time-domain amplitudes (using Einstein notation) as

$$p_i = \check{\mu}_i + \check{\alpha}_{ij} E_j + \check{\beta}_{ijk} E_j E_k + \ldots, \tag{2.3}$$

see Eq. (2.22) in [53], where $\check{\mu}$ is the electric dipole moment, $\check{\alpha}$ the first-order polarizability and $\check{\beta}$ the second-order polarizability or first order hyperpolarizability [46]. The indices $i, j, k = \{x, y, z\}$ denote the three orthogonal axes in a Cartesian coordinate system. The second-order optical nonlinearity originates from the first order hyperpolarizability $\check{\beta}$ [53]. For most chromophores in second-order nonlinear organic materials the component $\check{\beta}_{zzz}$ is dominant in a coordinate system where the z-direction is aligned with the dipole symmetry axis of the chromophore molecule. If all other components of $\check{\beta}$ are assumed to be negligible, the hyperpolarizability can be related to the macroscopic second-order susceptibility $\chi^{(2)}_{333}$ by [46]

$$\chi^{(2)}_{333} = N \check{\beta}_{zzz} \langle \cos^3 \theta \rangle g. \tag{2.4}$$

Besides the intrinsic microscopic nonlinearity of the molecules $\check{\beta}$, the macroscopic nonlinearity $\chi^{(2)}$ depends on the number density N of the active molecules ($[N]$ = molecules/cm^3), and on their average acentric order, described by the order parameter $\langle \cos^3 \theta \rangle$, with θ being the angle between the z-direction in the molecular system and an external laboratory reference system. The operator $\langle \rangle$ symbolizes an ensemble average over all chromophores. If the chromophores are completely randomly oriented, the order parameter is zero and the contributions of the individual chromophores cancel out. If the chromophores have an acentric order, a net contribution remains, thus leading a non-vanishing $\chi^{(2)}$. The so-called Lorentz-Onsager local field factor g is introduced to rescale the external field which is partially screened by charges in the organic EO material.

The second-order susceptibility $\chi^{(2)}_{333}$ is linked to the widely used EO coefficient r_{333} by [26]

$$r_{333} = -2 \frac{\chi^{(2)}_{333}}{n_0^4}, \tag{2.5}$$

with the refractive index n_0 of the EO material along the z-direction. Exploiting the symmetry of the second-rank tensor r_{ijk} we can introduce a contracted notation [26] reducing the number of subscripts to two and write the relevant component r_{333} as r_{33}. The EO coefficient r_{33} of the organic chromophore EO material can then be written as

$$r_{33} = -2N\check{\beta}_{zzz}\langle\cos^3\theta\rangle g/n_0^4. \tag{2.6}$$

The macroscopic EO activity of the organic materials can be improved by enhancing the hyperpolarizability $\check{\beta}$ of the constituting chromophores, by increasing the number density of chromophores N in the material, and by increasing their orientational order $\langle\cos^3\theta\rangle$. The latter is a crucial step in preparing organic EO materials as the thermodynamically favored state of the chromophore ensemble is a centric order, where the molecular dipole moments chancel out and the energy is therefore minimized [46]. This. however, would leave the material with vanishing net bulk EO activity. To bring the chromophores into an acentric order the material must be poled [46,48,49,52,53]. While exposed to an elevated temperature, the chromophores become mobile and align according to an external electric poling field. To prevent relaxation back into centric order, the material is cooled down while maintaining the poling field. Optimization of the parameters of the poling process, like the poling temperature, or the poling time is one of the central engineering tasks in improving device performance of SOH modulators [18,48,55,56]. It remains a challenge to prevent the relaxation of the chromophore orientation back in to their energetically favorable state. This thermal relaxation reduces device reliability and stability. The thermal relaxation can be slowed down by designing material systems with high glass-transition temperature T_g or by employing techniques like cross-linking to permanently fix the chromophore orientation in a polymer matrix. For experiments presented in the following chapters, two organic EO material systems optimized for thermal stability were used:

Organic EO guest-host system material family SEO: For the experiments reported in Chapter 4 and 5 the commercially available organic EO materials SEO100 and SEO250 (sold by Soluxra, LLC) were used [57,58]. Both SEO materials are guest-host systems comprising amorphous polycarbonate and EO chromophores. The composite of

SEO100 has a glass transition temperature T_g around 140°C, low optical loss and is specified for stable operation at 85°C [57]. The EO coefficient can be as high as 200 pm/V at a wavelength of 1310 nm [57] (144 pm/V at 1550 nm). Using SEO100, high-speed operation of an SOH modulator at 80°C was shown in [21]. SEO250 has the same T_g as SEO100 and while the nominal r_{33} is slightly higher than for SEO100, the material shows very similar EO efficiencies in SOH modulators.

Organic EO sidechain polymer material: For the experiments in Chapter 3, a side-chain EO material was used [20, 54, 59]. The material is based on a methyl methacrylate (MMA) polymer backbone. Two functional side groups are attached to the backbone [20]: a bulky adamantyl side group which makes the polymer chain less mobile and thus increases T_g, and a sidegroup containing a phenyl vinylene thiophene (PVT) chromophore that provides the EO activity. Due to the adamantyl side group the material exhibits a high T_g of 172°C which can be even further increased to 194°C with a slightly reduced EO activity [60]. This material was used to demonstrate long-term thermally stable SOH modulators in accordance with Telcordia standards [61] for high-temperature storage [20]. In high-temperature storage experiments at 85°C the electro-optic activity converged to a constant long-term stable level after an initial decay. Considering a burn-in time of 300 h, the efficiency of the SOH modulator decreased by less than 15% over the following 2400 h.

In earlier work [18] the highly efficient **organic EO neat chromophore material JRD1** [47, 48] was used in SOH modulators resulting in ultra high EO in-device efficiencies. JRD1 is the result of theory-guided optimization of EO chromophores [48]. The chromophore features bulky phenyl side groups which significantly increase the intermolecular distance of neighboring chromophores. This in turn reduces the dipole-dipole interactions between chromophores, and JRD1 chromophores can be used in high number densities without a polymer host. This leads to a high $\check{\beta}$ and bulk EO coefficients of $r_{33} = 550\,\mathrm{pm/V}$ [47]. However, these materials do not yet offer sufficient thermal stability for practically viable devices, and in this work, the more stable materials SEO100, SEO250 and the side-chain material with polymer backbone were used.

In addition to reversible thermal relaxation, irreversible photo-oxidation can degrade EO materials. This so-called photobleaching is triggered by optical absorption and subsequent chemical reaction with oxygen [62]. While typical organic EO materials have a low absorption at the telecom wavelength of around 1550 nm, the high optical intensities present in nano waveguides and in particular in the nano-slot waveguides used in SOH modulators, see Section 2.4, lead to two-photon absorption (TPA) and consequently to photobleaching if oxygen is present. Improvements in both, thermal stability and photo stability, are subject to ongoing research. It is expected that techniques like cross-linking and hermetic sealing can greatly improve the reliability of organic EO materials.

2.2 Principle of Mach-Zehnder and IQ modulators

Electro-optic modulators are key elements in optical communication systems. EO modulation can be realized either by direct absorption or by phase modulation. Modulators comprising embedded phase shifters are capable of supporting intensity modulation and complex-valued modulation formats. By exploiting interferometric or resonant structures, modulators based on phase shifters can transform a modulation of the phase into a modulation of the amplitude or intensity of the optical carrier. The present section limits itself to Mach-Zehnder modulators (MZMs) as this type of modulator generally supports complex modulation formats, broadband operation in terms of the optical carrier frequency, and broadband operation in terms of the modulating RF signal.

An MZM is an interferometric modulator structure based on interference and modulation of the refractive index [35]. The schematic of an MZM is depicted in Fig. 2.1(a). A monochromatic, coherent, linearly polarized optical carrier as input signal is split into two parallel paths, the two arms of the MZM, and then recombined to form the output signal. In the two arms of the interferometer a phase shift is introduced by modulation of the refractive index n in the active section of length ℓ. In MZMs the refractive index can be manipulated by a control voltage u_S. The equivalent of this scheme as implemented in a PIC is depicted in Fig 2.1(b). The incoming light is split by a multi-mode-

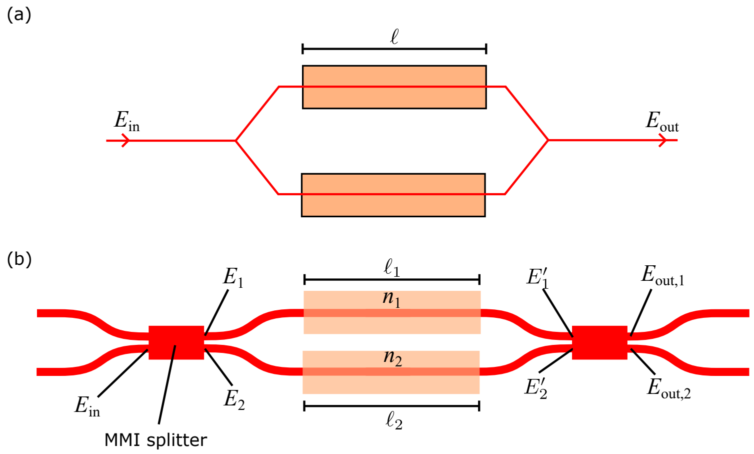

Fig. 2.1: Modulation of an optical carrier based on a Mach-Zehnder interferometer (MZI) (a) Schematic of an Mach-Zehnder modulator (MZM). The input signal is split into two arms where the phase is manipulated by controlling the refractive index along an interaction length ℓ. When the two signals are recombined they interfere and form the output signal. (b) Implementation of an MZM in a photonic integrated circuit (PIC). The light is split and recombined by multi-mode-interference (MMI) splitters. The phase in each arm is adjusted by manipulating the effective refractive index in a section of the integrated waveguide.

interference (MMI) coupler [35, 63], propagates in two parallel waveguides with adjustable effective refractive index and is recombined by a second MMI coupler. The SOH modulators used in this work are derived from this scheme, see Section 2.4.

We will now derive an expression for the optical signal at the output ports of the MZM. In the following we use complex representations of the electric field E such that the actual, real-valued field can be derived as $\Re\{E\}$. The input signal directly at the input of the MMI coupler oscillates with the angular frequency ω and is given by $E_{\text{in}} = E_0 \exp(\mathrm{j}\omega t)$. This input signal is split into the two arms of the MZM. Assuming a 1-to-1 splitting ratio for the MMI ("50:50-splitter"), the field at the output of the MMI coupler in the upper arm is given by

$$E_1 = \frac{1}{\sqrt{2}} E_{\text{in}} \exp(-\mathrm{j}\pi/2) \tag{2.7}$$

and for the lower arm by

$$E_2 = \frac{1}{\sqrt{2}} E_{\mathrm{in}}. \tag{2.8}$$

The additional phase of $-\pi/2$ of the signal in the upper arm is caused by the cross transition of the MMI [35]. After propagation through the phase modulator PM1 and PM2 the signal accumulates a phase φ_i given by $\varphi_i = -(2\pi/\lambda_0)n_i\ell_i$ with $i = 1, 2$ indicating path 1 and 2 respectively and λ_0 being the vacuum wavelength of the carrier. Additional phase shifts that accumulate during propagation in both arms and do not lead to a relative phase difference between the signals in arm 1 and arm 2 are omitted. The optical signals in the arms before recombination (at the inputs of the second MMI coupler) can then be written as

$$E_1' = \frac{1}{\sqrt{2}} E_{\mathrm{in}} \mathrm{e}^{-\mathrm{j}\pi/2} \mathrm{e}^{\mathrm{j}\varphi_1} \tag{2.9}$$

and

$$E_2' = \frac{1}{\sqrt{2}} E_{\mathrm{in}} \mathrm{e}^{\mathrm{j}\varphi_2} \tag{2.10}$$

The output signals at the two output ports 1 and 2 are given by

$$E_{\mathrm{out},1} = \frac{1}{\sqrt{2}} E_1' + \mathrm{e}^{-\mathrm{j}\pi/2} \frac{1}{\sqrt{2}} E_2' = \frac{1}{2} \mathrm{e}^{-\mathrm{j}\pi/2} E_{\mathrm{in}} \left[\mathrm{e}^{\mathrm{j}\varphi_1} + \mathrm{e}^{\mathrm{j}\varphi_2}\right] \tag{2.11}$$

and

$$E_{\mathrm{out},2} = \frac{1}{\sqrt{2}} \mathrm{e}^{-\mathrm{j}\pi/2} E_1' + \frac{1}{\sqrt{2}} E_2' = \frac{1}{2} E_{\mathrm{in}} \left[-\mathrm{e}^{\mathrm{j}\varphi_1} + \mathrm{e}^{\mathrm{j}\varphi_2}\right]. \tag{2.12}$$

By defining the relative phase difference $\Delta\varphi = \varphi_2 - \varphi_1$ and omitting global phase factors we can rewrite the output fields as

$$E_{\mathrm{out},1} = \frac{1}{2} E_{\mathrm{in}} \mathrm{e}^{\mathrm{j}\frac{\varphi_1+\varphi_2}{2}} \left[\mathrm{e}^{\mathrm{j}\frac{\Delta\varphi}{2}} + \mathrm{e}^{-\mathrm{j}\frac{\Delta\varphi}{2}}\right] = E_{\mathrm{in}} \mathrm{e}^{\mathrm{j}\frac{\varphi_1+\varphi_2}{2}} \cos\left(\frac{\Delta\varphi}{2}\right) \tag{2.13}$$

and

$$E_{\mathrm{out},2} = \frac{1}{2} E_{\mathrm{in}} \mathrm{e}^{\mathrm{j}\frac{\varphi_1+\varphi_2}{2}} \left[\mathrm{e}^{\mathrm{j}\frac{\Delta\varphi}{2}} - \mathrm{e}^{-\mathrm{j}\frac{\Delta\varphi}{2}}\right] = E_{\mathrm{in}} \mathrm{e}^{\mathrm{j}\frac{\varphi_1+\varphi_2}{2}} \sin\left(\frac{\Delta\varphi}{2}\right). \tag{2.14}$$

With the relation given by Eq. 2.13, the output field E_{out} can in principle reach any point in the complex plane by adjusting the phases φ_1 and φ_2. In practical modulators, however, where the phases are typically controlled by a voltage, it is more convenient to use the MZM in so-called push-pull operation mode for pure intensity modulation or pure amplitude modulation. If complex-valued output fields are required it is more convenient to configure an optical IQ modulator based on two nested child MZM. The concept of push-pull operation and of optical IQ modulators are briefly introduced in Section 2.2.1 and Section 2.2.2.

If a Pockels effect, see Section 2.1.4, is used for shifting the phase in the MZM arms with a static or slowly varying external electric field E_{ext}, we can write the phase change $\delta\varphi$ caused by E_{ext} as

$$\delta\varphi = -\frac{1}{2} n_0^3 r_{33} E_{\mathrm{ext}} k_0 \ell, \tag{2.15}$$

where r_{33} is the electro-optic coefficient, n_0 is the optical refractive index in the active section of length ℓ, and k_0 the vacuum wave vector of the optical carrier. If the modulating electric field is written as $E_{\mathrm{ext}} = u_{\mathrm{s}}/d$, with d being the distance between electrodes used to apply the control voltage u_{s} we can express $\delta\varphi$ as

$$\delta\varphi = -\frac{1}{2} n_0^3 r_{33} \frac{u_{\mathrm{s}}}{d} k_0 \ell. \tag{2.16}$$

This leads to the time dependent phase-shift $\delta\varphi(t)$, controlled by the voltage u_{s},

$$\delta\varphi(t) \propto u_{\mathrm{s}}(t). \tag{2.17}$$

2.2.1 Push-pull operation

Simultaneous phase and amplitude modulation is generally undesired for intensity or amplitude modulation systems. In intensity modulation systems, phase modulation results in a chirp which leads to increased signal distortions for signals propagating through dispersive media. A detailed discussion on chirp caused by MZMs can be found in Section 4.2. In amplitude modulation system it is often desired that the amplitude is precisely controlled without affecting the phase, see, e.g., the IQ modulator in Section 2.2.2. Unwanted phase modulation can be suppressed by so-called push-pull operation where the phase in each of the MZM arms, Eq. 2.9 and 2.10, is chosen such that $\varphi_1 = -\varphi_2$. The transfer functions in Eq. 2.13 and Eq. 2.14 then simplify to a purely real amplitude transfer function and we can write

$$E_{\mathrm{out},1} = E_{\mathrm{in}} \cos\left(\frac{\Delta\varphi}{2}\right) = E_{\mathrm{in}} \cos\left(\varphi_1\right) \tag{2.18}$$

and

$$E_{\mathrm{out},2} = E_{\mathrm{in}} \sin\left(\frac{\Delta\varphi}{2}\right) = E_{\mathrm{in}} \sin\left(\varphi_1\right). \tag{2.19}$$

The intensity transfer functions for push-pull operation are given by

$$|E_{\mathrm{out},1}|^2 = |E_{\mathrm{in}}|^2 \cos^2\left(\frac{\Delta\varphi}{2}\right) = |E_{\mathrm{in}}|^2 \frac{1}{2}\left(1 + \cos(\Delta\varphi)\right) \tag{2.20}$$

and

$$|E_{\mathrm{out},2}|^2 = |E_{\mathrm{in}}|^2 \sin^2\left(\frac{\Delta\varphi}{2}\right) = |E_{\mathrm{in}}|^2 \frac{1}{2}\left(1 - \cos(\Delta\varphi)\right). \tag{2.21}$$

The amplitude transfer function as given by Eq. 2.18 and the intensity transfer function as given by Eq. 2.20 are shown in Fig. 2.2. For intensity modulation the transfer function can be linearized if a small-signal modulation is applied around the so-called quadrature point at $\Delta\varphi = \frac{\pi}{2}$ such that $\Delta\varphi = \frac{\pi}{2} + \delta\varphi$ with $|\delta\varphi| \ll \pi/2$. The so-called null point is chosen for optimum field linearity and is given at $\Delta\varphi = \pi$. Small-signal amplitude modulation is then realized for $\Delta\varphi = \pi + \delta\varphi$ with $|\delta\varphi| \ll \pi$. The null point is typically chosen as operating point when realizing complex modulation formats in IQ-modulators, see Section 2.2.2. Linearizing Eq. 2.18 and 2.20 by setting the operating point accordingly we can use Eq. 2.17 to write

$$E_{\mathrm{out}} \propto u_{\mathrm{s}} \tag{2.22}$$

for the amplitude modulation in the null point and

$$|E_{\mathrm{out}}|^2 \propto u_{\mathrm{s}} \tag{2.23}$$

for intensity modulation in the quadrature point. These two expression clearly show how an MZM can be used as EO amplitude or intensity modulator.

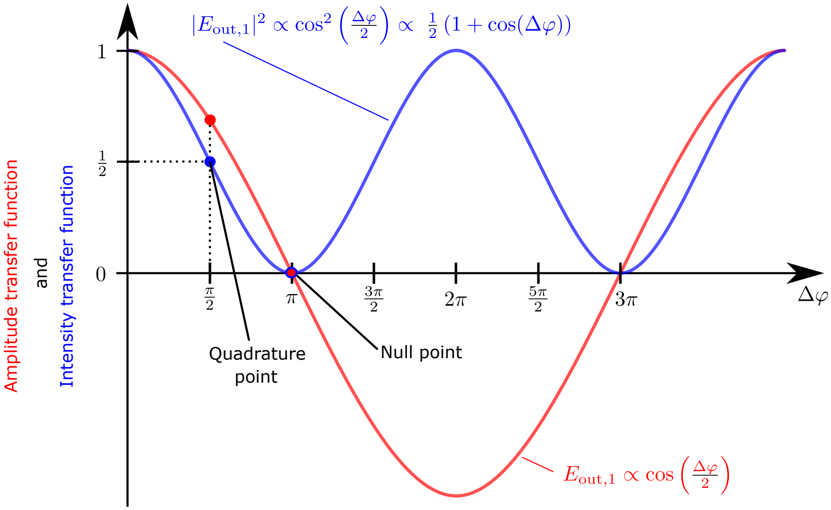

Fig. 2.2: Amplitude transfer function (red) and intensity transfer function (blue) of an MZM in push-pull configuration. For intensity modulation the transfer function is linearized if a small signal modulation is applied around the so-called quadrature-point at $\Delta\varphi = \frac{\pi}{2}$. The so-called null point, $\Delta\varphi = \pi$, is the operating point where amplitude and intensity become zero (optimum field linearity).

2.2.2 IQ modulator

To realize complex modulation formats with independent modulation of both amplitude and phase of the optical carrier (see Section 2.6 for an introduction into various modulation formats) a single MZM could be used as explained in the context of Eq. 2.13. However, to set the amplitude and phase of the output signal, a sophisticated control of the phases φ_1 and φ_2 in the two arms of the MZM is needed. In practical applications it is desired to set the in-phase component (I-component) and the quadrature component (Q-component) of the output signal directly by independent control signals. This can be achieved by nesting two “child” MZMs operated in push-pull configuration and biased at the null point, see Section 2.2.1, to form a “parent” MZM. To form an in-phase/quadrature-phase (IQ) modulator, an additional static phase shift of

90° between the combined signals is introduced into one arm of the “parent” MZMs, see Fig. 2.3(a). The output signal of the IQ-modulator is given by

$$E_{\mathrm{out}} = \frac{E_{\mathrm{in}}}{2}\left[\cos(\Delta\varphi_{\mathrm{MZM1}}) + \mathrm{j}\cos(\Delta\varphi_{\mathrm{MZM2}})\right], \tag{2.24}$$

with $\Delta\varphi_{\mathrm{MZM1}}$ and $\Delta\varphi_{\mathrm{MZM2}}$ being the relative phase difference in the two child MZMs as given by Eq. 2.13. The I-component

$$I = \frac{E_0}{2}\cos(\Delta\varphi_{\mathrm{MZM1}}) \tag{2.25}$$

and the Q-component

$$Q = \frac{E_0}{2}\cos(\Delta\varphi_{\mathrm{MZM2}}) \tag{2.26}$$

can now be adjusted independently by controlling $\Delta\varphi_{\mathrm{MZM1}}$ and $\Delta\varphi_{\mathrm{MZM2}}$, respectively. The output field E_{out} can reach any point in the complex plane, see Fig 2.3(b), and we can derive the following useful relations:

$$E_{\mathrm{out}} = (I + \mathrm{j}Q)\mathrm{e}^{\mathrm{j}\omega t} \tag{2.27}$$

and

$$I + \mathrm{j}Q \equiv a_{\mathrm{IQ}}\mathrm{e}^{\mathrm{j}\varphi_{\mathrm{IQ}}} \tag{2.28}$$

with $a_{\mathrm{IQ}} = \sqrt{I^2 + Q^2}$ and $\varphi_{\mathrm{IQ}} = \arg(I + \mathrm{j}Q)$. For the real part of the complex representation of the E-field at the output we can write

$$\Re\left\{E_{\mathrm{out}}\right\} = I\cos(\omega t) - Q\sin(\omega t). \tag{2.29}$$

2.2.3 Basic performance metrics for MZMs

This section introduces important performance metrics for MZMs. These metrics will be used to evaluate the overall performance of modulators and help to identify design trade-offs when developing new devices.

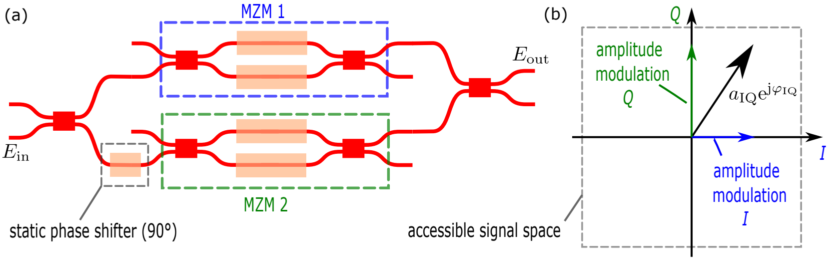

Fig. 2.3: In-phase-quadrature-phase IQ modulator: (a) IQ modulator realized with two nested "child" MZMs in the arms of a "parent" MZM. A static phase shifter is added in one arm to ensure that the two signals from MZM 1 and MZM 2 have a 90° phase difference upon recombination. Both "child" MZMs are operated in push-pull configuration and biased at the null point. (b) By adjusting the phase difference in the two child MZMs the I- and Q-component of the output signal can be set and any point in the complex plane can be reached.

π-voltage U_π

The π-voltage U_π of an MZM in push-pull configuration is the voltage that is required to cause a relative phase shift of $\Delta\varphi = \pi$, see Eq. 2.18. It corresponds to the voltage that is needed to bring the intensity transfer function, Eq. 2.20, depicted in Fig. 2.2, from the point of maximum transmission to the point of minimum transmission. Using U_π, Eq. 2.16 can be written as

$$\Delta\varphi = \frac{u_{\mathrm{S}}\pi}{U_\pi}, \tag{2.30}$$

where $U_\pi = \pi d/(n_0^3 r_{33} k_0 \ell)$, see Eq. 2.16. The π-voltage is a device property. Making the interaction length ℓ of a modulator longer reduces U_π. The **voltage-length-product** $U_\pi\ell$ is therefore often used as a length-independent metric for the efficiency of a particular modulator scheme.

Insertion loss $a^{(\mathrm{IL})}$

The optical power loss in the modulator even when set to maximum transmission is given by the insertion loss (IL) $a^{(\mathrm{IL})} = 10\log(P_{\mathrm{in}}/P_{\mathrm{out}})$ with $[a^{(\mathrm{IL})}] =$ dB. The IL comprises losses in imperfect waveguides due to absorption and scattering, losses due to imperfect power splitters and combiners and propagation losses in the active sections of the phase shifters. If the phase shifters are lossy, reducing the modulator length leads to lower propagation losses, however, U_π is increased. A frequently used metric for modulator concepts and technologies is the product of the voltage-length-figure of merit (FOM) $U_\pi \ell$ and the optical power propagation loss of the phase shifter $a_{\mathrm{PS}} = 4.34\alpha^{(\mathrm{pwr})}$ expressed in dB/m [49]. This results in the so-called **π-voltage-loss-product** $a_{\mathrm{PS}} U_\pi \ell$ with the unit dB · V and can be interpreted as the π-voltage of a device having 1 dB insertion loss, or as the propagation loss of a device with $U_\pi = 1$ V. For simplicity the index "PS" in a_{PS} is omitted in the remainder of this work. In the context of the $aU_\pi \ell$-FOM, a always refers to the optical power propagation loss in the active section of the phase shifter.

Extinction Ratio

The extinction ratio (ER) of an MZM is defined as the ratio between the transmitted power in the maximum transmission point and the transmitted power in the minimum transmission point, often expressed in dB. If the phase shifters are loss-less and the splitters split the incoming power in perfectly equal parts, as assumed in the derivation of Eq. 2.13, the ER is infinitely large. Due to loss or imperfect power splitters the field strength of the signals from the two arms may differ. This results in imperfect extinction and the ER has a finite value. Generally a large ER is desired.

Electro-Optic Bandwidth

If a time-dependent control signal is used to drive the MZM such that there is a time dependent phase shift $\Delta\varphi(t)$, the response time of the modulator is of interest. The bandwidth of a modulator is not defined consistently in literature [64, 65]. Typically, the small-signal EO response is quantified either by the electro-optic-electric (EOE) 3 dB bandwidth or the EOE 6 dB bandwidth, the latter one sometimes referred to as electro-optic (EO) 3 dB bandwidth. For intensity modulation, the EOE 3 dB bandwidth is defined by the frequency $\omega_{3\mathrm{dB}}/2\pi$ where the amplitude of the optical power modulation is reduced by a factor of $1/\sqrt{2}$ compared to the low-frequency limit. A detailed discussion on how to define and measure the bandwidth of a modulator is given in Section 2.5.5 along with a discussion of bandwidth-limiting effects.

Chirp

Unwanted phase modulation in intensity modulated signals is called chirp. Chirp can lead to signal distortions in dispersive media. The so-called chirp parameter $\alpha^{(c)}$ is defined as the ratio of the phase modulation strength and the amplitude modulation strength, see Section 4.2 for a detailed discussion. Ideally, MZMs in push-pull configuration exploiting a pure Pockels effect allow to completely suppress any phase modulation and therefore allow chirp-free operation, see Eq. 2.18, and $\alpha^{(c)} = 0$. In real-world devices with finite ER or with an imbalance in the phase modulation of the two arms, a residual phase modulation leads to chip and non-zero values of the chirp parameter.

Footprint

The size of integrated EO MZMs is an important FOM because a reduction in size leads to a reduction of manufacturing costs and allows integrating more functionality on the same available chip area. Since the π-voltage U_π of an MZM is directly linked to the length ℓ of the active section of the phase shifters, more efficient modulator technologies lead to a reduced size of the devices. A short length of the modulator can also be beneficial for the achievable modulation speed, see Section 2.5.5.

Energy dissipation

While the $U_\pi \ell$-FOM is an essential performance metric to quantify the efficiency of the MZM (the smaller the better), the energy dissipated when driving the device with a dynamic control voltage u_s is crucial when designing optical communication systems [16]. In this case the energy dissipation does not only depend on the EO modulator itself, but also on the surrounding electronic circuit used to feed the modulating signal to the modulator [49]. The relevant FOM is the energy W_bit dissipated per bit that is encoded onto the optical carrier. For example, if we assume a binary data signal with equal probabilities for

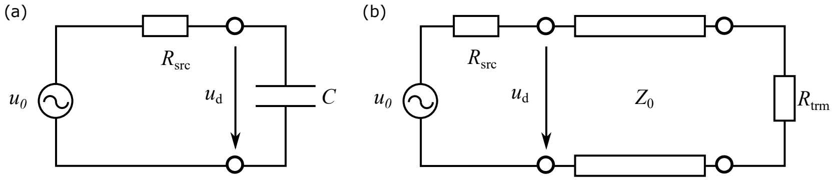

Fig. 2.4: Equivalent-circuit models of EO modulators to derive electrical energy dissipation. (a) Lumped-element EO modulator represented by a capacitance. The modulator is driven by a voltage source with internal resistance R_{src}. (b) Impedance-matched traveling-wave modulator modeled by a transmission line having a characteristic impedance matched to the source impedance R_{src} and the terminating impedance R_{trm}.

the "on-state" ($u_{\mathrm{s}} = u_{\mathrm{d}}$ is applied to the modulator) and "off-state" ($u_{\mathrm{s}} = 0$ is applied to the modulator), and model the modulator as a lumped element with capacitance C, see Fig. 2.4(a), the energy dissipated per bit is given by [49,66]

$$W_{\mathrm{bit}} = \frac{C u_{\mathrm{d}}^2}{4}. \tag{2.31}$$

However, oftentimes MZMs are designed as traveling-wave devices, see Section 2.5, and the modulator can not be considered as being a lumped element. In this case the modulator can be modeled as a transmission line. For a modulator with a characteristic impedance Z_0 matched to the source resistance R_{src} and terminated in a matched load R_{trm} as shown in Fig. 2.4(b), the energy dissipated for a binary signal with equal probabilities for "ones" and "zeroes" is given by [49]

$$W_{\mathrm{bit}} = \frac{u_{\mathrm{d}}^2 T_{\mathrm{bit}}}{4 R_{\mathrm{trm}}}, \tag{2.32}$$

with T_{bit} being the duration of the time slot of one bit (symbol duration). A more detailed discussion of the energy dissipation in SOH modulators is found in Section 4.8.

Compatibility with CMOS processes

Besides performance, process compatibility of the materials and the manufacturing steps is an important characteristic for integrated EO modulators [16]. In particular for Si modulators the compatibility with established CMOS processes is important for cost efficient and scalable deployment [67]. So-called "zero-change" processes, where photonic structures are fabricated with unmodified digital electronics processes were demonstrated in recent years [68, 69]. Most SiP modulators, however, can not be directly fabricated using the very same processes as for CMOS electronics. Generally, it is desired for a technology to require the smallest possible modifications in the highly sophisticated front-end-of-line (FEOL) fabrication processes, i.e. by only adding a back-end-of-line (BEOL) process.

2.3 Silicon-photonic Mach-Zehnder modulators: State of the art

There is a wide variety of high-speed, silicon MZMs. A comprehensive review of state-of-the-art, high-speed silicon phase shifters is given in [16]. The goal of this section is to shortly review and categorize all relevant Si MZM device types, to give a comparative overview of their performance parameters, and to provide references for putting the work presented in this thesis into perspective.

Si MZMs can be categorized into all-silicon modulators and into modulators combining Si with addition materials, either through monolithic or through heterogeneous integration. All-silicon MZMs are most commonly realized either as reverse-biased p-doped-intrinsic-n-doped (PIN) or PN diodes or as silicon-insulator-silicon capacitors (SISCAPs). If integration with additional materials other than pure or doped Si is employed, the same modulator structures, namely PIN, PN and SISCAP modulators, can be used, potentially with improvements in performance compared to all-Si implementations. Further, the availability of materials with second-order optical nonlinearity opens the possibility to realize true Pockels-effect modulators. Figure 2.5 gives an overview of all of these types of Si MZMs along with a schematic cross section of the phase shifter, Table 2.1 gives an overview of the key performance metrics for selected modulators. A brief description of the basic modulator types is given in the following paragraphs.

- **PIN and PN modulators**
  In PIN phase shifters the waveguide consists of a PIN diode, most commonly operated in reverse bias to deplete the waveguide from free

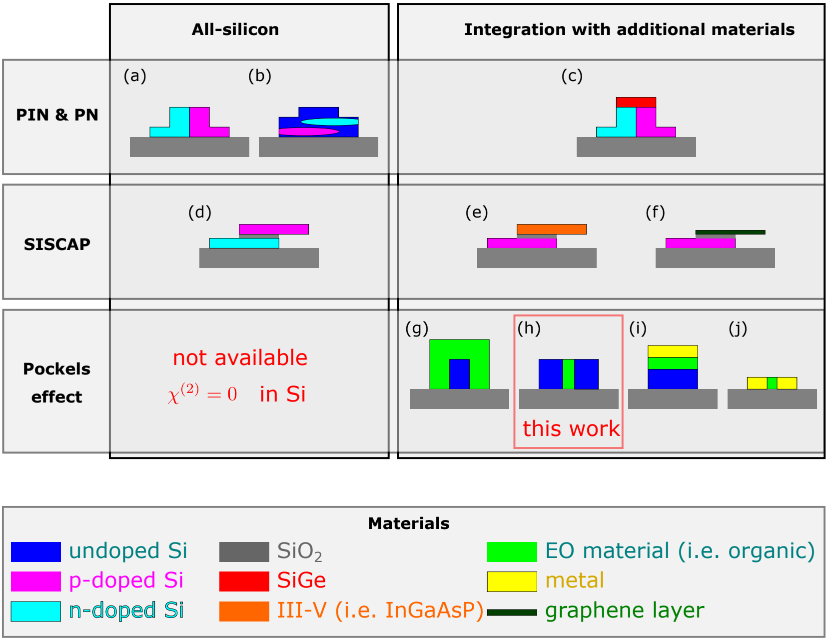

Fig. 2.5: Overview of state-of-the-art high-speed Si MZMs. The image depicts schematic cross-sections of the phase shifters categorized into all-Si phase shifters and phase shifters where Si is combined with additional materials either through monolithic or through heterogeneous integration. (a) Conventional PN-junction, (b) vertical PIN-junction, (c) PN-junction using a SiGe overlayer, (d) silicon-insulator-silicon capacitor (SISCAP), (e) SISCAP with the n-doped side replaced by a III-V semiconductor, and (f) SISCAP with the n-doped side replaced by a single graphene layer. Since Si does not exhibit a second-order optical nonlinearity, Pockels-effect modulators have to be realized as hybrid system using e.g. an organic material or a ferroelectric Perovskite as EO material. These modulators can be realized as a (g) rib waveguide clad with the EO material or as a (h) slot waveguide filled with the EO material. Waveguides guiding a hybrid plasmonic mode (i) or a plasmonic mode in a plasmonic slot waveguide (j) are also used as hybrid EO modulators when functionalized with EO materials. Examples and references along with performance metrics are given in Table 2.1.

carriers. If the intrinsic region between the n-doped and the p-doped part is negligible, see Fig 2.5(a), these modulators are also referred to as PN modulators. We will refer to the general modulator scheme as P(I)N as the operation principle of PIN and PN modulators is identical if operated under reverse bias condition[1]. A modulation of the applied voltage leads to a modulation of the width of the depletion region. The resulting modulation of the free-carrier concentration inside the waveguide results in a modulation of the waveguide's effective refractive index, see Section 2.1.2. For an efficient P(I)N modulator a large device capacitance is desired because a large number of carriers is moved into and out of the waveguide. A large device capacitance, however, increases the dynamic power consumption of the modulator and increases the RC time-constant, associated with the device capacitance and resistive connections to it, see Fig. 2.4. In addition, to increase the capacitance, the width of the space charge region has to be reduced which requires higher doping concentration and therefore induces higher optical losses due to free-carrier absorption. The efficiency of high-speed P(I)N modulators is therefore intrinsically limited. Best-in-class high-speed modulator efficiencies are limited to $U_\pi \ell = 25\,\mathrm{Vmm}$ but reach EO bandwidths of more than 50 GHz [70]. Optimizing the doping profile to place the free carriers where they contribute most to the modulation and reducing their concentration elsewhere is therefore an effective measure to improve the overall performance. Figure 2.5(b) shows an example of a horizontal PIN junction (in contrast to the vertical PN junction in Fig. 2.5(a)) which is used to increase the volume in which the free-carrier concentration is modulated. This approach leads to significantly improved efficiencies with $U_\pi \ell = 7.4\,\mathrm{Vmm}$ [71]. Other, more complex doping profiles, potentially supported by epitaxial overgrowth steps provide a way to tailor the EO properties of P(I)N modulators [16].

The efficiency of P(I)N modulators can be improved using integration with additional materials. In [72] SiGe has been used to replace the p-doped silicon, see Fig. 2.5(c). The strain induced by the lattice mismatch between Si and Ge reduces the effective mass of the holes, thus

---

[1] PIN modulators can also be operated under forward bias condition which leads to high efficiencies. This mode of operation is not suited for high-speed operation due to the long carrier lifetime in the intrinsic region and is therefore not considered here.

increasing the refractive index change, see Eq. 2.1. This leads to an improved efficiency of $U_\pi \ell = 6\,\mathrm{Vmm}$ and offers the advantage that Ge is well established in CMOS processes. While this approach relaxes the fundamental trade-off between efficiency and speed in P(I)N modulators, even these highly-optimized device exhibit $U_\pi \ell$-products of several Vmm.

- **SISCAP modulators**
  In SISCAP MZMs, the active section of the waveguide comprises a SIS capacitor, Fig. 2.5(d). These modulators are most commonly operated in accumulation mode, where carriers are accumulated on either side of the insulator. As with the P(I)N modulators the modification of the free-carrier density results in a change of the waveguide's effective refractive index. The accumulation of carriers of opposite polarity on both sides of the insulator allows increasing the device capacitance compared to P(I)N modulators without the need for doping. This leads to very efficient modulators, i.e. $U_\pi \ell = 1.6\,\mathrm{Vmm}$ [73] without an undue increase of optical losses. However, the high device capacitance limits the operation speed due to an increased RC time-constant [16]. As with P(I)N modulators, the efficiency of SISCAP modulators can be improved by adding additional materials. In InGaAsP the electrons contribute stronger to a refractive index change than in Si [43]. This effect is used in [74, 75], where on the n-doped side of the SISCAP, Si was replaced with n-doped InGaAsP by using direct wafer bonding. The efficiency is thus improved to $U_\pi \ell = 0.47\,\mathrm{Vmm}$ [75]. Alternatively, graphene has been used to replace Si on one side of the insulator, exploiting the unique properties of a two-dimensional semiconductor [16, 76]. So far, these heterogeneously integrated SISCAP modulators are severely limited in at least one of the key performance metrics, see Table 2.1, and are not considered for practical applications.

- **Pockels-effect modulators**
  Si MZMs based on carrier-induced refractive index change suffer from the aforementioned fundamental trade-off between modulation efficiency, speed and optical losses. It is furthermore impossible to decouple amplitude and phase modulation which impairs MZM performance, see Section 2.2.2. To overcome these limitations, a field driven EO effect is desired. Since silicon exhibits no linear EO effect, due to its

centro-symmetric crystal structure, additional materials have to be integrated into the SiP platform [16, 17]. Substantial efforts have been made to successfully integrate organic EO materials or ferroelectric perovskites such as $LiNbO_3$ [36], $BaTiO_3$ [77] or PZT [78]. All of those materials exhibit a Pockels effect and therefore offer pure phase modulation which can be transformed into a pure amplitude modulation in an MZM. Since the intrinsic EO efficiency of the materials is higher than for the plasma-dispersion effect available in pure Si, the approach of heterogeneous integration allows substantially improving the modulator efficiency without being constrained by the efficiency-loss trade-off as present with all-Si P(I)N or SISCAP modulators. Various waveguide designs to combine the high index material Si with organic or ferroelectric EO materials are found in literature. Two basic realizations are shown in Fig. 2.5(g) and Fig. 2.5(h), where the EO material is used as cladding material of a Si waveguide or filled into the slot of a Si slot waveguide, respectively. A central optimization strategy when designing such hybrid Si modulators is to increase the overlap between the optical mode and the modulating electric field. The slot waveguide offers very good confinement of the optical mode to the slot region and sophisticated electrode design can then lead to an almost perfect overlap of the optical and electric modes [49]. The approach of a slot waveguide filled with an EO material is called SOH integration and is the modulator technology investigated and optimized in this work. The strong intrinsic EO activity of the underlying organic material and the good overlap due to the slot-waveguide geometry can lead to ultra high in-device modulation efficiencies and corresponding ultra-small π-voltage-length products $U_\pi \ell = 0.32\,\mathrm{Vmm}$ [18]. The SOH approach is particularly attractive since the organic material can be spun-on or dispensed in a back-end-of-line (BEOL) process without a need to alter conventional SiP fabrication processes. The integration of ferroelectric materials, however, requires a dedicated, heavily modified fabrication process. A detailed introduction into SOH modulators is given in the Section 2.4.

Hybrid integration of Si waveguides with organic or ferroelectric EO materials can be combined with plasmonic structures. Hybrid plasmonic waveguides, see Fig. 2.5(i), or plasmonic slot waveguides, Fig. 2.5(j), are used to guide a surface plasmon polariton along a metal surface which in turn can lead to strong interaction between optical and modulating electric field [49]. In particular, the combination of plasmonic slot waveguides with organic EO materials in plasmonic-organic hybrid (POH) devices has led to very efficient MZMs with $U_\pi \ell = 0.05\,\mathrm{Vmm}$ [55] and extraordinary EO bandwidths of hundreds of GHz [79, 80]. However, high optical losses in the metal limit the practical interaction length and therefore constrain the achievable U_π and lead to high π-voltage-loss products of $aU_\pi \ell > 10\,\mathrm{VdB}$, see Table 2.1.

A comparative overview of important MZM FOMs of selected modulators published in literature is given in Table 2.1. With the exception of SOH modulators, neither of the technologies offers excellent efficiency along with bandwidths of the order of 100 GHz and good compatibility with standard SiP processes. The organic EO material can be added in a BEOL-process. Therefore, SOH modulators can be combined with the full portfolio of SiP components. Combined with the high efficiency, large bandwidth and small π-voltage-loss products, SOH modulators are one of the most promising candidates for high-performance, low-cost SiP modulators. Significant improvements in the thermal stability of the organic materials could be made recently [20]. Further progress in terms of reliability is to be expected similar to what was achieved with other organic technologies such as organic light-emitting diodes (OLEDs).

Table 2.1: Performance comparison of state-of-the-art high-speed Si MZMs. The schematic cross-section of all device types is given in Fig. 2.5.

Technology	Ref.	EO Bandwidth	$U_\pi \ell$	$aU_\pi \ell$	Process modification
all-Si P(I)N (conventional)	[70]	50 GHz(1)	25 Vmm	NA	none
all-Si P(I)N (vertical junction)	[71]	48 GHz	7.4 Vmm	31 VdB	none
monolithic P(I)N (SiGe)	[72]	> 10 GHz(1)	6 Vmm	12 VdB	none
all-Si SISCAP	[73]	< 20 GHz(2)	1.6 Vmm	5.7 VdB	none
heterogeneous SISCAP (III-V)	[74]	2.2 GHz(1,3)	0.9 Vmm	4 VdB	new process
heterogeneous SISCAP (III-V)	[75]	100 MHz(1,3)	0.47 Vmm	0.9 VdB	new process
heterogeneous SISCAP (graphene)	[76]	5 GHz(1,3)	2.8 Vmm	62 VdB	new process
POH	[80]	> 500 GHz	0.06 Vmm	30 VdB	new process
POH	[55]	NA	0.05 Vmm	22 VdB	new process
BTO on Si	[38]	30 GHz(1,4)	4.5 Vmm	4.6 VdB	new process
$LiNbO_3$ on Si	[36]	100 GHz(1)	22 Vmm	0.44 VdB	new process
SOH	[81]	> 100 GHz	11 Vmm	55 VdB	BEOL post-processing
SOH	[18]	< 20 GHz(5)	0.32 Vmm	1.2 VdB	BEOL post-processing

(1) A clear definition of the EO S_{21}-parameter was not found. The context suggests that the reported bandwidth is the EOE 3 dB bandwidth as defined in Section 2.5.5.

(2) Bandwidth not reported in the paper. A reduction of the vertical eye-opening of a 25 Gbit/s eye diagram can be observed.

(3) Bandwidth currently limited by the contact resistance (not a fundamental limit).

(4) A ring resonator (no MZM) was characterized in this work.

(5) The reported bandwidth in this work was the EOE 6 dB bandwidth as defined in Section 2.5.5.

2.4 SOH modulator device principles

The absence of a Pockels effect in Si is compensated by using organic EO materials, see Section 2.1.4, to overclad Si waveguides in SOH modulators fabricated in silicon-on-insulator (SOI) technology [48,49,51]. The EO activity is then provided by the highly efficient organic EO materials with EO coefficients of up to $r_{33} = 550\,\mathrm{pm/V}$ [47]. Besides a high intrinsic EO efficiency, a good overlap between the modulating electric field and the optical mode is of paramount importance for an efficient modulation. This can be accomplished by using a Si slot waveguide as shown in Fig. 2.6(a), where typical dimensions and refractive indices for the materials used refer to an operation at a vacuum wavelength of $\lambda_0 = 1.55\,\mu\mathrm{m}$. The rails of the slot waveguides are attached to thin, doped Si slabs, which allow to apply a modulation voltage. The Si slot waveguide is filled with an organic EO material with a refractive index much lower than the refractive index of Si. Due to the discontinuity of the normal component of the optical electric field with a higher field amplitude in the low-refractive-index region and due to the proximity of the two silicon rails, the optical mode is confined inside the slot region, and most of the light propagates inside the EO active material [82]. The dominant x-component of the optical electric field is shown in a color-coded plot in Fig. 2.6(b). The modulating RF voltage U_{mod} drops almost entirely across the insulating slot, and therefore the associated electric RF field is confined to the slot region as well. Fig 2.6(c) shows a color plot of the dominant x-component of the modulating electric field. The narrow slot leads to high modulating field strengths and to an excellent overlap of the electric mode with the optical mode. This results in ultra-high efficiencies with voltage-length products of only 0.32 Vmm [83]. The concept of such a slot waveguide attached to Si slabs and clad with EO organic material was first demonstrated to work as an EO modulator at RF frequencies by Ding et al. [50]. While other waveguide geometries, e.g., narrow Si waveguides with the evanescent field penetrating into an EO cladding, might be beneficial for certain applications, the slot waveguide is best in terms of modulation efficiency and is used throughout the work reported in this thesis.

The basic concept [49] of an SOH MZM using over-clad slot waveguides in each arm is shown in Fig. 2.7. The top view, depicted in Fig. 2.7(a), resembles the schematic of an integrated MZM introduced in Section 2.2, Fig. 2.1(b).

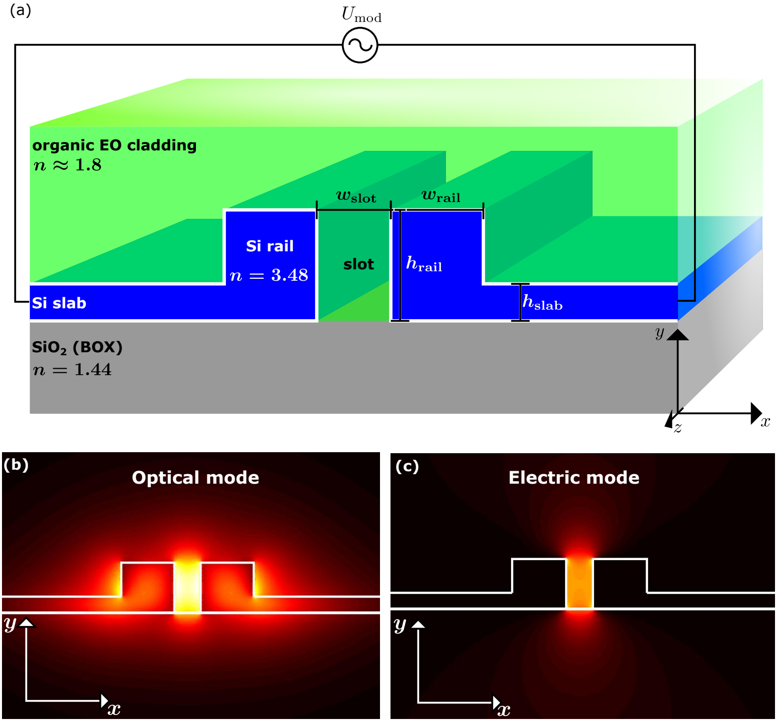

Fig. 2.6: Silicon slot waveguide with organic EO cladding. (a) Slot waveguide with the refractive indices of the used materials. Thin, doped Si slabs are attached to the rails of the slot waveguide to apply a modulation voltage U_{mod}. Typical dimensions are $w_{\mathrm{slot}} = 60\ldots160\,\mathrm{nm}$, $w_{\mathrm{rail}} = 200\ldots250\,\mathrm{nm}$, $h_{\mathrm{rail}} = 220\,\mathrm{nm}$, and $h_{\mathrm{slab}} = 70\ldots90\,\mathrm{nm}$. (b) Color-coded plot of the dominant x-component of the optical mode. The highest intensity is found in the slot. (c) Color-coded plot of the dominant x-component of the modulating electric field.

Light from the optical input is split by an MMI splitter into the two arms of the MZM. Figure 2.7(b) depicts an artist's view of the MZM. The cross-section of the device with the slot waveguides in each arm of the MZM is shown in Fig. 2.7(c). Strip-to-slot mode converters [84] connect the Si strip waveguides with the slot waveguides of the phase shifters. This transition can be seen in Fig. 2.7(d) that depicts a magnified artist's view of the beginning of the slot waveguide section with the strip-to-slot converters. Note that, for a better understanding, in the graphical representation in Fig. 2.7(d), only one of the phase shifter slots is filled with the organic EO material.

The modulating electric drive signal is applied via metal electrodes which are directly deposited onto the Si slabs, see Fig. 2.7(c). In some cases, an additional oxide over-cladding can be used to protect the strip waveguides on the chip. This oxide cladding is then locally removed to expose the slot waveguide for application of the organic EO material. If an oxide over-cladding is used, the electrodes are deposited on top of this oxide layer and connect to the Si slabs by metal vias. For a cross-section of a modulator with oxide cladding and vias see Section 4.2, Fig. 4.1. In either way, the electrodes are arranged as a coplanar GSG transmission line, see Fig. 2.7(a-c). The modulating RF signal co-propagates with the optical carrier along the modulator. Typical lengths ℓ for SOH modulators range from 250 µm to 1.5 mm. To increase the conductivity of the Si slabs, the free-carrier density can be increased by doping through ion-implantation and/or by the formation of an electron accumulation layer at the Si-burried-oxide-layer (BOX) interface, induced by a so-called "gate"-voltage [85] between the slabs and the handle wafer. Increasing the slab conductivity helps to reduce the RC time-constant associated with the slot capacitance and the slab resistance. This RC time-constant limits the modulation speed of the SOH MZM. A general discussion of bandwidth-limiting effects of transmission-line-driven MZMs is given in Subsection 2.5.5. A detailed discussion of the bandwidth of SOH modulators along with experimental investigations and with implications for the design of SOH modulators is presented in Chapter 3.

To activate the macroscopic EO activity of the organic material, the molecular dipoles in the material have to be oriented in an acentric order by a one-time poling process, see Section 2.1.4. The poling procedure for an SOH MZM for single-drive push-pull operation is illustrated in Fig. 2.8. Before the poling process, Fig. 2.8(a), the molecular dipoles are in their thermodynamically favored state and are randomly oriented, leading to a vanishing macroscopic EO

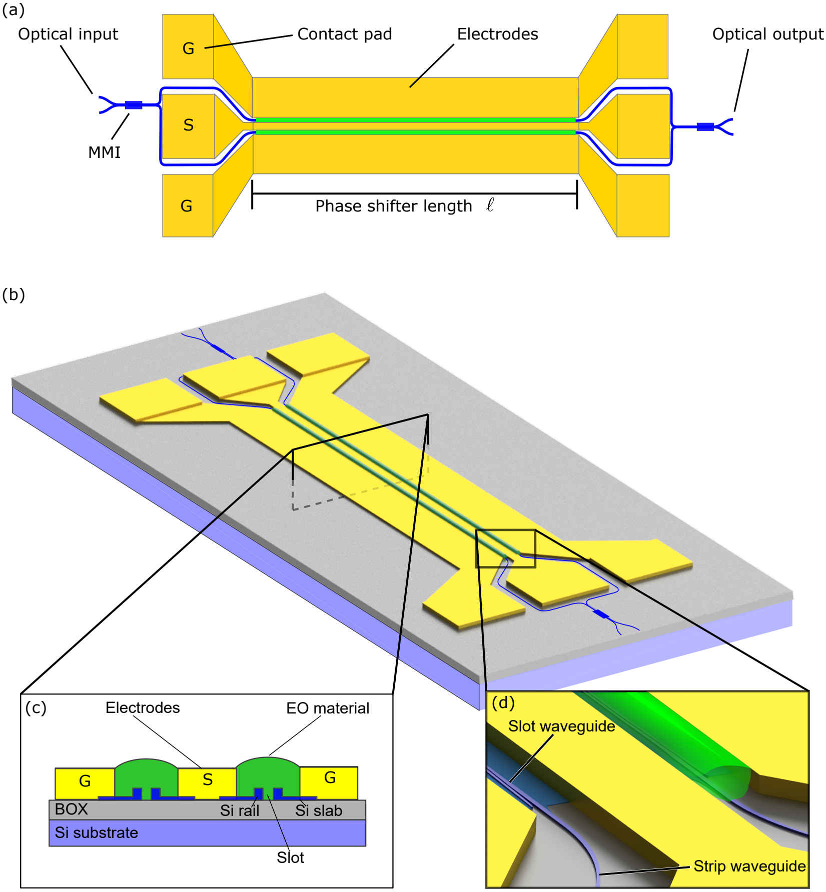

Fig. 2.7: SOH modulator concept: (a) Top-view of the modulator with optical waveguides shown in blue, the active section of the phase shifters with the organic EO material shown in green, and the metal electrodes shown in yellow. The electrodes form a coplanar ground-signal-ground (GSG) transmission line. The light is split and combined by multi-mode-interference (MMI) couplers. (b) Artist's view of the SOH MZM. (c) Cross-section of the SOH MZM. Thin, doped Si slabs connect the slot waveguide to the metal electrodes. (d) Magnified artist's view of the transition from the slot waveguide to the strip waveguide section (strip-to-slot converter [84]). For better understanding the EO cladding (green) is shown in one arm only. Parts of this figure were adapted with permission from [J2] Fig. 1 ©The Optical Society.

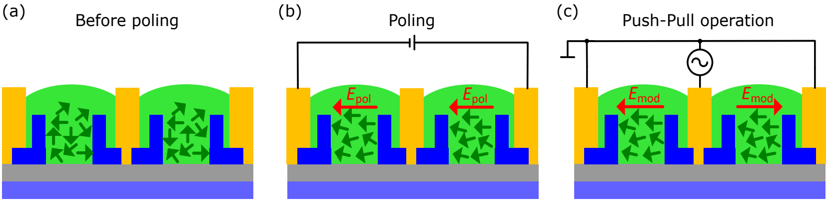

Fig. 2.8: Poling process and push-pull operation of SOH MZM. “(a) Prior to poling, the molecular dipoles (green arrows) in the organic EO material are randomly oriented such that no macroscopic Pockels effect can be observed. (b) At elevated temperatures, a poling voltage [applied between the floating ground electrodes] induces a poling field E_{pol} which aligns the molecular dipoles predominantly along the electric field. This molecular orientation is frozen when the material is cooled down to room temperature. (c) In push-pull operation, the modulating RF voltage is applied to the center signal electrode thereby leading to a modulating field vector E_{mod} that is oriented parallel to the poling direction in one arm and anti-parallel in the other one. This allows a pure amplitude or intensity modulation without residual phase modulation (chirp-free) [86].” Adapted with permission from Fig. 1 in [J3] ©The Optical Society.

activity. For poling, Fig. 2.8(b), the modulator is first heated to a temperature close to the glass-transition temperature of the organic material such that the molecular dipoles become mobile. A poling voltage is then applied to the floating ground electrodes, and the dipoles in the slot align according to the poling field E_{pol}. While the poling field remains applied, the modulator is cooled well below the glass transition temperature of the organic material, and the orientation of the molecular dipoles is thus frozen. The poling field can then be removed and the organic material exhibits a macroscopic EO activity. For operation of the MZM, Fig. 2.8(d), the modulation voltage is applied to the central signal electrode such that the modulating field vector is oriented parallel to the molecular dipoles in one arm of the MZM and antiparallel in the other arm. This leads to phase shifts of equal magnitude but opposite sign and hence to an intrinsic push-pull operation, see Section 2.2.1.

2.5 Transmission-line-driven electro-optic modulators

If the length ℓ of a modulator does not allow to treat the modulator electrically as a lumped element, voltages and currents in the modulator may vary along the devices. The metal electrodes used to apply the electrical signal are therefore often realized as a transmission line that allows the signal to propagate along the modulator. This section briefly summarizes the key concepts of microwave engineering that are needed to formulate a quantitative model of the EO behavior of such modulators.

2.5.1 Electrical transmission lines

If the physical dimension of an electrical circuit is much smaller than the wavelength of the considered electrical signal, the components in the network can be treated as lumped elements connected by perfect wires. However, if at high frequencies the dimension of the network becomes lager than a considerable fraction of the wavelength, the assumption of lumped elements does not hold any more. Currents and voltages may vary along the network, and in general Maxwell's equations have to be applied rigorously to describe the network and to calculate voltages and currents. For special cases, microwave theory has developed simplified models that allow to use circuit theory to treat such networks at high frequencies. One such case is the propagation of voltages and currents along a conductor forming a transmission line, which can be modeled by the distributed equivalent circuit shown in Fig. 2.9. The full line is described by infinitesimally short sections of length Δz, for each of which the assumption of lumped elements can be justified again. Each section is modeled by a series resistance $R = R'\Delta z$, a series inductance $L = L'\Delta z$, a parallel capacitance $C = C'\Delta z$ and a parallel conductance $G = G'\Delta z$. The quantities R', L', G' and C' are thus differential quantities that describe the resistance, inductance, conductance and capacitance of the transmission line per length in Ω/m, H/m, S/m and F/m, respectively. The following derivation of useful relations and quantities describing a transmission line is based on the textbook "Microwave engineering" by D. M. Pozar [87].

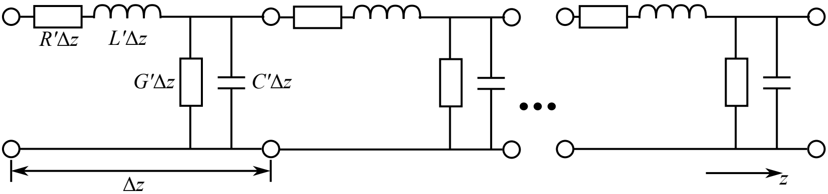

Fig. 2.9: Equivalent circuit of a transmission line divided into infinitesimally short sections of length Δz. Each section is modeled by a series resistance $R = R'\Delta z$, a series inductance $L = L'\Delta z$, a parallel capacitance $C = C'\Delta z$ and a parallel conductance $G = G'\Delta z$. The quantities R', L', G' and C' are thus differential quantities that describe the resistance, inductance, conductance and capacitance of the transmission line per length in Ω/m, H/m, S/m and F/m, respectively.

2.5.2 Telegrapher equation and characteristic impedance

The time dependent voltages $u(z,t)$ and currents $i(z,t)$ along the transmission line are determined by the telegrapher equations [87]:

$$\frac{\partial u(z,t)}{\partial z} = -R' i(z,t) - L' \frac{\partial i(z,t)}{\partial t} \tag{2.33}$$

and

$$\frac{\partial i(z,t)}{\partial z} = -G' u(z,t) - C' \frac{\partial u(z,t)}{\partial t}. \tag{2.34}$$

For time-harmonic currents $i(z,t) = \Re\{I(z)\exp(\mathrm{j}\omega t)\}$ and voltages $u(z,t) = \Re\{U(z)\exp(\mathrm{j}\omega t)\}$, the telegrapher equations 2.33 and 2.34 simplify to

$$\frac{dU(z)}{dz} = -(R' + j\omega L')I(z), \tag{2.35}$$

$$\frac{dI(z)}{dz} = -(G' + j\omega C')U(z). \tag{2.36}$$

Combining Eq. 2.35 and Eq. 2.36 yields wave equations of the form

$$\frac{d^2U(z)}{dz^2} - \gamma^2 U(z) = 0, \tag{2.37}$$

$$\frac{d^2I(z)}{dz^2} - \gamma^2 I(z) = 0, \tag{2.38}$$

with the complex propagation parameter $\gamma = \sqrt{(R' + j\omega L')(G' + j\omega C')}$. These wave equations are solved by a superposition of forward and backward traveling waves

$$U(z) = U_0^+ \mathrm{e}^{-\gamma z} + U_0^- \mathrm{e}^{\gamma z}, \tag{2.39}$$

$$I(z) = I_0^+ \mathrm{e}^{-\gamma z} + I_0^- \mathrm{e}^{\gamma z}. \tag{2.40}$$

The terms $U_0^+ \mathrm{e}^{-\gamma z}$ and $I_0^+ \mathrm{e}^{-\gamma z}$ describe the forward traveling waves and $U_0^- \mathrm{e}^{\gamma z}$ and $I_0^- \mathrm{e}^{\gamma z}$ describe the backward traveling waves.

The propagation parameter can be written as $\gamma = \alpha + \mathrm{j}\beta$, where α represents an attenuation of the amplitude of the propagating wave[2] and β the effective propagation index. The complex propagation parameter γ describes how current and voltage change along the transmission line. Additionally, we can define the characteristic impedance

$$Z_0 = \frac{R' + \mathrm{j}\omega L'}{\gamma} = \sqrt{\frac{R' + \mathrm{j}\omega L'}{G' + j\omega C'}} \tag{2.41}$$

which relates current and voltage to one another as

$$I(z) = \frac{1}{Z_0}\left(U_0^+ \mathrm{e}^{-\gamma z} - U_0^- \mathrm{e}^{\gamma z}\right). \tag{2.42}$$

Note that both γ and Z_0 are generally complex[3] and independent of the length of a transmission line. They are fully determined by R', L', C', and G', which are dictated by the physical cross-section of the transmission line. Signal propagation along a transmission line is thus fully described by the length ℓ,

---

[2] Note that α denotes an amplitude attenuation coefficient. The corresponding power attenuation coefficient, in this work denoted as $\alpha^{(\mathrm{pwr})}$ and often used in optics, amounts to 2α.

[3] Oftentimes the characteristic impedance is considered in the context of low-loss transmission lines at high frequencies so that $Z_0 \approx \sqrt{L'/C'}$ and therefore $Z_0 \in \mathbb{R}$. This approximation does only hold if $R' \ll \omega L'$ and $G' \ll \omega C'$.

the characteristic impedance Z_0 and the complex propagation constant γ of the line.

For a transmission line of finite length, the amplitudes of the forward and backward-propagating waves $U^\pm$ and $I^\pm$ depend on the boundary conditions at the start and the end of the line. In all relevant scenarios, the transmission line with characteristic impedance Z_0 is not isolated but embedded in a network. Generally, we consider an input network with the source impedance Z_{src} and an output network with load impedance Z_{L}. If $Z_0 \neq Z_{\mathrm{src}}$ and $Z_0 \neq Z_{\mathrm{L}}$ the propagating waves are (partially) reflected at the boundary to the input network and at the boundary to the output network, respectively. The amplitude reflection factor at such an impedance mismatch between impedance Z_i and Z_j is

$$\Gamma = \frac{Z_i - Z_j}{Z_i + Z_j}. \tag{2.43}$$

2.5.3 Matrix description of transmission line

A linear two-port network can be described using a two-dimensional matrix relating wave amplitudes at the input port to wave amplitudes at the output port. Figure 2.10 shows a schematic of a two-port network (e.g. a transmission line) with current I_i and voltage U_i at port i. The quantity U_i^+ is the amplitude of the voltage wave incident at port i, and U_i^- is the voltage wave emitted from port i, including also partial reflection of the incident wave. Two-port representations used in this work include the transfer-matrix $\mathbf{T}$ (often referred to as *ABCD*-matrix in microwave engineering[4]), relating the voltages and currents at port 1 to the voltages and currents at port 2:

$$\begin{pmatrix} U_1 \\ I_1 \end{pmatrix} = \underbrace{\begin{pmatrix} T_{11} & T_{12} \\ T_{21} & T_{22} \end{pmatrix}}_{\mathbf{T}} \begin{pmatrix} U_2 \\ I_2 \end{pmatrix}. \tag{2.44}$$

---

[4] Not to be confused with the matrix used in optics for ray transfer matrix analysis.

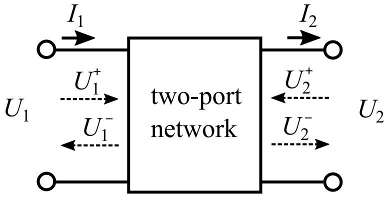

Fig. 2.10: Schematic representation of two-port network.

The transmission-matrix representation of a two-port is particularly useful because a cascade of two-ports described individually by $\mathbf{T_1}$, $\mathbf{T_2}$,...,$\mathbf{T_n}$ can be represented by the multiplication of all transmission matrices $\mathbf{T}_{\text{cascade}} = \mathbf{T_1}\mathbf{T_2}\ldots\mathbf{T_n}$.

An alternative representation is the frequently used scattering matrix $\mathbf{S}$, the elements of which are referred to as S-parameters. The scattering matrix relates the incident voltage waves U_i^+ to the reflected or transmitted voltage waves U_i^-:

$$\begin{pmatrix} U_1^- \\ U_2^- \end{pmatrix} = \underbrace{\begin{pmatrix} S_{11} & S_{22} \\ S_{21} & S_{22} \end{pmatrix}}_{\mathbf{S}} \begin{pmatrix} U_1^+ \\ U_2^+ \end{pmatrix}. \tag{2.45}$$

The individual matrix elements are given by

$$S_{ij} = \left.\frac{U_i^-}{U_j^+}\right|_{U_k^+=0 \text{ for } k\neq j}. \tag{2.46}$$

S-parameter are particularly useful because they can be easily measured using a vector network analyzer (VNA) and they can be generalizing, using the concept of power waves, for systems where voltages and currents are no longer defined (e.g. hollow-core waveguides) [87, 88]. If the reference impedance Z_{ref} of the measurement system (usually $50\,\Omega$) is known, a transmission line can be fully described by its S-parameters. For a transmission line of length ℓ, the following relation is useful to express **T** in terms of the transmission lines characteristic impedance Z_0 and its complex propagation parameter γ [89]:

$$\mathbf{T} = \begin{pmatrix} \cosh(\gamma\ell) & Z_0 \sinh(\gamma\ell) \\ \frac{1}{Z_0}\sinh(\gamma\ell) & \cosh(\gamma\ell) \end{pmatrix} \tag{2.47}$$

so that

$$Z_0 = \sqrt{\frac{T_{12}}{T_{21}}} \tag{2.48}$$

and

$$\gamma = \frac{1}{\ell}\operatorname{arcosh}(T_{11}). \tag{2.49}$$

To convert the S-matrix representation of a two-port into the equivalent T-matrix representation, the following relations are used [87, 89]:

$$\begin{aligned} T_{11} &= \frac{1 + S_{11} - S_{22} - \Delta S}{2S_{21}} \\ T_{12} &= Z_{\mathrm{ref}}\frac{1 + S_{11} + S_{22} + \Delta S}{2S_{21}} \\ T_{21} &= \frac{1}{Z_{\mathrm{ref}}}\frac{1 - S_{11} - S_{22} + \Delta S}{2S_{21}} \\ T_{22} &= \frac{1 - S_{11} + S_{22} - \Delta S}{2S_{21}} \end{aligned} \tag{2.50}$$

where $\Delta S = S_{11}S_{22} - S_{21}S_{12}$. Consequently, if a transmission line is characterized by obtaining **S** through a measurement and if both Z_{ref} and l are known, the relations Eqs. 2.50, 2.48, and 2.49 can be used to obtain Z_0 and γ.

2.5.4 Voltage along a terminated lossy transmission line

Figure 2.11 shows a transmission line of length ℓ, characteristic impedance Z_0, and complex propagation constant γ as defined in Eq. 2.40. The line is fed with a signal from a source generating an open-circuit voltage U_{src}. The source impedance is Z_{src} and the line is terminated with an impedance Z_{trm}.

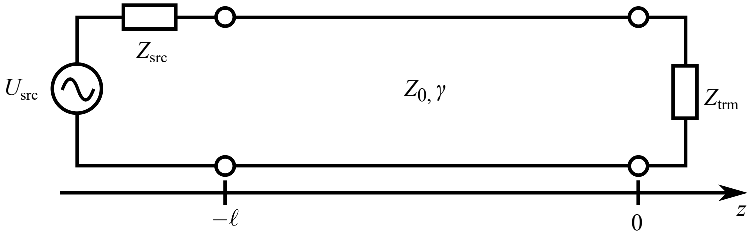

Fig. 2.11: Schematic representation of a transmission line of length ℓ connected to a source with an internal source impedance Z_{src} and a terminating impedance Z_{trm}. The transmission line has a characteristic impedance Z_0 and a complex propagation constant γ.

The reflection coefficients as seen from the transmission line at both ends of the transmission line are

$$\Gamma_{\mathrm{trm}} = \frac{Z_{\mathrm{trm}} - Z_0}{Z_{\mathrm{trm}} + Z_0} \tag{2.51}$$

and

$$\Gamma_{\mathrm{src}} = \frac{Z_{\mathrm{src}} - Z_0}{Z_{\mathrm{src}} + Z_0}. \tag{2.52}$$

Due to reflections at both ends of the transmission line the voltage U at each point z along the transmission line is composed of a forward-traveling[5] and a backward-traveling component as in Eq. 2.39

$$U(z) = U_0^{+} \mathrm{e}^{-\gamma z} + U_0^{-} \mathrm{e}^{\gamma z}, \tag{2.53}$$

with $U_0^{-} = \Gamma_{\mathrm{trm}} U_0^{+}$, so that

$$U(z) = U_0^{+} \mathrm{e}^{-\gamma z} + \Gamma_{\mathrm{trm}} U_0^{+} \mathrm{e}^{\gamma z}. \tag{2.54}$$

To determine U_0^{+}, we consider $U(z)$ at the position $z = -\ell$,

$$U(-\ell) = U_{\mathrm{src}} \frac{Z_{\mathrm{in}}}{Z_{\mathrm{in}} + Z_{\mathrm{src}}}, \tag{2.55}$$

---

[5] “Forward-traveling” corresponds to a wave propagating in the positive z-direction of the axis defined in Fig. 2.11. Note that the transmission line extends from a negative z-value at $z = -\ell$ to $z = 0$.

with Z_{in} being the input impedance seen at $z = -\ell$ looking into the transmission line terminated with Z_{trm}, see Eq. 2.90 in [87],

$$Z_{\text{in}} = \frac{U(-l)}{I(-\ell)}) = Z_0 \frac{\mathrm{e}^{\gamma\ell} + \Gamma_{\text{trm}}\mathrm{e}^{-\gamma\ell}}{\mathrm{e}^{\gamma\ell} - \Gamma_{\text{trm}}\mathrm{e}^{-\gamma\ell}}. \tag{2.56}$$

From Eq. 2.54 and 2.55, we find

$$U_0^+ = U_{\text{src}} \frac{Z_{\text{in}}}{Z_{\text{in}} + Z_{\text{src}}} \frac{1}{\mathrm{e}^{\gamma\ell} + \Gamma_{\text{trm}}\mathrm{e}^{-\gamma\ell}} = U_{\text{src}} \frac{Z_0}{Z_0 + Z_{\text{src}}} \frac{1}{\mathrm{e}^{\gamma\ell} - \Gamma_{\text{trm}}\Gamma_{\text{src}}\mathrm{e}^{-\gamma\ell}}, \tag{2.57}$$

and the voltage along the transmission line is found to be

$$U(z) = U_{\text{src}} \frac{Z_0}{Z_0 + Z_{\text{src}}} \frac{\mathrm{e}^{-\gamma z} + \Gamma_{\text{trm}}\mathrm{e}^{\gamma z}}{\mathrm{e}^{\gamma l} - \Gamma_{\text{trm}}\Gamma_{\text{src}}\mathrm{e}^{-\gamma l}}. \tag{2.58}$$

Note that Eq. 2.58 corresponds to Eq. 3 in [90] if the coordinate system is transformed accordingly.

2.5.5 Traveling-wave electro-optic modulators

In a traveling-wave EO phase modulator, the modulating RF signal guided by an electrical transmission line travels along with the optical signal. The interaction between RF wave and optical wave depends on the propagation speed of both the RF signal and of the optical signal. The effective optical group index is $n_{\text{g,opt}}$ and thus the group velocity of the optical signal is given by $v_{\text{g,opt}} = \mathrm{c}/n_{\text{g,opt}}$. In an EO modulator based on the Pockels effect, the local phase shift increases in proportion to the local modulation voltage, see Eq. 2.17. The traveling-wave modulator can be considered as a transmission line for the modulating voltage. If a sinusoidal voltage with angular frequency ω_{RF} is applied, the modulating voltage along the modulator is given by Eq. 2.58. In the following analysis, we express the total sinusoidally varying phase shift $\varphi(t)$ that an optical signal accumulates along the modulator as

$$\varphi(t) = \Re\left\{\hat{\varphi}(\omega_{\text{RF}})\mathrm{e}^{\mathrm{j}\omega_{\text{RF}}t}\right\}, \tag{2.59}$$

where the complex amplitude $\hat{\varphi}(\omega_{\mathrm{RF}})$ contains both the frequency dependent amplitude and the phase of the phase shift.

To calculate the total phase shift $\varphi(t)$, the modulating voltage seen by the optical signal has to be integrated along the phase shifter length ℓ [90]

$$\hat{\varphi}(\omega_{\mathrm{RF}})\mathrm{e}^{\mathrm{j}\omega_{\mathrm{RF}}t} \propto \frac{1}{\ell}\int_{-\ell}^{0} u(z,t')\,\mathrm{d}z = \frac{1}{\ell}\int_{-\ell}^{0} U(z)\mathrm{e}^{j\omega_{\mathrm{RF}}t'}\,\mathrm{d}z, \tag{2.60}$$

where $U(z)$ is given by Eq. 2.58 and t' is a retarded time given by

$$t' = \frac{z+\ell}{v_{\mathrm{g,opt}}} + t. \tag{2.61}$$

The time t' corresponds to the time at which the optical signal which has entered the modulator at time t at the position $z = -\ell$ reaches the position z.

We can then combine Eq. 2.58, 2.60 and 2.61 to get

$$\begin{aligned}
&\hat{\varphi}(\omega_{\mathrm{RF}})\mathrm{e}^{\mathrm{j}\omega_{\mathrm{RF}}t} \propto \\
&\frac{U_{\mathrm{src}}}{\ell}\frac{Z_0}{Z_0+Z_{\mathrm{src}}}\frac{1}{\mathrm{e}^{\gamma\ell}-\Gamma_{\mathrm{trm}}\Gamma_{\mathrm{src}}\mathrm{e}^{-\gamma\ell}}\int\limits_{-\ell}^{0}(\mathrm{e}^{-\gamma z}+\Gamma_{\mathrm{trm}}\mathrm{e}^{\gamma z})\,\mathrm{e}^{\mathrm{j}\omega_{\mathrm{RF}}t'}\mathrm{d}z \\
=&\frac{U_{\mathrm{src}}}{\ell}\frac{Z_0}{Z_0+Z_{\mathrm{src}}}\frac{\mathrm{e}^{\mathrm{j}\omega_{\mathrm{RF}}t}}{\mathrm{e}^{\gamma\ell}-\Gamma_{\mathrm{trm}}\Gamma_{\mathrm{src}}\mathrm{e}^{-\gamma\ell}}\int\limits_{-\ell}^{0}(\mathrm{e}^{-\gamma z}+\Gamma_{\mathrm{trm}}\mathrm{e}^{\gamma z})\,\mathrm{e}^{\mathrm{j}\omega_{\mathrm{RF}}(z+\ell)/v_{\mathrm{g,opt}}}\mathrm{d}z.
\end{aligned} \tag{2.62}$$

Multiplying both sides of Eq. 2.62 with $\mathrm{e}^{-\mathrm{j}\omega_{\mathrm{RF}}\mathrm{t}}$ yields the complex phase amplitude as

$$\begin{aligned}
&\hat{\varphi}(\omega_{\mathrm{RF}}) \propto \\
&\frac{U_{\mathrm{src}}}{\ell}\frac{Z_0}{Z_0+Z_{\mathrm{src}}}\frac{1}{\mathrm{e}^{\gamma\ell}-\Gamma_{\mathrm{trm}}\Gamma_{\mathrm{src}}\mathrm{e}^{-\gamma\ell}}\int\limits_{-\ell}^{0}(\mathrm{e}^{-\gamma z}+\Gamma_{\mathrm{trm}}\mathrm{e}^{\gamma z})\,\mathrm{e}^{\mathrm{j}\omega_{\mathrm{RF}}(z+\ell)/v_{\mathrm{g,opt}}}\mathrm{d}z.
\end{aligned} \tag{2.63}$$

The frequency response of the phase modulator $\tilde{m}_{\mathrm{PH}}$ is given by the phase amplitude $\hat{\varphi}(\omega_{\mathrm{RF}})$, typically normalized by $\hat{\varphi}(0)|_{Z_{\mathrm{src}}=Z_{\mathrm{trm}}=Z_0}$ [90]

$$\tilde{m}_{\mathrm{PH}}(\omega_{\mathrm{RF}}) = \frac{\hat{\varphi}(\omega_{\mathrm{RF}})}{\hat{\varphi}(0)|_{Z_{\mathrm{src}}=Z_{\mathrm{trm}}=Z_0}} = A\left(\frac{\mathrm{e}^{q^{-}\ell}-1}{q^{-}} + B\frac{\mathrm{e}^{q^{+}\ell}-1}{q^{+}}\right), \tag{2.64}$$

with

$$A = \frac{2}{\ell}\frac{Z_0}{Z_0+Z_{\mathrm{src}}}\frac{1}{1-\Gamma_{\mathrm{trm}}\Gamma_{\mathrm{src}}\mathrm{e}^{-2\gamma\ell}} \tag{2.65}$$

$$B = \mathrm{e}^{-2\gamma\ell}\Gamma_{\mathrm{trm}} \tag{2.66}$$

$$q^{-} = -\gamma + \frac{\mathrm{j}\omega_{\mathrm{RF}}}{v_{\mathrm{g,opt}}} \tag{2.67}$$

$$q^{+} = \gamma + \frac{\mathrm{j}\omega_{\mathrm{RF}}}{v_{\mathrm{g,opt}}}. \tag{2.68}$$

Equation 2.64 is equivalent to the expression given in [90], Eq. 3, for a modulator in which the active phase-shifter section occupies to the entire length l of the transmission line. Equation 2.64 generally describes the frequency response of a traveling-wave phase modulator and comprises the bandwidth-limiting effects of velocity mismatch, impedance mismatch and microwave loss of the transmission line. The second expression in Eq. 2.64 describes the contribution of a backwards-traveling wave and becomes zero for a perfectly terminated modulator with $Z_{\mathrm{trm}} = Z_0$. If an MZM comprises traveling-wave phase modulators as described by Eq. 2.64, which are additionally configured in push-pull configuration and biased at the 3 dB-point, the small-signal intensity frequency response $m_{\mathrm{EOE}}(\omega_{\mathrm{RF}})$ is given by the same expression as Eq. 2.64, see Section 3.2. For slot-waveguide-based modulators the additional capacitive loading of the metal transmission line by the slot waveguide can lead to a further reduction of the bandwidth. This is because the voltage that becomes effective in the slot can deviate from the voltage $U(z)$ across the transmission line due to the reduction by the voltage divider formed by the resistive slab and the slot capacitance [91], see Section 3.2. A detailed discussion of the impact of velocity mismatch, impedance mismatch, microwave loss, and RC limitation in the case of SOH modulators is given in Chapter 3.

2.6 Optical modulation formats for digital communications

In fiber-based optical communication, information is transmitted by encoding data onto an optical carrier, which is then sent, e.g., through an optical fiber. For single-mode silica fibers, the vacuum wavelength of the carrier lies most often in the so-called C-band with wavelengths between 1.45 µm and 1.65 µm [35]. The tremendous bandwidth of 25 THz available in this wavelength window along with the low propagation loss of modern single-mode silica fibers is the reason why optical communication is used to transmit broadband data signals.

To generate the monochromatic optical carrier with angular frequency ω_0, lasers are used. To encode data, one or several of the following physical attributes of the optical field propagating in the single-mode fiber can be used: the intensity, the phase, and the polarization. Encoding information in the polarization is used in so-called polarization switched modulation formats but not considered here. The polarization degree of freedom is also used in polarization division multiplexing (PDM) systems to increase the spectral efficiency by transmitting independent data on two carriers with the same wavelength but orthogonal polarization states. In the following we restrict ourselves to linearly polarized carriers with a scalar electric field represented by

$$E(t) = \Re\left\{A(t)\exp(\mathrm{j}\omega_0 t)\right\} \tag{2.69}$$

with a “slowly varying” and generally complex amplitude $A(t)$. To encode information by modulation, the laser could be directly modulated. In practice, this allows modulating the intensity, but it gives no independent control over the phase. Further, for directly modulated lasers, the modulation speed is limited and phase- and amplitude modulation are inherently linked, which leads to chirp in intensity-modulated signals [35]. External modulation of the carrier using an MZM in push-pull configuration allows modulating the amplitude or intensity only, without residual phase modulation, see Section 2.2.1. Using an IQ modulator for external modulation allows to independently control the amplitude and the phase of the carrier, see Section 2.2.2.

In digital communications, the information is encoded using an alphabet $\{a_k\}$ comprising M symbols a_k with $k = 1, \ldots, M$. Each symbol can contain a maximum of $m = \log_2 M$ bit of information. To transmit the abstract alphabet over a physical channel, e.g. an optical fiber, a set of analogue waveforms $p_k(t)$ has to be assigned to the symbols a_k. A time-continuous signal consisting of symbols at a symbol rate $f_\mathrm{s} = 1/T_\mathrm{s}$ with symbol duration T_s can then be written as

$$s(t) = \sum_{i=-\infty}^{\infty} p_{k(i)}(t - iT_\mathrm{s}), \tag{2.70}$$

and a modulator can be used to encode the signal $s(t)$ onto the optical carrier such that $A(t) = s(t)$.

The unit of the symbol rate is "baud" (Bd), defined as 1 Bd = 1 symbol/s. If each symbol carries $m = \log_2 M$ bit information, the line rate f_d in bit/s is given by

$$f_\mathrm{d} = m f_\mathrm{s}. \tag{2.71}$$

In many cases of practical interest, the same analogue pulse shape is used for all symbols, and we can write $p_k(t) = a_k p(t)$.

We now consider the most commonly used optical modulation formats, which can be categorized into intensity modulation formats, where information is represented only by the intensity (power) of the optical signal, and coherent modulation formats, where the phase of the optical signal is used as an additional carrier of information.

In intensity modulation formats, different intensity levels are used to create the letters of an alphabet. A photodiode in the receiver can then directly convert the optical signal back into an electrical signal. Modulation formats using only intensity modulation and direct detection by a single photodiode are therefore referred to as intensity-modulation and direct-detection (IM/DD) formats. The simplest case of intensity modulation is so-called "On-Off"-keying (OOK), where 1 bit information is encoded per symbol, using a symbol represented by a high optical intensity and a symbol represented by a low (usually zero) optical intensity. Mathematically, the alphabet for OOK is given by

$$a_{k,\mathrm{OOK}} = \{0, 1\}, \tag{2.72}$$

which represents two states with amplitude 0 and 1. A frequently used graphical representation of the symbol alphabet is a so-called constellation diagram, where the symbol alphabet is visualized by points in the complex plane. Figure 2.12(a) shows the constellation diagram of an OOK signal with the two amplitude levels given by Eq, 2.72. An example of an eye-diagram of the corresponding optical intensity I_{opt} is shown in Fig. 2.12(b).

To increase the number of bits per symbol, additional signal levels can be introduced. This increases the spectral efficiency, but the noise resilience is reduced. In four-level pulse-amplitude modulation (PAM4), four equally spaced intensity levels are used, represented by the alphabet

$$a_{k,\mathrm{PAM4}} = \left\{0, \sqrt{\frac{1}{3}}, \sqrt{\frac{2}{3}}, 1\right\}. \tag{2.73}$$

The corresponding amplitude and intensity levels are shown in the constellation diagram and eye diagram in Fig. 2.12(c) and Fig. 2.12(d), respectively.

An alternative approach to increase the spectral efficiency is the use of correlative coding, where a correlation between symbols is introduced. Chapter 4 provides a detailed introduction into intensity-modulated duobinary (IDB), an IM/DD correlative coding format. A side-to-side comparison of the three important IM/DD formats OOK, PAM4, and IDB in terms of spectral efficiency, signal-to-noise-ratio (SNR) tolerance and technical complexity can be found in Section 4.7.

Coherent modulation formats, encoding information in both the amplitude and the phase of the optical carrier, are nowadays widely used to increase the spectral efficiency beyond the limitations of the technically simple IM/DD techniques. The use of two orthogonal attributes of the optical field allows to double the spectral efficiency compared to intensity modulation. This comes at the cost of a more complex system consisting of a modulator that is capable of independent phase and amplitude modulation at the transmitter (e.g. an IQ-modulator, see Section 2.2.2) and a coherent receiver that allows to receive both, the phase and the amplitude of the received signal by homodyne, intradyne or heterodyne reception.

In many cases of practical interest, so-called quadrature-amplitude modulation (QAM) is used as coherent optical modulation format. It uses a two-dimensional symbol alphabet constructed in the “quadrature space”, composed

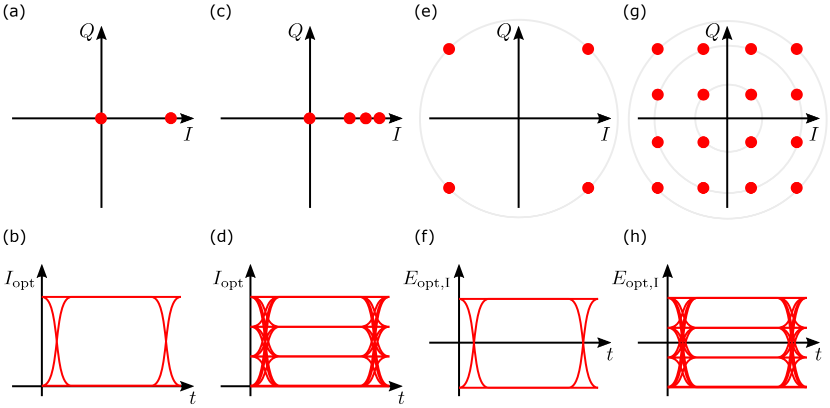

Fig. 2.12: Optical modulation formats. Intensity modulation formats encode information into the intensity of an optical carrier. The simplest form is on-off-keying (OOK) with only two intensity levels. (a) Constellation diagram of the corresponding two amplitude levels. (b) The intensity eye-diagram of the OOK signal is shown for a raised-cosine pulse shape. Increasing the number of intensity levels allows increasing the spectral efficiency. (c) Constellation diagram and (d) intensity eye-diagram for four-level pulse-amplitude modulation (PAM4). If information is encoded in both the amplitude and the phase of the optical signal, the constellation becomes two-dimensional and a phase-sensitive coherent receiver is required. (e) Constellation diagram of a quadrature-phase-shift-keying (QPSK) modulation format and (f) the corresponding amplitude eye-diagram for the I component. (g) Constellation diagram for a 16-state quadrature-amplitude modulation (16QAM) format. (h) Corresponding amplitude eye-diagram for I component of the 16QAM signal.

from the in-phase (I) component and the quadrature (Q) component of the electric field. So-called QPSK uses four symbols given by

$$a_{k,\mathrm{QPSK}} = \{1+\mathrm{j}, -1+\mathrm{j}, -1-\mathrm{j}, 1-\mathrm{j}\}\,. \tag{2.74}$$

The corresponding constellation diagram is depicted in Fig 2.12(e). A coherent receiver allows separating the I- and Q-component of the signal, and the amplitude eye-diagram of the isolated I-component is shown in Fig. 2.12(f). Analogously to the quaternary QPSK alphabet, M-ary quadrature-amplitude-modulation (M-QAM) formats map symbols to M states in the two-dimensional I-Q-space. The example of 16-state quadrature amplitude modulation (QAM) is depicted in Fig. 2.12(g) and (e) in form of the constellation diagram and the amplitude eye-diagram of the I component.

3 Model of traveling-wave SOH modulators

This chapter reports on the formulation and the experimental verification of a model describing the dynamic EO behavior of SOH modulators. The model is used to extract design guidelines for SOH modulators. This chapter was published in a scientific journal [J1]. The material from the publication was adapted to comply with the layout and the structure of this thesis.

[Beginning of Paper [J1]. Reprinted with permission ©The Optical Society.]

A verified equivalent-circuit model for slot-waveguide modulators

Optics Express, Vol. 28, Issue 9, pp. 12951-12976 (2020)

DOI: `https://doi.org/10.1364/OE.383120`

Heiner Zwickel,[1] Stefan Singer,[1] Clemens Kieninger,[1,2] Yasar Kutuvantavida,[1,2] Narek Muradyan,[1] Thorsten Wahlbrink,[3] Shiyoshi Yokoyama,[4] Sebastian Randel,[1] Wolfgang Freude,[1] and Christian Koos[1,2]

[1] Institute of Photonics and Quantum Electronics (IPQ), Karlsruhe Institute of Technology (KIT), Germany

[2] Institute of Microstructure Technology (IMT), Karlsruhe Institute of Technology (KIT), Germany

[3] AMO GmbH, 52074 Aachen, Germany

[4] Institute for Materials Chemistry and Engineering, Kyushu University, Japan

We formulate and experimentally validate an equivalent-circuit model based on distributed elements to describe the electric and electro-optic (EO) properties of traveling-wave silicon-organic hybrid (SOH) slot-waveguide modulators. The model allows to reliably predict the small-signal EO frequency response of the modulators exploiting purely electrical measurements of the frequency-

dependent RF transmission characteristics. We experimentally verify the validity of our model, and we formulate design guidelines for an optimum trade-off between optical loss due to free-carrier absorption (FCA), electro-optic bandwidth, and π-voltage of SOH slot-waveguide modulators.

3.1 Introduction

Broadband efficient EO modulators are key elements for a wide variety of applications, ranging from high-speed optical communications [40,70,71,86,92,93] to ultra-fast signal processing [80, 94] and further to optical metrology and sensing [95, 96]. Among the various technology platforms that are available today, SiP represents a particularly promising option, exploiting mature CMOS fabrication processes for cost-efficient mass production of densely integrated photonic circuits [23,24,97]. When it comes to EO modulators, hybrid combinations of SiP slot waveguides with highly efficient organic EO cladding materials are an attractive approach to overcome the intrinsic lack of second-order optical nonlinearities in bulk silicon [17]. Exploiting theory-guided optimization of organic EO materials on a molecular level [98], SOH devices primarily stand out due to small voltage-length products down to 0.32 Vmm [18] – more than an order of magnitude below that of conventional depletion-type SiP modulators [16]. SOH devices have been demonstrated to offer attractive performance parameters such as EO bandwidths of 100 GHz [81] as well as line rates of up to 120 Gbit/s for intensity modulation [86, 99] and up to 400 Gbit/s for coherent 16QAM signaling [93], while supporting driver-less operation with sub-1 V drive signals obtained from binary outputs of a standard CMOS field-programmable gate array (FPGA) [100]. However, the EO bandwidth of these devices is still subject to large uncertainties. In addition, most of the aforementioned experiments [81, 86, 93, 99, 101] relied on a so-called gate voltage that is applied across the BOX of the underlying SOI substrate to induce a highly conductive electron accumulation layer that reduces the RC time constant of the slot waveguide [85]. Moreover, an experimentally verified model describing the EO frequency response of SOH modulators is still lacking, which represents a major obstacle towards a targeted design of the modulator structures and of the associated drive circuitry.

In this paper, we formulate and experimentally verify a reliable quantitative model of slot-waveguide modulators that accounts for the various bandwidth-limiting effects. We build upon an equivalent-circuit approach proposed by Witzens *et al.* [91], which relies on a distributed-element description of the slot-waveguide structure and of the associated RF transmission line. We refine this model and verify it quantitatively using experimental data obtained from SOH devices. We find that the model accurately predicts the EO frequency response of a slot-waveguide modulator based on purely electrical RF characteristics of the device, which are easily accessible by measurements. Our model allows to identify non-optimum doping profiles as the main reason for a limited EO bandwidth of our current device generation. Based on these findings, we extract design rules that lead to an optimum trade-off between optical loss due to free-carrier absorption (FCA), EO bandwidth, and π-voltage. Optimized device designs should lead to sub-1 mm Mach-Zehnder modulators (MZMs) with π-voltages smaller than 1 V, EOE bandwidths larger than 100 GHz, and FCA-induced optical losses below 0.1 dB. To the best of our knowledge, this work represents the first experimental validation of a general model of slot-waveguide modulators. We believe that quantitatively reliable models represent a key step towards fast and reliable design and efficient wafer-level characterization of slot-waveguide modulators which are embedded into complex optical systems and RF drive circuits.

This chapter is structured as follows: In Section 3.2, we introduce the concept of SOH modulators and formulate a model based on distributed elements. In Section 3.3, we discuss S-parameter measurements of SOH modulators, extract the characteristic impedance and the RF propagation parameter, and determine the parameters of the equivalent RF circuit by a least-squares fit. In Section 3.4, we validate the model by comparing the measured EO frequency response to the model prediction using parameters extracted from purely electrical measurements. In Section 3.5, we summarize the findings and discuss design guidelines and achievable performance parameters of SOH EO modulators.

3.2 Device principle and model based on distributed-element equivalent circuit

The concept of a slot-waveguide SOH MZM is depicted in Figure 3.1 [49–51]. The MZM consists of two parallel phase shifter sections, which typically have a length ℓ between 0.5 mm and 1.5 mm, see Fig. 3.1(a). The electric drive signal is applied via a coplanar RF transmission line in GSG configuration. The device is realized as a traveling-wave structure, in which the modulating electric mode co-propagates with the optical mode. Each phase shifter comprises a silicon slot waveguide with a slot width typically between 60 nm and 160 nm, which is filled with a highly efficient organic EO material that may offer in-device EO coefficients in excess of 300 pm/V [18], see cross-section in Fig. 3.1(b). To activate the macroscopic EO activity in the slot, chromophores in the organic EO material have to be aligned in a one-time poling process, see [49, 102] for details. The rails of the slot waveguide are connected to the metal RF transmission line via thin, doped silicon slabs, such that the externally applied drive voltage predominantly drops across the narrow slot. At the same time, the optical mode is highly confined to the slot region, leading to a very strong interaction with the modulating electric field. The EO frequency response of SOH modulators strongly depends on the RC time constant that is associated with the slot capacitance and the slab resistance. A two-level doping profile as illustrated in Fig.3.1(b) can help to increase the bandwidth while maintaining acceptable optical loss [103, 104]: In the rails and near the slot, the doping concentration is kept low (light blue) to avoid excessive free-carrier absorption, while a higher doping concentration (dark blue) is used further away from the optical waveguide to increase the electric conductivity. The impact of increased slab conductivity can also be studied by applying a DC “gate” voltage U_{gate} between the substrate and the slabs. This induces a highly conductive electron accumulation layer at the interface between the Si slabs and the BOX [85].

For a quantitative description of the electric behavior of the SOH modulator, we adapt the model suggested in [91], which has also been adapted to model depletion-type pn-modulators [105–111]. Reference [91] is primarily focused on the design of phase-matched traveling-wave transmission lines, which is key to achieve broadband operation of MZMs with rather large interaction lengths ℓ of several millimeters. Over the previous years, however, substantial improvements of organic EO materials and in-device EO efficiencies [18] have

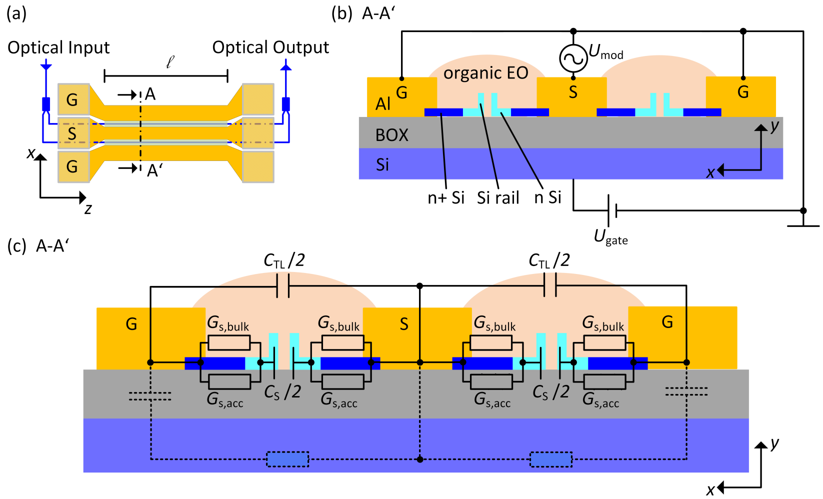

Fig. 3.1: Device concept and equivalent-circuit model. (a) Schematic top view of the Mach-Zehnder modulator (MZM) with metal electrodes (yellow) that form a coplanar ground-signal-ground electrical transmission line of length ℓ. The device is equipped with contact pads at both ends. The optical waveguide depicted in blue is split into two arms to realize the Mach-Zehnder interferometer. (b) Cross-section of the MZM along the line A-A’ indicated in Subfigure (a). Each arm comprises a SiP slot waveguide filled with an organic electro-optic (EO) material. The metal electrodes are connected to the rails of the slot waveguide via thin, doped Si slabs. A modulating voltage U_{mod}, applied to the signal electrode, drops mainly across the narrow slot. This leads to a strong electric field in the slot that changes the refractive index of the organic EO material and thus modulates the phase of the optical wave. The Si slabs are doped to increase the conductivity. A low doping concentration (light blue) is used near the slot to keep optical losses low. A higher doping concentration (dark blue) is used further away from the slot to achieve a low resistance of the slabs and to thus decrease the RC time constant of the modulator. In addition, a DC “gate” voltage U_{gate} can be applied between the substrate and the ground electrodes. This induces a highly conductive electron accumulation layer at the interface between the Si slabs and the burried-oxide-layer (BOX) and thus further decreases the RC time constant. (c) Enlarged cross-sectional view of the MZM along with the associated elements of an equivalent-circuit representation of the modulator. The capacitance of the slot is represented by a capacitor with capacitance $C_{\mathrm{S}}/2$. The finite conductivity of each slab is represented by two parallel conductances $G_{\mathrm{S,bulk}}$ and $G_{\mathrm{S,acc}}$ that account for the conductance of the bulk Si slab and of the accumulation layer formed by the gate voltage, respectively. The metal electrodes have a total capacitance C_{TL}.

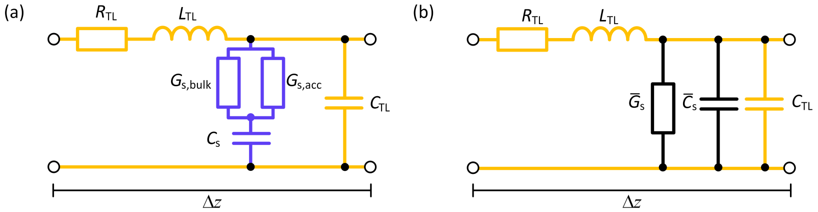

Fig. 3.2: Full equivalent-circuit model. (a) Equivalent-circuit model of an infinitesimally short element of the electrical transmission line formed by the MZM, shown in Fig. 3.1. The distributed elements shown in yellow correspond to the metal electrodes. The distributed elements shown in blue represent the additional RC shunt load formed by the slot waveguide. (b) Telegrapher-type equivalent-circuit representation of an MZM transmission-line element [91]. This representation is obtained by transforming the circuit in Subfigure (a), using a frequency-dependent shunt conductance $\overline{G}_\mathrm{S}$ and a frequency-dependent shunt capacitance $\overline{C}_\mathrm{S}$ see Eq. 3.2 and Eq. 3.3.

allowed to significantly reduce the interaction length. This renders phase-matching less crucial and requires adapted design considerations that focus on the RC time constant of the slab/slot configuration and on the associated trade-off with respect to optical loss.

In our analysis, we rely on a distributed-element model of the underlying RF transmission line, see Fig. 3.1(c) for a cross-sectional view with elements of an equivalent circuit representing an infinitesimally short transmission-line section of length Δz. The full equivalent circuit is shown in Fig. 3.2(a). First, we consider the circuit elements depicted in yellow in Fig. 3.2(a) that describe the coplanar GSG transmission line formed by the metal electrodes only, without the optical slot-waveguide structure. These circuit elements comprise a series resistance $R'_\mathrm{TL}\Delta z$, a series inductance $L'_\mathrm{TL}\Delta z$, and a shunt capacitance $C'_\mathrm{TL}\Delta z$, where R'_TL, L'_TL and C'_TL are differential quantities that describe the resistance, inductance, and capacitance of the GSG transmission line per length in Ω/m, H/m, and F/m, respectively. This corresponds to the classical telegrapher circuit with negligible shunt conductance. In a second step, we expand the equivalent circuit by the electrical representation of the Si structure (blue) forming the optical slot waveguide. For practical doping concentrations, the conductivity of the slabs is much smaller than that of the metal electrodes. As a consequence, the longitudinal currents can be assumed to be confined to the metal electrodes, whereas the currents in the silicon slabs flow predominantly in the transverse (x) direction between the electrodes and the slot. These assumptions are in accordance with findings from finite-element simulations [91] and allow us to model the electrical behavior of the optical slot waveguide by simply adding an RC shunt to the equivalent circuit [91,105,112]. The associated elements are the differential capacitance C'_S of the pair of slots, the differential conductance $G'_\mathrm{S,bulk}$ of the resistive Si slabs to both sides of each of the slot waveguides, and the differential conductance $G'_\mathrm{S,acc} = g'_\mathrm{S,acc} U_\mathrm{gate}$, which accounts for the increased conductance of an accumulation layer that may be induced by applying a gate voltage U_gate. Note that the capacitance between center signal electrode and each of the ground electrodes amounts to $C_\mathrm{TL}/2$, and that the overall shunt capacitance of the metal electrodes forming the coplanar GSG transmission line is hence $C_\mathrm{TL} = C'_\mathrm{TL}\Delta z$. Similarly, $C_\mathrm{S}/2$ is the capacitance of an individual slot, and $C_\mathrm{S} = C'_\mathrm{S}\Delta z$ represents the combination of both slots. The quantities $G_\mathrm{S,bulk} = G'_\mathrm{S,bulk}\Delta z$ and $G_\mathrm{S,acc} = G'_\mathrm{S,acc}\Delta z$ refer to the slab conductance to either side of each slot, and the equivalent circuit-element in Fig. 3.2(a) represents the combined effect of four slabs. The total differential conductance is $G'_\mathrm{S} = G'_\mathrm{S,bulk} + G'_\mathrm{S,acc}$. The two slot waveguides thus create a differential shunt admittance $\underline{Y}'_\mathrm{S}$ given by[1]

$$\frac{1}{\underline{Y}'_\mathrm{S}} = \frac{1}{G'_\mathrm{S,bulk} + G'_\mathrm{S,acc}} + \frac{1}{\mathrm{j}\omega_\mathrm{RF} C'_\mathrm{S}}. \tag{3.1}$$

For completeness, we have also indicated additional elements by dashed lines in Fig. 3.1(c) that seem to be reasonable to include. These elements model an additional RC shunt that accounts for the finite resistance of the handle wafer and the capacitance created by the BOX. It turned out, however, that in our case the impact of this additional RC circuit is negligible despite the rather low substrate resistivity of about 20 Ωcm as specified by the wafer manufacturer. This additional RC shunt load is therefore disregarded in the following, but could be easily included if modified device or material choices would require an adapted model [105].

The overall circuit shown in Fig. 3.2(a) can be transformed into the circuit in Fig. 3.2(b) by introducing the frequency-dependent differential conductance

---

[1] [*Note: For clarity, complex quantities are indicated by an underbar in this chapter. This symbol decoration is omitted elsewhere for better readability.*]

$$\overline{G}'_{\mathrm{S}}(\omega_{\mathrm{RF}}) = \Re\left\{\underline{Y}'_{\mathrm{S}}\right\} \tag{3.2}$$

and the frequency-dependent differential capacitance

$$\overline{C}'_{\mathrm{S}}(\omega_{\mathrm{RF}}) = \frac{1}{\omega_{\mathrm{RF}}}\Im\left\{\underline{Y}'_{\mathrm{S}}\right\} \tag{3.3}$$

This circuit resembles that of a classical telegrapher-type transmission-line model, and the transmission line can thus be fully described by the complex propagation parameter $\underline{\gamma} = \alpha + \mathrm{j}\beta$ together with the complex characteristic impedance $\underline{Z}_0$ obtained from the well-known transmission-line equations [87]

$$\underline{\gamma} = \alpha + \mathrm{j}\beta = \sqrt{\left(R'_{\mathrm{TL}} + \mathrm{j}\omega_{\mathrm{RF}}L'_{\mathrm{TL}}\right)\left(\overline{G}'_{\mathrm{S}} + \mathrm{j}\omega_{\mathrm{RF}}\left(\overline{C}'_{\mathrm{S}} + C'_{\mathrm{TL}}\right)\right)} \tag{3.4}$$

$$\underline{Z}_0 = \sqrt{\frac{R'_{\mathrm{TL}} + \mathrm{j}\omega_{\mathrm{RF}}L'_{\mathrm{TL}}}{\overline{G}'_{\mathrm{S}} + \mathrm{j}\omega_{\mathrm{RF}}\left(\overline{C}'_{\mathrm{S}} + C'_{\mathrm{TL}}\right)}}. \tag{3.5}$$

Note that in these relations α denotes an amplitude attenuation coefficient. The corresponding power attenuation coefficient amounts to 2α.

For analyzing the EO interaction, we now consider a traveling-wave EO modulator with characteristic impedance $\underline{Z}_0$, complex RF propagation parameter $\underline{\gamma}$, optical group refractive index $n_{\mathrm{g,opt}}$ in the phase shifter, and active phase-shifter length ℓ. The device is connected to an RF source with impedance $\underline{Z}_{\mathrm{src}}$ and terminated by an impedance $\underline{Z}_{\mathrm{trm}}$. Due to the Pockels effect, the local optical phase shift increases in proportion to the local modulation voltage. If a sinusoidal voltage with angular frequency ω_{RF} is applied to the modulator's signal electrode, the total phase shift $\varphi(t) = \Re\left\{\hat{\varphi}(\omega_{\mathrm{RF}})\mathrm{e}^{\mathrm{j}\omega_{\mathrm{RF}}t}\right\}$ in each arm can then be obtained from an integral of the modulation voltage seen by the optical signal along the phase shifter length ℓ, see ref. [90], Eq. 2. In this relation, the complex amplitude $\hat{\varphi}(\omega_{\mathrm{RF}})$ contains both the frequency-dependent amplitude and the phase of the sinusoidally varying phase shift $\varphi(t)$. The complex frequency response $\underline{m}_{\mathrm{PH}}(\omega_{\mathrm{RF}})$ of such a phase modulator is given by the phase amplitude $\hat{\varphi}(\omega_{\mathrm{RF}})$, normalized to its value that would be obtained for an angular frequency $\omega_{\mathrm{RF}} = 0$ for a source and a termination impedance that are both perfectly matched to the modulator's characteristic transmission-line impedance $\underline{Z}_0$ ([90], Eq. 3). This leads to

$$\underline{m}_{\mathrm{PH}}(\omega_{\mathrm{RF}}) = \frac{\underline{\hat{\varphi}}(\omega_{\mathrm{RF}})}{\underline{\hat{\varphi}}(0)\big|_{\underline{Z}_{\mathrm{src}}=\underline{Z}_{\mathrm{trm}}=\underline{Z}_0}} = \underline{A}\,\underline{H}_{\mathrm{RC}}\left(\frac{\mathrm{e}^{\underline{q}^{-}\ell}-1}{\underline{q}^{-}} + \underline{B}\frac{\mathrm{e}^{\underline{q}^{+}\ell}-1}{\underline{q}^{+}}\right), \tag{3.6}$$

where

$$\underline{A} = \frac{2}{\ell}\frac{\underline{Z}_0}{\underline{Z}_0+\underline{Z}_{\mathrm{src}}}\frac{1}{1-\underline{\Gamma}_{\mathrm{src}}\underline{\Gamma}_{\mathrm{trm}}\exp(-2\underline{\gamma}\ell)}, \tag{3.7}$$

$$\underline{B} = \exp\left(-2\underline{\gamma}\ell\right)\underline{\Gamma}_{\mathrm{trm}}, \tag{3.8}$$

$$\underline{q}^{\pm} = \pm\underline{\gamma} + \mathrm{j}\frac{n_{\mathrm{g,opt}}\omega_{\mathrm{RF}}}{\mathrm{c}}, \tag{3.9}$$

and where the reflection factors of source and termination are given by,

$$\underline{\Gamma}_{\mathrm{src}} = \frac{\underline{Z}_{\mathrm{src}}-\underline{Z}_0}{\underline{Z}_{\mathrm{src}}+\underline{Z}_0} \quad \text{and} \quad \underline{\Gamma}_{\mathrm{trm}} = \frac{\underline{Z}_{\mathrm{trm}}-\underline{Z}_0}{\underline{Z}_{\mathrm{trm}}+\underline{Z}_0}. \tag{3.10}$$

The quantity $\underline{H}_{\mathrm{RC}}(\omega_{\mathrm{RF}})$ in Eq. 3.6 accounts for the fact that the voltage that becomes effective for modulation in the slot waveguide is reduced with respect to the voltage on the metal transmission lines through a voltage divider formed by the slab conductance and the slot capacitance [105]. This reduction becomes more pronounced as the frequency increases and can be written as

$$\underline{H}_{\mathrm{RC}}(\omega_{\mathrm{RF}}) = \frac{1}{1+\mathrm{j}\omega_{\mathrm{RF}}C'_{\mathrm{S}}/G'_{\mathrm{S}}}. \tag{3.11}$$

The frequency response of EO modulators is usually obtained from a frequency-dependent decay of an intensity modulation rather than from a phase modulation. To connect the two quantities, we consider an MZM in push-pull configuration, for which the phase shifts φ_1 and φ_2 in the two arms fulfill the relation $\varphi_1 = -\varphi_2 = \varphi$. The phase difference between the two arms $\Delta\varphi$ is then given by $\Delta\varphi = 2\varphi_1$, and the intensity I_{opt} of the optical output signal is related to the phase difference $\Delta\varphi$ by

$$I_{\text{opt}} = \cos^2(\Delta\varphi/2) = \cos^2(\varphi_1)\,. \tag{3.12}$$

If the push-pull MZM is biased at the 3 dB point (quadrature point) and operated under small-signal conditions, i.e., with $\Delta\varphi = \pi/2 \pm \delta\varphi$, $(|\delta\varphi| \ll \pi/2)$, Eq. 3.12 can be linearized and the change in optical power δP_{opt} is in proportion to $\delta\varphi$. In characterization experiments, the optical output of the modulator is usually coupled to a photodetector, the photocurrent I_{p} of which is proportional to the received optical power such that

$$\delta I_{\text{p}} \propto \delta P_{\text{opt}} \propto \delta\varphi. \tag{3.13}$$

The small-signal intensity frequency response $\underline{m}_{\text{EOE}}$ of the EOE conversion is therefore identical to the phase modulator frequency response given in Eq. 3.6,

$$\underline{m}_{\text{EOE}}(\omega_{\text{RF}}) = \underline{m}_{\text{PH}}(\omega_{\text{RF}}). \tag{3.14}$$

To quantify the bandwidth of the modulator, the 3 dB corner frequency $f_{3\text{dB,EOE}} = \omega_{3\text{dB,EOE}}/2\pi$ of the intensity modulation may be used. The 3 dB corner frequency $\omega_{3\text{dB,EOE}}/2\pi$ is defined as the frequency $\omega_{\text{RF}}/2\pi$, for which $|\underline{m}_{\text{EOE}}(\omega_{\text{RF}})|^2$ is reduced by a factor of two compared to $|\underline{m}_{\text{EOE}}(0)|^2$, which corresponds to a power decay of the associated spectral component of the photocurrent by a factor of two. Alternatively, also the 6 dB corner frequency $f_{6\text{dB,EOE}} = \omega_{6\text{dB,EOE}}/2\pi$ of $|\underline{m}_{\text{EOE}}(\omega_{\text{RF}})|^2$ can be considered, which corresponds to a decay of $|\underline{m}_{\text{EOE}}(\omega_{\text{RF}})|^2$ and of the associated photocurrent power by a factor of four and is hence equivalent to a reduction of the photocurrent amplitude or, equivalently, the phase modulation amplitude by a factor of two. Both values are used in the literature to refer to the bandwidth of a modulator [64, 65, 113], sometimes without explicitly stating which of the two values is specified. In the following, we either specify both values or reside to the 6 dB corner frequency for better comparability to similar investigations of SiP EO modulators [50, 65, 91, 105].

To apply the model developed here to a given device design, the complex propagation parameter $\underline{\gamma}$ and the characteristic impedance $\underline{Z}_0$ can be directly determined from S-parameter measurements or with numerical mode solvers. The equivalent-circuit parameters R'_{TL}, L'_{TL},C'_{TL} ,G'_{S}, C'_{S} can then be obtained by fitting Eq. 3.4 and Eq. 3.5 to the frequency-dependence of $\underline{\gamma}$ and $\underline{Z}_0$, see Section 3.3. If, in addition, $n_{\mathrm{g,opt}}$ is known, Eq.3.6 allows to predict the EO response of the modulator.

3.3 Electrical characterization and fitting procedure

To experimentally verify the model introduced in Section 3.2, we determine the frequency-dependent characteristic impedance $\underline{Z}_0$ and propagation parameter $\underline{\gamma}$ of a typical SOH modulator. These parameters fully describe the electrical behavior of the device and build the base for determining the frequency response $|\mathrm{m}_{\mathrm{EOE}}(\omega_{\mathrm{RF}})|$ of the EOE conversion, see Section 3.4. To ensure comparability with the measurement of the EOE device characteristics, we used a modulator with the organic EO material already applied to the slot waveguides by means of a dispensing technique. Direct-current measurements confirm that the organic material behaves as a dielectric with negligible parasitic currents flowing through the slot. For the devices used here, the thickness of the BOX layer was 3 µm, the device layer thickness was 220 nm, and the slot width was 120 nm. To de-embed the characteristics of the device under test (DUT) from those of the RF contact-pad parasitics, we investigate two MZMs with nominally identical cross sections and different active lengths $\ell_1 = 500\,\mu\mathrm{m}$ and $\ell_2 = 750\,\mu\mathrm{m}$ of the phase shifters. In a first step, we measure S-parameters of the embedded devices using a VNA and microwave contact probes. Figure 3.3(c) shows the measured (embedded) transmission $\underline{S}_{21}$ and reflection $\underline{S}_{11}$ of the two modulators for a gate voltage $U_{\mathrm{gate}} = 0\,\mathrm{V}$. The reference plane was moved to the tip of the probes using a short-open-load-through (SOLT) calibration routine with an impedance-standard substrate. The phase-shifter sections of both devices are thus only embedded into identical on-chip contact circuits that are formed by the contact pads and subsequent transitions on both ends of the modulator, see Fig. 3.3(a), and that are referred to as contact fixtures in the following. Each of these fixtures is modeled by a series impedance $\underline{Z}$ and a shunt admittance $\underline{Y}$ as shown in Fig. 3.3(b), which can be represented by electrical transfer matrices (T-matrices [87]) $\underline{T}_{\mathrm{L}}$ and $\underline{T}_{\mathrm{R}}$ for the left and the right fixture, respectively, see Section 3.7, Eq. 3.22 and Eq. 3.23. These T-matrices can be calculated from the measured S-parameters $\underline{S}_{21}$ and $\underline{S}_{11}$ using standard microwave theory, see Section 3.7. To de-embed the T-matrices $\underline{T}_{\mathrm{DUT1}}$ and $\underline{T}_{\mathrm{DUT2}}$ of the phase shifters with lengths ℓ_1 and ℓ_2, we first extract the measured T-matrix of the embedded modulator $\underline{T}_{\mathrm{m1}} = \underline{T}_{\mathrm{L}}\underline{T}_{\mathrm{DUT1}}\underline{T}_{\mathrm{R}}$ and $\underline{T}_{\mathrm{m2}} = \underline{T}_{\mathrm{L}}\underline{T}_{\mathrm{DUT2}}\underline{T}_{\mathrm{R}}$ from the measured S-parameters. Introducing the T-matrix $\underline{T}_{\mathrm{DUT0}}$ of an $\ell_0 = 250\,\mu\mathrm{m}$-long de-embedded modulator section and exploiting that $\ell_1 = 2\ell_0$ and $\ell_2 = 3\ell_0$ we can rewrite $\underline{T}_{\mathrm{DUT1}}$ and $\underline{T}_{\mathrm{DUT2}}$ as $\underline{T}_{\mathrm{DUT1}} = \underline{T}_{\mathrm{DUT0}}\underline{T}_{\mathrm{DUT0}}$ and $\underline{T}_{\mathrm{DUT2}} = \underline{T}_{\mathrm{DUT0}}\underline{T}_{\mathrm{DUT0}}\underline{T}_{\mathrm{DUT0}}$. The T-matrix of the virtual through connection shown in Fig.3.3(b) is defined as $\underline{T}_{\mathrm{thru}} = \underline{T}_{\mathrm{L}}\underline{T}_{\mathrm{R}}$ and can then be calculated from the measured matrices as $\underline{T}_{\mathrm{thru}} = \underline{T}_{\mathrm{m1}}\underline{T}_{\mathrm{m2}}^{-1}\underline{T}_{\mathrm{m1}}\underline{T}_{\mathrm{m2}}^{-1}\underline{T}_{\mathrm{m1}}$. This allows to determine $\underline{T}_{\mathrm{L}}$ and $\underline{T}_{\mathrm{R}}$ directly from the measured transfer matrices $\underline{T}_{\mathrm{m1}}$ and $\underline{T}_{\mathrm{m2}}$ and to de-embed the modulator response by calculating $\underline{T}_{\mathrm{DUT1}} = \underline{T}_{\mathrm{L}}^{-1}\underline{T}_{\mathrm{m1}}\underline{T}_{\mathrm{R}}^{-1}$ and $\underline{T}_{\mathrm{DUT2}} = \underline{T}_{\mathrm{L}}^{-1}\underline{T}_{\mathrm{m2}}\underline{T}_{\mathrm{R}}^{-1}$. Using Eq. 3.25 of Section 3.7, we can then extract the frequency-dependent characteristic impedance $\underline{Z}_0$ and the frequency-dependent propagation parameter $\underline{\gamma}$ from the transfer matrices $\underline{T}_{\mathrm{DUT1}}$ and $\underline{T}_{\mathrm{DUT2}}$ of the de-embedded modulator, see black traces in Figures 3.3(d-g). We find that the results obtained from $\underline{T}_{\mathrm{DUT1}}$ and $\underline{T}_{\mathrm{DUT2}}$ show very good agreement, thereby confirming the validity of our de-embedding approach. For comparison, we also extract $\underline{Z}_0$ and $\underline{\gamma}$ by applying Eq. 3.24 and Eq. 3.25 directly to the measured T-matrices $\underline{T}_{\mathrm{m1}}$ and $\underline{T}_{\mathrm{m2}}$ of the embedded modulators, thereby ignoring the impact of the contact fixtures. The resulting frequency characteristics of $\underline{Z}_0$ and $\underline{\gamma}$ are depicted as blue and red traces in Figures 3.3(d-g) and show clear differences, thereby underlining the importance of proper de-embedding.

Our results indicated that $\underline{Z}_0$ has a negligible imaginary part and amounts to approximately $50\,\Omega$ – except for the low-frequency region, where $\underline{Z}_0$ deviates from its ideal low-loss and high-frequency approximation, see Eq. 3.26 in Section 3.8. This ensures good impedance matching to typical feeding networks and drivers. The real part α of $\underline{\gamma}$, associated with RF propagation loss, increases with frequency due to loss in the metal stripes and in the resistive slabs, see the following paragraphs for a detailed discussion of the loss mechanisms. The imaginary part β of $\underline{\gamma}$ shows a linear increase indicating a low dispersion of the RF transmission line.

The measurement of S-parameters and subsequent de-embedding and extraction of $\underline{\gamma}$ and $\underline{Z}_0$ was repeated for a range of gate voltages U_{gate} between 0 V and 300 V. Figure 3.4 shows the numerical values obtained from measurements in blue. To determine the six equivalent-circuit parameters R'_{TL}, L'_{TL}, C'_{TL}, $G'_{\mathrm{S,bulk}}$, $G'_{\mathrm{S,acc}}$, and C'_{S}, the following approach was used: First, Eq. 3.4

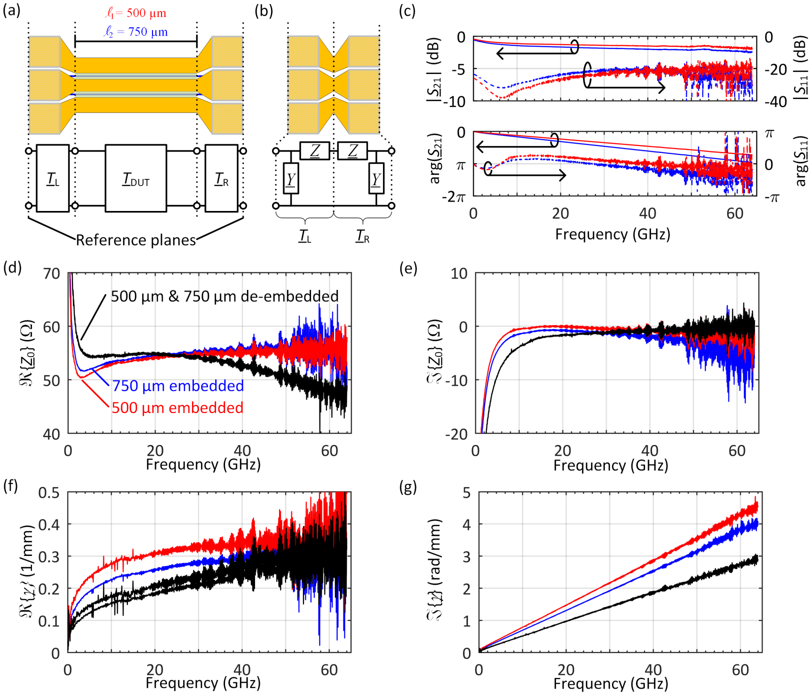

Fig. 3.3: (a) Simplified electrical structure of the SOH modulators. The phase-shifter sections with lengths ℓ_1 or ℓ_2 and T-matrices $\underline{T}_{\mathrm{DUT1}}$ or $\underline{T}_{\mathrm{DUT2}}$ are electrically embedded into contact fixtures, modeled by T-matrices T_{L} and T_{R}. (b) The contact fixtures are modeled by a series impedance $\underline{Z}$ and a shunt admittance $\underline{Y}$. (c) Amplitude and phase of measured S-parameters for embedded MZMs with lengths $\ell_1 = 500\,\mu\mathrm{m}$ (red) and $\ell_2 = 750\,\mu\mathrm{m}$ (blue). (d) Real part and (e) imaginary part of the characteristic impedance $\underline{Z}_0$, along with (f) real part and (g) imaginary part of the propagation constant γ. Black curves indicate values as extracted from de-embedded modulators of lengths ℓ_1 and ℓ_2. These results show good agreement and hence confirm the validity of our de-embedding approach. In contrast to that, the red and blue curves correspond to values extracted from the embedded modulators by ignoring the impact of the contact fixtures. Consequently, the results obtained for the different device lengths are not in agreement.

Table 3.1: Circuit parameters obtained by fitting Eq. 3.4 and 3.5 to the measured frequency-dependent and gate-voltage-dependent values of $\underline{\gamma}$ and $\underline{Z}_0$, see Fig. 3.4.

	Fit
R'_{TL}	$13\,\Omega/\mathrm{mm}$
L'_{TL}	$414\,\mathrm{pH/mm}$
C'_{TL}	$130\,\mathrm{fF/mm}$
$G'_{\mathrm{S,bulk}}$	$2.76\,\mathrm{mS/mm}$
$g'_{\mathrm{S,acc}} = G'_{\mathrm{S,acc}}/U_{\mathrm{gate}}$	$145\,\mu\mathrm{S/(Vmm)}$
C'_{S}	$160\,\mathrm{fF/mm}$

and Eq. 3.5 were used to calculate $R'_{\mathrm{TL}} = \Re\left\{\underline{Z}_0\underline{\gamma}\right\}$ and $L'_{\mathrm{TL}} = \Im\left\{\underline{Z}_0\underline{\gamma}\right\}/\omega_{\mathrm{RF}}$ directly from $\underline{\gamma}$ and $\underline{Z}_0$. Using the fact that both R'_{TL} and L'_{TL} are independent of frequency and of the applied gate voltage, the two values were calculated for all frequencies and gate voltages and then averaged. In a second step, a multi-dimensional multi-parameter least-squares fit was used to obtain C'_{TL}, $G'_{\mathrm{S,bulk}}$, $G'_{\mathrm{S,acc}}$, and C'_{S} by fitting Eq. 3.4 and Eq. 3.5 to the measured frequency-dependent and gate-voltage-dependent values of $\underline{\gamma}$ and $\underline{Z}_0$, see Table 3.1 for the resulting numerical values. We estimate, e.g., a differential capacitance of the transmission line of 130 fF/mm, which compares well to the numerical result of 151 fF/mm obtained for a similar device geometry in [91]. The fitted curves are shown in red in Fig. 3.4 and show good agreement with the measured data. For increasing frequencies, the characteristic impedance quickly approaches its ideal high-frequency real value $\underline{Z}_0 = \sqrt{L'_{\mathrm{TL}}/(C'_{\mathrm{S}} + C'_{\mathrm{TL}})} \approx 50\,\Omega$, which can be obtained from Eq. 3.5 using $R'_{\mathrm{TL}} \ll \omega_{\mathrm{RF}} L'_{\mathrm{TL}}$ and $\overline{G}'_{\mathrm{S}} \ll \omega_{\mathrm{RF}}(\overline{C}'_{\mathrm{S}} + C'_{\mathrm{TL}})$. The characteristic impedance $\underline{Z}_0$ as well as the imaginary part of $\underline{\gamma}$ are rather insensitive to the gate voltage.

In contrast to this, the losses show a strong dependence on the conductivity of the slabs and thus on U_{gate}. To explain this finding, we first consider the losses in the metal transmission line represented by R'_{TL}, L'_{TL} and C'_{TL} separately from the losses in the RC element which represents the slab and the slot and which is formed by $G'_{\mathrm{S,bulk}}$, $G'_{\mathrm{S,acc}}$ and C'_{S}. The different loss contributions are plotted as a function of frequency in Fig. 3.5 for three different gate voltages. Note that the separation and the independent analysis of the two loss contributions

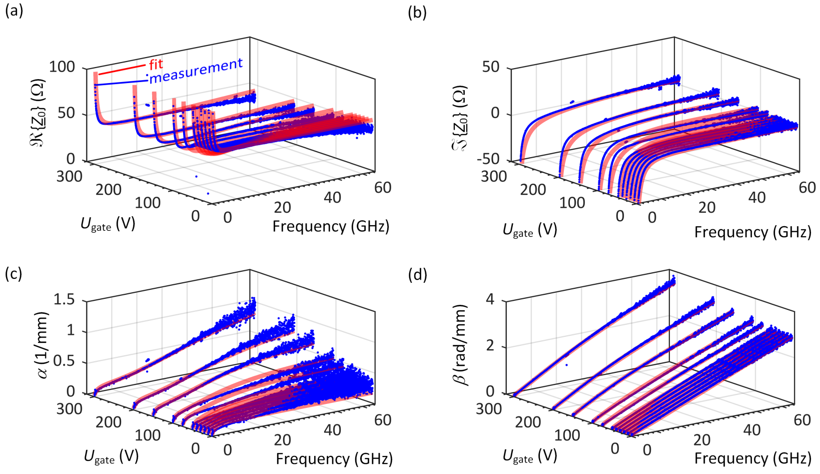

Fig. 3.4: Measured values (blue) and fitted curves (red) according to Eq. 3.4 and Eq. 3.5 as a function of both RF frequency and gate voltage U_gate for (a) the real part of the characteristic impedance $\underline{Z}_0$, (b) the imaginary part of the characteristic impedance $\underline{Z}_0$, (c) the real part of the complex propagation parameter $\underline{\gamma}$ associated with loss, and (d) the imaginary part of the complex propagation parameter $\underline{\gamma}$.

represents an approximation and might thus lead to small deviations from the mathematically correct overall loss that can be obtained from the real part α of the complex propagation parameter $\underline{\gamma}$ according to Eq. 3.4.

For the contribution of the bare transmission line, we neglect $G'_\text{S,bulk}$, $G'_\text{S,acc}$ and G'_S in Eq. 3.4, such that the loss can be written as

$$\alpha_\text{TL} = \Re\left\{\sqrt{\left(R'_\text{TL} + \text{j}\omega_\text{RF} L'_\text{TL}\right) \text{j}\omega_\text{RF} C'_\text{TL}}\right\}. \tag{3.15}$$

For low frequencies, $\omega_\text{RF} \ll \omega_\text{TL}$, $\omega_\text{TL} = R'_\text{TL}/L'_\text{TL}$, the loss α_TL increases in proportion to $\sqrt{\omega_\text{RF}}$,

$$\alpha_\text{TL} \approx \sqrt{\frac{R'_\text{TL} C'_\text{TL}}{2}} \sqrt{\omega_\text{RF}} \quad \text{for} \quad \omega_\text{RF} \ll \omega_\text{TL}. \tag{3.16}$$

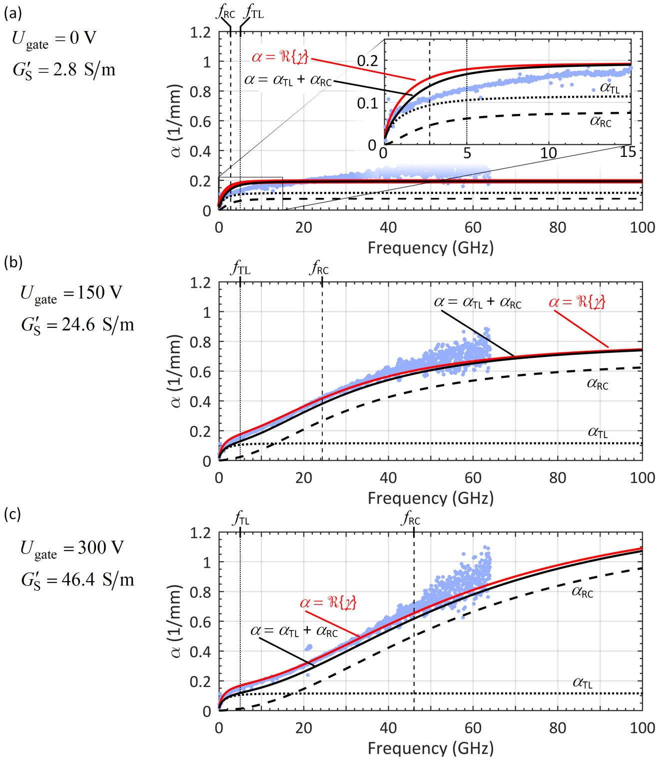

Fig. 3.5: Detailed representation of RF loss mechanisms in the slot-waveguide modulator. Blue data points represent measured data, and red traces correspond to the loss obtained by calculating the real part of the complex propagation parameter $\underline{\gamma}$, Eq. 3.4, for the circuit parameters obtained by the fit. The three panels correspond to three values of the gate voltage U_{gate} and represent slices of the 3D plot in Fig. 3.4. Besides the gate voltage U_{gate}, the associated slab conductance G'_S is specified. The black dotted traces depict the loss contribution α_{TL} of the transmission line formed by the metal electrodes only, see Eq. 3.15, and the black dashed traces show the loss contribution α_{RC} of the RC element formed by the slab and the slot, see Eq. 3.18. The solid black line shows the sum of α_{TL} and α_{RC}, which is in good agreement with the loss obtained from the full model represented by the red solid trace. (a) $U_{\text{gate}} = 0$ V: Except for very low frequencies, see inset, the loss is constant with frequency. (b) $U_{\text{gate}} = 150$ V: The quadratic frequency-dependence of α_{RC} for frequencies below the corner frequency $f_{RC} = \omega_{RC}/(2\pi)$ of the RC element, see Eq. 3.19, leads to a strong increase of the total loss with frequency. At frequencies $f_{RF} = \omega_{RF}/(2\pi) \gg f_{RC}$ the total loss approaches a constant value, see Eq. 3.17 and Eq. 3.20. (c) $U_{\text{gate}} = 300$ V: The corner frequency f_{RC} is further increased compared to (b), and the total loss no longer reaches its constant high-frequency value in the considered frequency range.

For higher frequencies, $\omega_{\mathrm{RF}} \gg \omega_{\mathrm{TL}}$, the loss α_{TL} of the bare transmission line approaches its low-loss, high-frequency approximation [87] and is constant with frequency,

$$\alpha_{\mathrm{TL}} \approx \sqrt{C'_{\mathrm{TL}}/L'_{\mathrm{TL}}}\left(R'_{\mathrm{TL}}/2\right) \qquad \text{for} \qquad \omega_{\mathrm{RF}} \gg \omega_{\mathrm{TL}}. \tag{3.17}$$

The frequency dependence of α_{TL} according to Eq. 3.15 is illustrated in Fig. 3.5 by the dotted black lines.

For the loss contribution of the RC-element that is formed by the slot capacitance C'_{S} and the slab conductance $G'_{\mathrm{S}} = G'_{\mathrm{S,acc}} + G'_{\mathrm{S,bulk}}$, we derive a relationship in Section 3.9,

$$\alpha_{\mathrm{RC}} = \frac{\omega_{\mathrm{RF}}^2 C_{\mathrm{S}}'^2 G_{\mathrm{S}}^{-1}}{1 + (\omega_{\mathrm{RF}} C'_{\mathrm{S}} G_{\mathrm{S}}'^{-1})^2} \frac{1}{2\Re\left\{\underline{Z}_0^{-1}\right\}}. \tag{3.18}$$

For frequencies well below the RC corner frequency $\omega_{\mathrm{RC}} = G'_{\mathrm{S}}/C'_{\mathrm{S}}$ of the RC element, we can approximate Eq. 3.18 by

$$\alpha_{\mathrm{RC}} \approx \omega_{\mathrm{RF}}^2 \frac{C_{\mathrm{S}}'^2}{G'_{\mathrm{S}}} \frac{1}{2\Re\left\{\underline{Z}_0^{-1}\right\}} \qquad \text{for} \qquad \omega_{\mathrm{RF}} \ll \omega_{\mathrm{RC}}, \tag{3.19}$$

leading to a quadratic increase of the losses with frequency. For frequencies well above the RC corner frequency ω_{RC}, we obtain

$$\alpha_{\mathrm{RC}} \approx G'_{\mathrm{S}} \frac{1}{2\Re\left\{\underline{Z}_0^{-1}\right\}} \qquad \text{for} \qquad \omega_{\mathrm{RF}} \gg \omega_{\mathrm{RC}}, \tag{3.20}$$

i.e., the losses are independent of frequency. The frequency dependence of α_{RC} according to Eq. 3.18 is illustrated in Fig. 3.5 by the dashed black lines. The overall loss α can be estimated by adding α_{TL} and α_{RC}, leading to the solid black lines in Fig. 3.5. These estimated losses are in good agreement with the loss obtained from directly using $\alpha = \Re\left\{\underline{\gamma}\right\}$ according to Eq. 3.4, see red lines in Fig. 3.5.

The three panels for Fig. 3.5(a, b, c) correspond to different gate voltages of 0 V, 150 V, and 300 V, respectively. For the samples used in our experiments, the doping of the slabs is rather low, and hence the resistance $G_{\mathrm{S}}^{\prime -1}$ of the slabs is rather high in case no gate voltage is applied. This leads to a small corner frequency ω_{RC}, illustrated by a dashed vertical line in Fig. 3.5(a), and the loss contribution α_{RC} of the RC-element quickly reaches the frequency-independent value given by Eq. 3.20. For low frequencies, the total loss is dominated by the contribution α_{TL} of the bare transmission line, Eq. 3.16, and increases in proportion to $\sqrt{\omega_{\mathrm{RF}}}$. Small discrepancies between measured and predicted curves can be observed for small values of U_{gate} and for the frequency range beyond 40 GHz, where the measurement data become noisy. These discrepancies may be reduced by introducing additional free parameters into the model, thereby improving the fit to measured data, but sacrificing the clear correlation between model parameters and physical device parameters such as geometry and material properties, see Section 3.4 for a more detailed discussion. If U_{gate} is increased, Fig. 3.5(b) and 3.5(c), ω_{RC} becomes larger and exceeds ω_{TL}, which leads to a strongly frequency-dependent increase of the overall loss dominated by $\alpha_{\mathrm{RC}} \propto \omega_{\mathrm{RF}}^2$ for frequencies ω_{RF} between ω_{TL} and ω_{RC}. At even higher frequencies ($\omega_{\mathrm{RF}} \gg \omega_{\mathrm{RC}}$), the total losses are again frequency-independent, see Eq. 3.17 and Eq. 3.20. For a gate voltage of 300 V, Fig. 3.5(c), the plateau, where the overall loss becomes frequency-independent, is no longer reached in the considered range of RF frequencies. For the discussion of design trade-offs (Section 3.5) it is important to note that in the range between 5 and 50 GHz, increasing the slab conductivity, in the range considered here by changing U_{gate}, brings the modulator from a regime with weakly frequency-dependent loss to a regime with strongly frequency-dependent loss and may hence limit the bandwidth of the device.

3.4 Measured and modeled electro-optic response

With the knowledge of the six equivalent-circuit parameters R'_{TL}, L'_{TL}, C'_{TL}, $G'_{\mathrm{S,bulk}}$, $G'_{\mathrm{S,acc}}$, C'_{S} and of the optical group velocity $v_{\mathrm{g,opt}}$ in the slot waveguide, Eq. 3.4-3.11 can be used to predict the EO frequency response of the SOH modulator. In the following we assume an operating wavelength of 1.55 µm. Note that SOH modulators can be adapted to other wavelengths such as 1300 nm, where the electro-optic coefficient of the underlying materials should be even higher [114]. The optical group velocity $v_{\mathrm{g,opt}} = c/n_{\mathrm{g,opt}}$ at

1.55 µm is obtained by calculating the group refractive index $n_{\mathrm{g,opt}} = 3.2$ by means of a numerical mode solver. In Fig. 3.6(a), the red lines show the EO frequency response as predicted by the model for a 750 µm-long modulator terminated with a 50 Ω impedance under the influence of gate voltages between 0V̇ to 300 V. These predictions are based on the circuit parameters listed in Table 3.1, as obtained from the purely electrical measurements of the frequency-dependent RF scattering parameters $\underline{S}_{21}$ and $\underline{S}_{11}$. Increasing the gate voltage increases the bandwidth, which is mainly due to a reduction of the RC time-constant of the slab-loaded slot waveguides. The predicted frequency response is compared against measured values obtained by using a VNA and a calibrated optical receiver [115], see blue traces in Fig. 3.6(a). In these measurements, the swept-source microwave stimulus of the VNA is applied to the modulator via microwave probes. The modulator is biased at its 3 dB point and the microwave signals amplitude is chosen small enough for the modulator to be operated under small-signal condition. The optical signal at a center wavelength of 1.55 µm is subsequently amplified using an EDFA, filtered by a band-pass filter to remove out-of-band amplified spontaneous emission (ASE), and converted back to the electrical domain using a photodiode that is connected to the receiver port of the VNA. The frequency-dependent decay of the EOE frequency response $|m_{\mathrm{EOE}}(\omega_{\mathrm{RF}})|$ according to Eq. 3.14 and Eq. 3.6 can be derived from the VNA measurement by the relation

$$10\log\left(|m_{\mathrm{EOE}}(\omega_{\mathrm{RF}})|^2\right) = S_{21,\mathrm{VNA,dB}}(\omega_{\mathrm{RF}}) - S_{21,\mathrm{VNA,dB}}(\omega_{\mathrm{RF},0}). \tag{3.21}$$

In this relation, $S_{21,\mathrm{VNA,dB}}$ denotes the scattering parameter measured by the VNA in dB after de-embedding from the frequency response of the photodiode and of the microwave probe, and $\omega_{\mathrm{RF},0}$ is a small reference frequency that is chosen as small as allowed by the VNA.

The different shades of blue in Fig. 3.6(a) indicate three independent measurements of the same device with small statistical variations. Overall, we find a good agreement of the measurements with the model predictions (red). In Fig. 3.6(b), both the 3 dB and the 6 dB EOE bandwidths of the modulator are shown for different gate voltages. For the 6 dB EOE bandwidth $f_{6\mathrm{dB,EOE}}$, blue diamonds correspond to the measured values, and the dotted red line represents the bandwidths predicted by the model. Similarly, blue circles and the solid red line indicated measurements and model predictions of the 3 dB EOE bandwidth $f_{3\mathrm{dB,EOE}}$. The good agreement of the predicted bandwidths with their

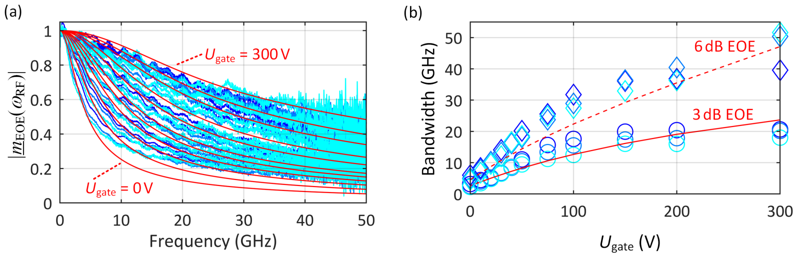

Fig. 3.6: Electro-optic-electric (EOE) frequency response $|\underline{m}_{\mathrm{EOE}}(\omega_{\mathrm{RF}})|$ according to Eq. 3.6 and Eq. 3.14 of a 750 µm-long SOH modulator terminated with a 50 Ω impedance. (a) EOE response for different gate voltages U_{gate} of 300 V, 200 V, 150 V, 100 V, 75 V, 50 V, 40 V, 30 V, 20 V, 10 V, and 0 V (from top to bottom). The red curve represents the prediction of the model according to Eq. 3.4 to Eq. 3.11, and the blue line corresponds to the measurement results, where the different shades indicate three independent measurements of the same device. With increasing gate voltage, the frequency response flattens. (b) 3dB EOE bandwidth $f_{3\mathrm{dB,EOE}}$ (red solid line: model; blue circles: measurement) and 6 dB EOE bandwidth $f_{6\mathrm{dB,EOE}}$ (red broken line: model; blue diamonds: measurement) as extracted from the curves in (a) as a function of applied gate voltage U_{gate}. The predicted bandwidths agree well with their measured counterparts, thus confirming that the proposed method allows to accurately predict the bandwidth of an SOH modulator based on the knowledge of purely electrical characteristics.

measured counterparts validates the model introduced in Section 3.2, i.e., the proposed method allows to accurately predict the EOE frequency response of an SOH modulator based on the knowledge of purely electrical characteristics along with the group velocity $v_{\mathrm{g,opt}}$ of the optical signal in the slot waveguide. Again, some discrepancies between measured and predicted curves can be observed for small values of U_{gate}. We believe that our model can be further refined by considering additional effects and/or by including additional equivalent-circuit elements, thereby reducing the discrepancies to the measured data. As an example, we assume a simple linear relationship between the differential conductance $G'_{\mathrm{S,acc}} = g'_{\mathrm{S,acc}} U_{\mathrm{gate}}$ and the gate voltage U_{gate} without any threshold behavior. This is to be expected for an ideal accumulation layer of majority carriers in the slab, but the physical situation in the device might be more complex. The benefit of our fairly simple model is the clear correlation between model parameters and physical device parameters such as geometry and material properties. This correlation is essential for deriving guidelines for future device designs. The electrical characteristics are easily accessible by either measurements in the RF domain, by simulations of the electrical RF device characteristics, or by estimating the distributed-element parameters from the modulator geometry and material properties. We believe that high-throughput wafer-level testing protocols might greatly benefit from a quantitatively verified model-based prediction of the EOE frequency response based on easily accessible electrical scattering parameters.

3.5 Design guidelines

3.5.1 Overcoming bandwidth limitations

Having validated the model of the SOH modulator, various design parameters can be tested for their impact on device performance. In the following, we assume a device with transmission line parameters R'_{TL}, L'_{TL} , and C'_{TL} as specified in Table 3.1 and investigate the impact of variations of the slot capacitance C'_{S} and of the slab conductance G'_{S} on the EO bandwidth. This leads to the following considerations:

- The slab conductance G'_{S} can be adjusted by modifying the doping profile in the slab. Increased slab conductivity will affect the electrical behavior and thus opens a way to increase the modulators bandwidth as discussed in detail below. As a trade-off, when increasing the slab conductivity by an increased doping concentration, the higher concentration of free carriers will also increase optical losses due to FCA.
- The slot capacitance C'_{S} is mainly affected by the geometry of the slot waveguide and can be reduced by increasing the slot width. Reduced slot capacitance will affect the electrical behavior and thus the bandwidth as discussed in detail below. As a trade-off, increasing the slot width reduces the modulating electric RF field in the slot as well as the confinement factor of the optical field in the slot region. This can lead to a reduced modulation efficiency [91, 116]. However, the poling efficiency may also be impaired by too narrow slot widths [48]. As an example, previous investigations of SOH modulators based on the EO material JRD1 [18] have shown that increasing the slot width to, e.g., 200 nm does not decrease the modulation efficiency of these devices.

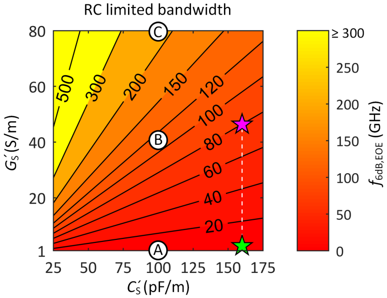

Fig. 3.7: 6 dB EOE bandwidth $f_{6\text{dB,EOE}}$ of a modulator only limited by the RC low-pass formed by the slot capacitance C_S' and the slab conductance G_S'. Both a reduction of C_S' and an increase of G_S' linearly increases the bandwidth. The parameters of the devices used in this paper for experimental verification of the model, see Table 3.1, are indicated by a green star for the case of a gate voltage of 0 V and by a magenta star for a gate voltage of 300 V. For the parameters indicated by Ⓐ, Ⓑ and Ⓒ the frequency response of a 750 µm-long modulator is exemplarily shown in Fig. 3.9.

The frequency response expressed by Eq. 3.6 considers all bandwidth-limiting effects, namely RC limitations of the slot waveguide together with the slabs, RF loss, impedance mismatch, and velocity mismatch. To investigate the impact of RC limitations, we first consider a theoretical modulator only limited by the RC-low-pass formed by the slab resistance and the slot capacitance, explicitly neglecting impedance mismatch, velocity mismatch and RF loss. The response of such a device is given by $\underline{H}_{\text{RC}}(\omega_{\text{RF}})$, Eq. 3.11. Figure 3.7 shows the 6 dB EOE bandwidth $f_{6\text{dB,EOE}}$ for a device that is only limited by the RC-low-pass as a function of slab conductance G_S' and slot capacitance C_S'. The parameters of the devices used for experimental verification in this paper, see Table 3.1, are indicated by a green star for the case of 0 V gate voltage applied and by a magenta star for 300 V gate voltage applied. The bandwidth increases linearly with both G_S' and $1/C_S'$. Note that the RC limitation is independent of the device length. Using the current devices as a reference, an increase of G_S', e.g., by a factor of 20, possibly combined with a slight reduction of C_S' by, e.g., 40%, would permit RC-related EOE bandwidths $f_{6\text{dB,EOE}}$ in excess of 100 GHz if the device was only RC-limited. Increasing G_S' by a factor of 20 can be realistically achieved without introducing excessive optical loss by using optimized doping profiles, see Section 3.5.2 for details.

Next, we consider the impact of RF loss, impedance mismatch, and velocity mismatch on the modulator bandwidth. Figure 3.8(a) shows $f_{6\mathrm{dB,EOE}}$ of a 750 µm-long modulator limited only by RF loss, impedance mismatch, and velocity mismatch, explicitly neglecting RC limitations. The response of such a theoretical device is given by Eq. 3.6 for $\underline{H}_{\mathrm{RC}}(\omega_{\mathrm{RF}}) = \mathrm{const}$. For all slot capacitances C'_{S}, an increase in the slab conductance G'_{S} tends to reduce the bandwidth, see Fig. 3.8(a). This can be understood by considering that increasing the slab conductance G'_{S} initially brings the modulator from a regime with low and frequency-independent RF loss to a regime with high RF loss that increases with frequency, see Fig. 3.5. If the slab conductance G'_{S} is increased further, the RF loss and its frequency dependence are reduced again, and the impact on the bandwidth decreases. In practical devices, however, G'_{S} is constrained due to optical loss caused by FCA in the highly doped slab regions. This trade-off can be mitigated by optimized doping profiles, see Section 3.5.2.

We further investigate the overall RF loss α of the modulator, including both the loss in the metal electrodes and in the RC element formed by the slot waveguide and the slabs, as well as the associated real-part Z_0 of the characteristic impedance $\underline{Z}_0$ and the effective RF index $n_{\mathrm{eff,RF}}$. The numerical values for α, Z_0, and $n_{\mathrm{eff,RF}}$ are shown exemplarily for an RF frequency of 50 GHz in Fig. 3.8(b), Fig. 3.8(c), and Fig 3.8(d), respectively. While the RF loss, Fig. 3.8(b), initially increases substantially with the slab conductance G'_{S}, the characteristic impedance Z_0, Fig. 3.8(c), stays close to 50 Ω. For the effective microwave index $n_{\mathrm{eff,RF}}$, we observe a strong initial increase with the slab conductance G'_{S}, Fig. 3.8(d). This can be understood by considering that, for a low slab conductivity G'_{S}, the RC element is operated above its corner-frequency $\omega_{\mathrm{RC}} < 50\,\mathrm{GHz}$. In this regime, the slot capacitance C'_{S} is only partially charged during one cycle. If the slab conductance G'_{S} is increased, the slot capacitance C'_{S} becomes increasingly effective, and the RF wave is slowed down. For larger values of the slab conductance G'_{S}, the RC element is operated above its corner frequency and the capacitor is fully charged and de-charged during each cycle, leading to an RF index $n_{\mathrm{eff,RF}}$ that is essentially independent of the slab conductance. Following the same argument, it can also be understood why an increase of the slot capacitance C'_{S} therefore leads to an increase of $n_{\mathrm{eff,RF}}$.

To investigate the frequency dependence of the RF loss, of the characteristic impedance, of the effective RF index, and of the RC low-pass as well as

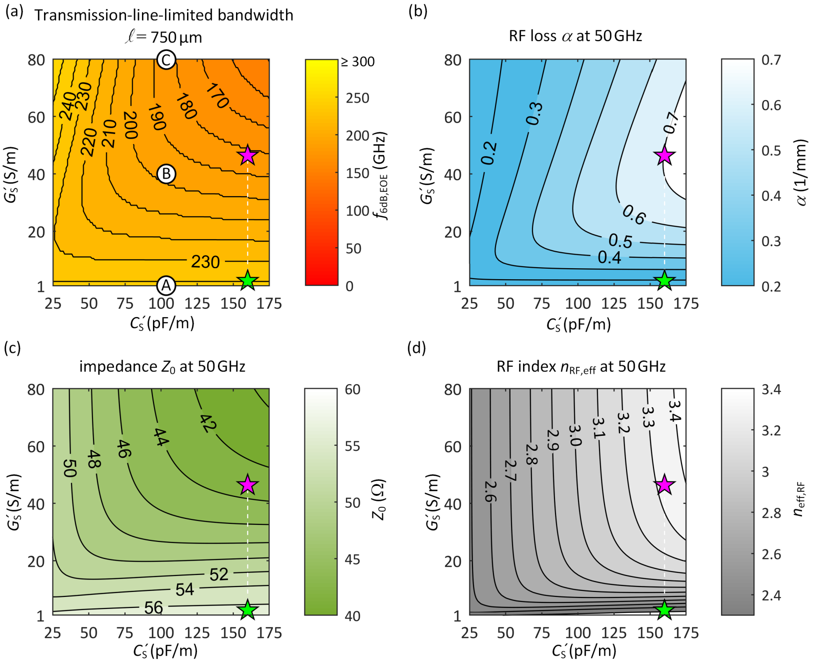

Fig. 3.8: (a) 6 dB EOE bandwidth $f_{6\text{dB,EOE}}$ of a 750 µm-long modulator limited only by RF loss, impedance mismatch, and velocity mismatch, explicitly neglecting the impact of the RC-low-pass formed by C'_S and G'_S. For a large C'_S and a low G'_S, an increase of G'_S leads to a strong frequency-dependent increase of the RF loss and thus to a reduced bandwidth. For the parameters indicated by Ⓐ, Ⓑ and Ⓒ the frequency response is exemplarily shown in Fig. 3.9. (b) RF loss for a 750 µm-long modulator at 50 GHz. The RF loss initially increases with increasing G'_S, see Fig. 3.5(a) and Fig. 3.5(b), but decreases again for very large values of G'_S, see Eq. 3.19. (c) Characteristic impedance Z_0 at 50 GHz. The impedance remains close to the system impedance of 50 Ω. (d) Effective RF refractive index $n_{\text{eff,RF}}$. For values of $G'_\text{S} \approx 50$ S/m and $C'_\text{S} \approx 130$ pF/m, $n_{\text{eff,RF}}$ is close to the effective optical group refractive index of 3.2. Increasing the slot capacitance slows down the RF wave and hence increases the RF refractive index. The detailed analysis in Fig. 3.9 shows that the bandwidth is not limited by velocity mismatch for practical values of C'_S for the considered length of the modulator. The parameters of the devices (see Table 3.1) used in this paper for experimental verification of the model are indicated by a green star for the case of 0 V gate voltage applied and by a magenta star for 300 V gate voltage applied.

the associated impact on the modulator bandwidth, we consider three exemplary C'_S-G'_S-value-pairs for a 750 µm-long device. The chosen value pairs are marked by Ⓐ, Ⓑ and Ⓒ in Fig. 3.7 and Fig. 3.8. The slot capacitance is fixed to $C'_\mathrm{S} = 100\,\mathrm{pF/m}$, while the slab conductance G'_S is increased from $G'_\mathrm{S} = 2.76\,\mathrm{S/m}$ (Ⓐ), which corresponds to the value extracted from the device used in our experiment, to $G'_\mathrm{S} = 40\,\mathrm{S/m}$ (Ⓑ) and further to $G'_\mathrm{S} = 80\,\mathrm{S/m}$ (Ⓒ). Figure 3.9(a) shows, for the weakly conducting slab with $G'_\mathrm{S} = 2.76\,\mathrm{S/m}$, the EOE frequency response $|m_\mathrm{EOE}(\omega_\mathrm{RF})|$, the RF loss α, the characteristic impedance Z_0, and the effective RF refractive index $n_\mathrm{eff,RF}$, all as a function of RF frequency up to 150 GHz. The solid red line depicts the total frequency response. Broken lines in blue, magenta, green, and black depict the frequency response by the sole contribution of the RC low-pass, the RF loss, the impedance mismatch, and the velocity mismatch, respectively. For a weakly conducting slab with $G'_\mathrm{S} = 2.76\,\mathrm{S/m}$, the total bandwidth (red line) is limited almost exclusively by the RC low-pass (blue broken line), whereas the impact of RF loss (red magenta broken line), impedance-mismatch (green broken line) and of velocity mismatch (black broken line) are negligible, because α, Z_0, and $n_\mathrm{eff,RF}$ show little frequency dependence. If the slab conductivity is increased to, e.g., 40 S/m, Fig. 3.9(b), or 80 S/m, Fig. 3.9(c), the RC corner frequency increases. However, frequency-dependent RF loss starts to become significant and limits the overall bandwidth of the device to values smaller than the RC corner frequency. For the increased slab conductance $G'_\mathrm{S} = 40\,\mathrm{S/m}$ and $G'_\mathrm{S} = 80\,\mathrm{S/m}$ impedance mismatch and velocity mismatch do not significantly affect the bandwidth either. This confirms that RF loss is the most important bandwidth-limiting effect besides the RC time constant of the slab-slot configuration.

Finally, we consider the 6 dB EOE bandwidth $f_\mathrm{6dB,EOE}$ obtained from the full model as a function of the slab conductance G'_S and the slot capacitance C'_S, taking into account all bandwidth-limiting effects, i.e., the RF loss, the impedance mismatch, the velocity mismatch and the RC low-pass. Figure 3.10 shows $f_\mathrm{6dB,EOE}$ as obtained by the full model for four different lengths ℓ of the modulator. For long devices, the frequency dependence of the RF loss is more significant, and increasing the slab conductivity G'_S has a smaller impact on the overall bandwidth than for short devices, see Fig. 3.10(a). Specifically, if ℓ is reduced to 500 µm, Fig. 3.10(c), and further to 200 µm, Fig. 3.10(d), the bandwidth approaches the RC-limited case shown in Fig. 3.7. A combination

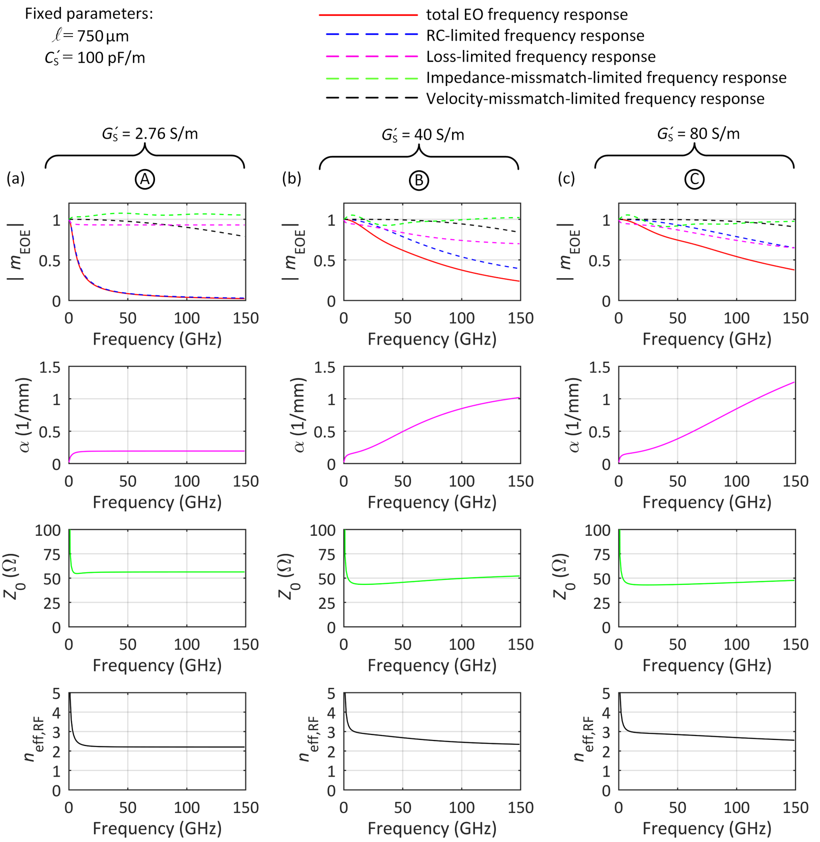

Fig. 3.9: Electro-optic bandwidth and RF properties for a 750 µm-long modulator with C'_S = 100 pF/m and (a) G'_S = 2.76 S/m, (b) G'_S = 40 S/m, and (c) G'_S = 80 S/m, corresponding to the points marked by Ⓐ, Ⓑ and Ⓒ, respectively, in Fig. 3.7, Fig. 3.8(a), and Fig. 3.8(b). The first row shows the overall frequency response $|m_\mathrm{EOE}(\omega_\mathrm{RF})|$ of the modulator (solid red line), as well as the frequency responses that correspond to the sole impact of RC limitations (blue dashed line), RF loss (magenta dashed line), impedance mismatch (green dashed line), and velocity mismatch (black dashed line). The second row shows the total RF loss α. In (a) the RF loss is low and frequency-independent, see Eq. 3.17. In (b) and (c) losses in the resistive slab are increased and the losses becomes strongly frequency-dependent, see Eq. 3.19, thereby reducing the bandwidth to values below the RC limit. The third row shows the characteristic impedance Z_0, which stays close to the system impedance of 50 Ω, except for low frequencies, where the Z_0 deviates from its ideal high frequency, low loss value, see Section 3.8. The last row shows the effective RF refractive index $n_\mathrm{eff,RF}$. In (a), the RC corner frequency ω_RC is small and the slot capacitance is not fully charged and de-charged as the RF wave (caption continued on next page)

Fig. 3.9 continued: propagates along the modulator. If the resistance of the slabs is reduced, see (b) and (c), ω_{RC} increases and the slot capacitance has a stronger impact on the RF wave, leading to a reduced velocity. The effective RF refractive index $n_{\mathrm{eff,RF}}$ then becomes close to the optical group index $n_{\mathrm{g,opt}} = 3.2$. Overall, impedance and velocity-mismatch are negligible for all of the three considered cases. In (a), the device is limited by the RC time constant of the slab-slot configuration. In (b) and (c) the RC time constant is reduced and the associated bandwidth is increased accordingly. At the same time, the increased RC corner frequency leads to an increased frequency-dependence of the RF loss, which causes additional bandwidth limitations.

of reduced device length, reduced slab capacitance C'_{S}, and increased slab conductance G'_{S} thus enables bandwidths well beyond 100 GHz.

3.5.2 Optimized doping profiles for low-loss modulators

To increase the bandwidth of the modulators, highly conductive slab regions are desirable. Increasing the doping concentration near the optical slot waveguide, however, leads to optical loss due to FCA. This effect can be mitigated by a two-step doping profile, see Fig. 3.1(b) [91, 103, 104]. Based on this approach, we suggest the following design procedure for SOH modulators:

(i) Given a certain EO material and a practical slot width, the targeted π-voltage U_π will determine the length ℓ of the modulator.

(ii) Based on the slot width, which determines the slot capacitance C'_{S}, and the length ℓ of the modulator, the targeted bandwidth determines the slab conductance G'_{S}, see, e.g., Eq. 3.6 and Fig. 3.10.

(iii) For a given slab conductance G'_{S}, the optical loss can be minimized by optimizing the two-step doping profile [103, 104]. This optimization is described in the following paragraph.

We exemplarily demonstrate the optimization of the doping profile for a device with a targeted slab conductance of $G'_{\mathrm{S}} = 102\,\mathrm{S/m}$ and a fixed slot width of 200 nm. For this device, a slot capacitance C'_{S} of about 100 pF/m can be estimated by assuming a parallel-plate approximation. This assumption has to be taken with caution since fringing fields can contribute to a significant portion of the slot capacitance [91]. For the chosen values of G'_{S} and C'_{S}, a

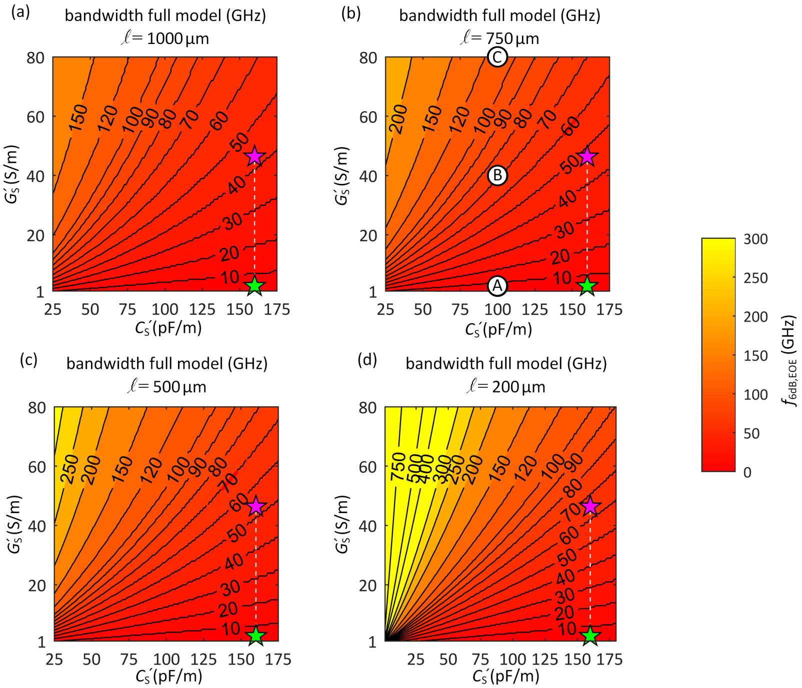

Fig. 3.10: 6 dB EOE bandwidth $f_{6\mathrm{dB,EOE}}$ for modulators of different lengths ℓ based on the full model considering all bandwidth-limiting effects. The color scale is the same as in Fig. 3.7. If the length is reduced, the bandwidth of the modulator approaches the RC-limited case depicted in Fig. 3.7. The frequency response of the 750 µm-long modulator is shown in Fig. 3.9 for the C'_S-G'_S-values indicated by Ⓐ, Ⓑ and Ⓒin (b). The parameters of the devices used in this paper for experimental verification of the model, see Table 3.1, are indicated by a green star for the case of a gate voltage of 0 V and by a magenta star for a gate voltage of 300 V.

device with length $\ell = 1$ mm, and transmission line parameters R'_{TL}, L'_{TL}, and C'_{TL} as specified in Table 3.1, the model according to Eq. 3.6 would predict a bandwidth of $f_{6\mathrm{dB,EOE}} = 114\,\mathrm{GHz}$. The geometry of the slot waveguide is fixed with a slab height of $h_{\mathrm{slab}} = 70\,\mathrm{nm}$, a rail width $w_{\mathrm{rail}} = 240\,\mathrm{nm}$, and a rail height of $h_{\mathrm{rail}} = 240\,\mathrm{nm}$ as shown in Fig. 3.11(a). The weakly doped region of the slab near the slot is depicted in green, and the more heavily doped region further away from the slot is depicted in blue in Fig. 3.11(a). As free parameters, we can vary the resistivity ρ_{heavy} of the heavily doped region as well as the resistivity ρ_{weak} and the width w_{weak} of the weakly doped part.

For simplicity, we choose a fixed resistivity ρ_{weak} of the weakly doped section in a first step, here $\rho_{\mathrm{weak}} = 5.5\times10^{-4}\,\Omega\mathrm{m}$. For a target conductance $G'_{\mathrm{S}} = 102\,\mathrm{S/m}$ of the slab, Fig. 3.11(b) shows the required bulk resistivity ρ_{heavy} of the heavily doped region as a function of its width w_{heavy}. To reach the overall target conductance of $G'_{\mathrm{S}} = 102\,\mathrm{S/m}$, the width w_{weak} of the heavily doped region must stay below 1.16 µm. The bulk resistivity in the weakly and heavily doped regions can be translated into optical loss parameters using the experimentally obtained relations published in [117]. Figure 3.11c shows the bulk power absorption coefficient α_{Si}. Note that α_{Si} refers to the optical power – in contrast to the RF attenuation coefficient α, specified in Eq. 3.4., which refers to the amplitude. The underlying model for the optical power absorption coefficient assumes a linear increase of the optical loss with the electrical conductivity in Si [117]. This assumption is only valid as long as the electrical conductivity is not limited by electron-impurity-scattering [118]. To translate the bulk absorption coefficient into a waveguide-loss parameter, we compute the optical mode in the slot waveguide and the overlap with the doped silicon region [49] using a vectorial mode solver. The resulting power absorption coefficient α_{WG} for the optical waveguide mode is shown in Fig. 3.11(d). If the weakly doped region is narrow, the heavily doped section comes close to the slot region leading to high optical loss. If the heavily doped section is far away from the slot waveguide, the conductivity has to be increased to maintain a given overall conductance G'_{S}, which again increases the optical loss. A minimum excess loss of approximately $0.048\,\mathrm{mm}^{-1}$ (0.2 dB/mm) is found for a weakly doped region with an intermediate width of $w_{\mathrm{weak}} = 1\,\mu\mathrm{m}$ and a medium resistivity of the heavily doped section of $\rho_{\mathrm{heavy}} = 1.43\times10^{-4}\,\Omega\mathrm{m}$. Note that this doping-related excess loss does not significantly change the overall propagation loss of practically used slot waveguides, which is of the order of 0.5 dB/mm [119]. Note that these loss figures are still dominated

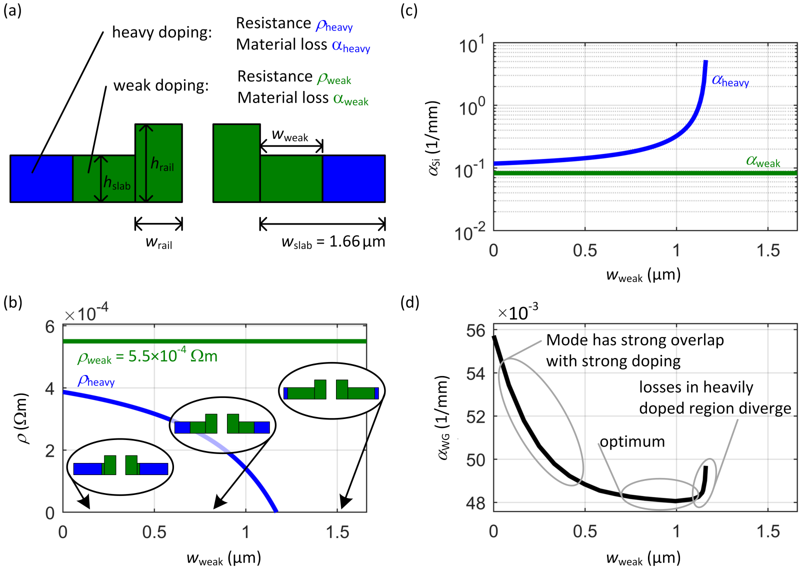

Fig. 3.11: Optimization of the doping profile in the slab-waveguide region to minimize optical loss. (a) Cross section of the slot waveguide and the adjacent slab: A low doping concentration is chosen for the rails of the slot waveguide and for the adjacent region of the slab (depicted in green), which interact strongly with the guided light. The doping is increased in the slab region that is further away from the rails (depicted in blue). We consider a waveguide with rails having a width of $w_\text{rail} = 240\,\text{nm}$ and a height of $h_\text{rail} = 220\,\text{nm}$. The slabs have a height of $h_\text{slab} = 70\,\text{nm}$ and a width of $w_\text{slab} = 1.66\,\mu\text{m}$. The width of the slot is 200 nm. For a fixed resistivity of the weakly doped silicon (here $\rho_\text{weak} = 5.5 \times 10^{-4}\,\Omega\text{m}$), w_weak and ρ_heavy can be varied to realize the target conductivity of the slab (here $G'_\text{S} = 102\,\text{S/m}$). (b) Bulk resistivity ρ_heavy in the heavily doped slab regions that is required to reach the target conductivity, specified as a function of w_weak for fixed values of $\rho_\text{weak} = 5.5 \times 10^{-4}\,\Omega\text{m}$ and $w_\text{slab} = 1.66\,\mu\text{m}$. (c) Corresponding material absorption coefficient in the doped silicon. Note that α_Si refers to the power attenuation coefficient for the optical wave, whereas the symbol α in Eq. 3.4 refers to the amplitude attenuation coefficient of the corresponding RF wave. (d) Power loss coefficient experienced by the guided optical mode, obtained from the numerically calculated optical mode field and its overlap with the doped silicon regions. An optimum in terms of optical loss is found for an intermediate extension of the heavily doped section in combination with a medium resistivity.

by the imperfections of the silicon slot waveguides and not by the organic EO cladding. The bulk absorption of the EO material is of the order of 0.1 dB/mm, and only a fraction of the optical mode propagates in the slot such that the contribution to the overall loss should be even smaller.

So far, we have only considered a fixed resistivity $\rho_\mathrm{weak} = 5.5 \times 10^{-4}\,\Omega\mathrm{m}$ of the weakly doped section. Varying this resistivity allows to further increase the bandwidth of the device or decrease its optical loss. This degree of freedom becomes particularly important when the length of the modulator is varied. For a quantitative analysis, we have repeated the optimization exemplarily described in the previous paragraph for devices of different lengths $\ell = 0.2\,\mathrm{mm}$, 0.5 mm, and 1.0 mm and for different resistivities $\rho_\mathrm{weak} = 5.5 \times 10^{-4}\,\Omega\mathrm{m}$, $16.5 \times 10^{-4}\,\Omega\mathrm{m}$, and $49.5 \times 10^{-4}\,\Omega\mathrm{m}$ of the weakly doped region. Figure 3.12 shows the resulting optical excess loss caused by absorption in the doped silicon regions for modulators of different lengths ℓ as a function of their total bandwidth $f_\mathrm{6dB,EOE}$. In this plot, the trade-off between the modulator figures of merits $U_\pi \propto \ell^{-1}$, bandwidth and insertion loss becomes evident. The numerical values presented in Fig. 3.12 suggest that it will be possible to realize SOH devices with a length of, e.g., 0.5 mm, having a bandwidth of $f_\mathrm{6dB,EOE} = 100\,\mathrm{GHz}$ while keeping the doping-related optical excess loss below 0.1 dB. Using highly efficient EO polymers [18], such a device would have a π-voltage of less than 1 V. The detailed device parameters leading to the results shown in Fig. 3.12 are depicted in Fig. 3.13. Figure 3.13(a) shows the relationship between the device bandwidth and the overall slab conductance G'_S for the three different modulator lengths ℓ considered in Fig. 3.12. The graphs are obtained from the full model according to Eq. 3.6 in combination with a slot capacitance of $C'_\mathrm{S} = 100\,\mathrm{pF/m}$ and the transmission line parameters R'_TL, L'_TL, and C'_TL as specified in Table 3.1. Figure 3.13(b) specifies the optimized resistivity ρ_heavy of the heavily doped slab region along with the associated width w_weak of the weakly doped region, see Fig. 3.13(c), and the associated power absorption coefficient α_WG for the optical waveguide mode, see Fig. 3.13(d), considering three fixed values of $\rho_\mathrm{weak} = 5.5 \times 10^{-4}\,\Omega\mathrm{m}$, $16.5 \times 10^{-4}\,\Omega\mathrm{m}$, and $49.5 \times 10^{-4}\,\Omega\mathrm{m}$.

3.6 Summary

We formulate and experimentally validate an equivalent-circuit model of SOH slot-waveguide modulators based on distributed elements that describe the electric properties of the device. The model parameters can be extracted from purely electrical measurements, that provide the frequency-dependent scattering parameters of the traveling-wave device. With these parameters, we can accurately predict the small-signal EO frequency response of the modulators, as confirmed by direct measurements of the EO frequency response. We further formulate design guidelines that lead to an optimum trade-off between EO bandwidth and optical insertion loss of SOH slot-waveguide modulators. We find that proper choice of doping concentrations and geometrical device parameters can enable SOH modulators with lengths of 0.5 mm and 6 dB EOE

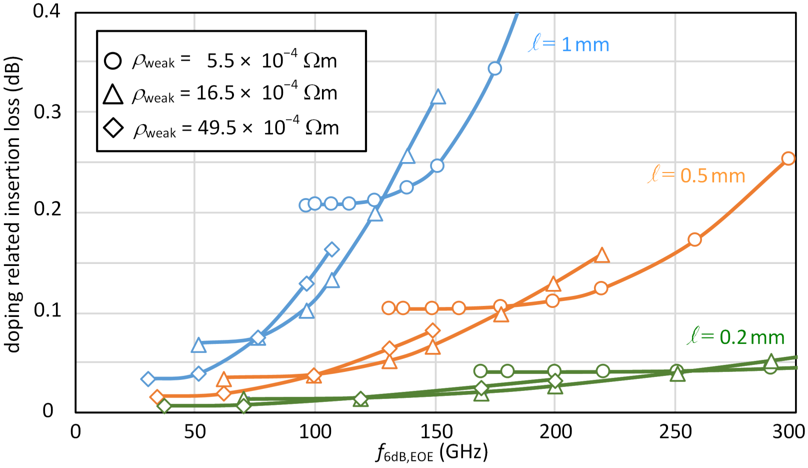

Fig. 3.12: Optical excess loss caused by absorption in the doped silicon regions for modulators of length $\ell = 0.2$ mm, 0.5 mm, and 1 mm as a function of the total 6 dB EOE bandwidth $f_{6dB,EOE}$. For each length, we consider three different resistivities ρ_{weak} of 5.5×10^{-4} Ωm, 16.5×10^{-4} Ωm, and 49.5×10^{-4} Ωm. The parameters ρ_{heavy} and w_{weak} are then optimized according to the procedure described in Fig. 3.11. For a given length of the modulator, there is a trade-off between electro-optic bandwidth and optical insertion loss. For a given bandwidth, optimizing the doping profile can lead to a reduction of optical loss. Data points are connected by interpolated lines as guide to the eye.

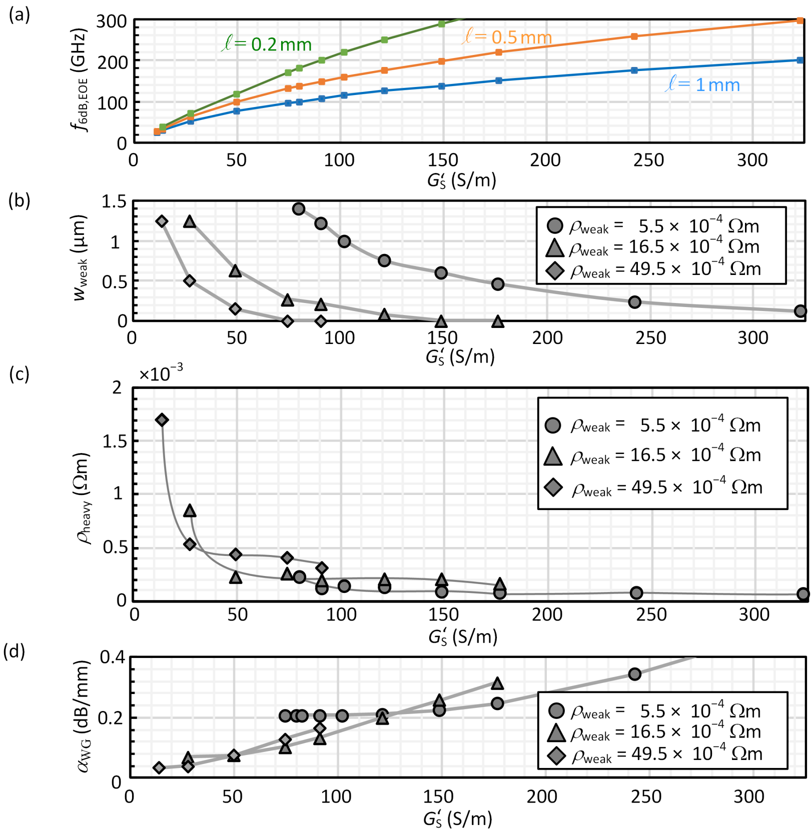

Fig. 3.13: Details of the optimized SOH modulator design for the modulators of length $\ell = 0.2$ mm, 0.5 mm, and 1 mm considered in Fig. 3.12. For each length, we consider three different resistivities ρ_{weak} of $5.5 \times 10^{-4}\,\Omega\text{m}$, $16.5 \times 10^{-4}\,\Omega\text{m}$, and $49.5 \times 10^{-4}\,\Omega\text{m}$. The parameters ρ_{heavy} and w_{weak} are then optimized according to the procedure described in Fig. 3.11. (a) Relationship between device bandwidth $f_{6\text{dB,EOE}}$ and overall slab conductance G'_{S} for three different modulator lengths. (b) Optimized width w_{weak} of the weakly doped region, (c) the associated resistivity ρ_{heavy} of the heavily doped slab region, and (d) the associated power absorption coefficient for the optical mode in the doped region of the silicon, all as a function of slab conductance G'_{S}, considering the three fixed values of ρ_{weak}. Data points in all subfigures are connected by interpolated lines as guide to the eye.

bandwidths of more than $f_{6\mathrm{dB,EOE}} = 100\,\mathrm{GHz}$ while maintaining π-voltages of less than 1 V and while keeping the optical excess loss caused by free-carrier absorption in the doped silicon regions below 0.1 dB.

3.7 Mathematical relations for de-embedding the radio-frequency characteristics of on-chip modulators

[This section was published as Appendix A of [J1]]

Transfer matrices of contact pads
The transfer matrix (T-matrix) of the left-hand-side contact pad including the subsequent transition to the modulator electrodes, see Fig. 3.3(a), is modeled by a series impedance $\underline{Z}$ and a shunt admittance $\underline{Y}$

$$\underline{T}_\mathrm{L} = \begin{pmatrix} 1 & 0 \\ \underline{Y} & 1 \end{pmatrix} \begin{pmatrix} 1 & \underline{Z} \\ 0 & 1 \end{pmatrix} = \begin{pmatrix} 1 & \underline{Z} \\ \underline{Y} & \underline{Y}\,\underline{Z} + 1 \end{pmatrix}. \tag{3.22}$$

Similarly, the T-matrix of the right-hand-side contact pad including the subsequent transition to the modulator electrodes is modeled by the same series impedance $\underline{Z}$ and a the same shunt admittance $\underline{Y}$

$$\underline{T}_\mathrm{R} = \begin{pmatrix} 1 & \underline{Z} \\ 0 & 1 \end{pmatrix} \begin{pmatrix} 1 & 0 \\ \underline{Y} & 1 \end{pmatrix} = \begin{pmatrix} \underline{Y}\,\underline{Z} + 1 & \underline{Z} \\ \underline{Y} & 1 \end{pmatrix}. \tag{3.23}$$

Conversion between S-parameters and T-matrix parameters For conversion between S-parameters and electrical T-matrix parameters, we use the following relation [87, 89]:

$$\begin{aligned}
\underline{T}_{11} &= \frac{1+\underline{S}_{11}-\underline{S}_{22}-\Delta\underline{S}}{2\underline{S}_{21}} \\
\underline{T}_{12} &= \underline{Z}_{\text{ref}}\frac{1+\underline{S}_{11}+\underline{S}_{22}+\Delta\underline{S}}{2\underline{S}_{21}} \\
\underline{T}_{21} &= \frac{1}{\underline{Z}_{\text{ref}}}\frac{1-\underline{S}_{11}-\underline{S}_{22}+\Delta\underline{S}}{2\underline{S}_{21}} \\
\underline{T}_{22} &= \frac{1-\underline{S}_{11}+\underline{S}_{22}-\Delta\underline{S}}{2\underline{S}_{21}}
\end{aligned} \tag{3.24}$$

In these relations, $\Delta\underline{S} = \underline{S}_{11}\underline{S}_{22} - \underline{S}_{21}\underline{S}_{12}$, and $\underline{Z}_{\text{ref}}$ is the reference impedance of the measurement system.

Transfer matrix of a transmission line The transfer matrix of a transmission line of length ℓ with propagation parameter $\underline{\gamma}$ and characteristic impedance $\underline{Z}_0$ is given by [87, 89]

$$\underline{T} = \begin{pmatrix} \cosh(\underline{\gamma}\ell) & \underline{Z}_0 \sinh(\underline{\gamma}\ell) \\ \frac{1}{\underline{Z}_0}\sinh(\underline{\gamma}\ell) & \cosh(\underline{\gamma}\ell) \end{pmatrix}. \tag{3.25}$$

3.8 Low-frequency characteristic impedance of a transmission line

[This section was published as Appendix B of [J1]]

The characteristic impedance given in its standard form by [87] $\underline{Z}_0 = \sqrt{(R' + \mathrm{j}\omega_{\text{RF}}L')(G' + \mathrm{j}\omega_{\text{RF}}C')}$ is oftentimes considered for low-loss transmission lines at high frequencies only, where $\omega_{\text{RF}}L' \gg R'$ and $\omega_{\text{RF}}C' \gg G'$ holds. The characteristic impedance can then be approximated by a real-valued constant

$$Z_0 \approx \sqrt{\frac{L'}{C'}}. \tag{3.26}$$

Note that this approximation is not valid for the low-frequency region where $\underline{Z}_0$ can be complex and frequency-dependent and the real and imaginary part may diverge for $\omega_{\mathrm{RF}} \to 0$.

3.9 Loss parameter of the RC element

[This section was published as Appendix C of [J1]]

In this section we derive the RF amplitude attenuation parameter α_{RC} associated with the loss of the RC element formed by the slab resistance $G_{\mathrm{S}}'^{-1}$ and the slot capacitance C_{S}' following the approach in [91]. The active power dissipated in the RC element of an infinitesimally short section of the transmission line is linked to the real part of the complex line admittance $\underline{Y}_{\mathrm{RC}}'\mathrm{d}z$

$$\mathrm{d}P = -\Re\left\{|\underline{U}|^2 \underline{Y}_{\mathrm{RC}}'^{*}\right\}\mathrm{d}z, \tag{3.27}$$

where $\underline{U}$ denotes the voltage phasor and where the admittance $\underline{Y}_{\mathrm{RC}}'$ of the RC element is given by

$$\underline{Y}_{\mathrm{RC}}' = \left(\frac{1}{G_{\mathrm{S}}'} + \frac{1}{\mathrm{j}\omega_{\mathrm{RF}} C_{\mathrm{S}}'}\right)^{-1} = \frac{\omega_{\mathrm{RF}}^2 C_{\mathrm{S}}'^2 G_{\mathrm{S}}^{-1} + \mathrm{j}}{1 + \left(\omega_{\mathrm{RF}} C_{\mathrm{S}}' G_{\mathrm{S}}'^{-1}\right)^2}. \tag{3.28}$$

The active power that is transported on the entire transmission line is given by $P = \Re\left\{\frac{\underline{U}\underline{U}^*}{\underline{Z}_0^*}\right\}$ such that the ratio of the power lost in the RC element and the total power entering the infinitesimally short section is given by

$$\frac{\mathrm{d}P}{P} = -\frac{\omega_{\mathrm{RF}}^2 C_{\mathrm{S}}'^2 G_{\mathrm{S}}^{-1}}{1 + (\omega_{\mathrm{RF}} C_{\mathrm{S}}' G_{\mathrm{S}}'^{-1})^2} \frac{1}{\Re\left\{\underline{Z}_0^{-1}\right\}}\mathrm{d}z. \tag{3.29}$$

This differential equation is solved by $P = P_0 \exp(-2\alpha_{\mathrm{RC}} z)$, where the additional factor of two in the argument arises from the fact that α_{RC} refers to the amplitude rather than the power attenuation. The amplitude attenuation parameter can thus be written as

$$\alpha_{\mathrm{RC}} = \frac{\omega_{\mathrm{RF}}^2 C_{\mathrm{S}}'^2 G_{\mathrm{S}}^{-1}}{1 + (\omega_{\mathrm{RF}} C_{\mathrm{S}}' G_{\mathrm{S}}'^{-1})^2} \frac{1}{2\mathfrak{R}\left\{\underline{Z}_0^{-1}\right\}}. \tag{3.30}$$

[End of paper [J1]]

4 SOH modulators for intensity-modulation/direct-detection links

This chapter reports on the demonstration of SOH modulators in data transmission experiments using intensity-modulation and direct-detection (IM/DD). It was published in a scientific journal [J2]. The material from the publication was adapted to comply with the layout and structure of this thesis.

[Beginning of Paper [J2]. Reprinted with permission ©The Optical Society.]

Silicon-organic hybrid (SOH) modulators for intensity-modulation / direct-detection links with line rates of up to 120 Gbit/s

Optics Express, Vol. 25, Issue 20, pp. 23784-23800 (2017)

DOI: `https://doi.org/10.1364/OE.25.023784`

Heiner Zwickel,[1] Stefan Wolf,[1] Clemens Kieninger,[1,2] Yasar Kutuvantavida,[1,2] Matthias Lauermann,[1,3] Timothy de Keulenaer,[4,5] Arno Vyncke,[4,5] Renato Vaernewyck,[4,5] Jingdong Luo,[6] Alex K.-Y. Jen,[6] Wolfgang Freude,[1] Johan Bauwelinck,[4] Sebastian Randel,[1] and Christian Koos[1,2]

[1] Institute of Photonics and Quantum Electronics (IPQ), Karlsruhe Institute of Technology (KIT), Germany

[2] Institute of Microstructure Technology (IMT), Karlsruhe Institute of Technology (KIT), Germany

[3] Now with Infinera Corporation, Sunnyvale, CA 94089, USA

[4] Ghent University imec, IDLab, Department of Information Technology, Ghent, Belgium

[5] BiFAST, Ghent, Belgium

[6] Department of Material Science and Engineering, University of Washington, Seattle, Washington, USA

High-speed interconnects in data-center and campus-area networks crucially rely on efficient and technically simple transmission techniques that use IM/DD to bridge distances of up to a few kilometers. This requires electro-optic modulators that combine low operation voltages with large modulation bandwidth and that can be operated at high symbol rates using integrated drive circuits. Here we explore the potential of SOH MZMs for generating high-speed IM/DD signals at line rates of up to 120 Gbit/s. Using a SiGe bipolar CMOS (BiCMOS) signal-conditioning chip, we demonstrate that IDB signaling allows to efficiently use the electrical bandwidth, thereby enabling line rates of up to 100 Gbit/s at bit error ratios (BER) of 8.5×10^{-5}. This is the highest data rate achieved so far using a silicon-based MZM in combination with a dedicated signal-conditioning IC. We further show PAM4 at lines rates of up to 120 Gbit/s ($\mathrm{BER} = 3.2 \times 10^{-3}$) using a high-speed arbitrary waveform generator (AWG) and a 0.5 mm-long MZM. This is the highest data rate hitherto achieved with a sub-millimeter MZM on the silicon photonic platform.

4.1 Introduction

High-speed optical communication links in data-center and campus-area networks urgently call for efficient high-speed EO modulators that can be densely integrated at low cost. This need is, e.g., witnessed by the Ethernet Alliance, creating "The Holy Grail of 100GbE SFP+"-challenge that targets a single-wavelength 100 Gbit/s transceiver in a 1.5 W SFP+ package (SFP: small form factor pluggable) [120]. This competition was driven by the expectation that grouping of 100 Gbit/s lanes will enable interface rates of 400 Gbit/s, 0.8 Tbit/s or 1.6 Tbit/s that are already foreseen for future Ethernet standards [121]. To meet the associated scalability challenges, system complexity must be kept low by using simple transmission schemes based on IM/DD as opposed to more demanding coherent communication schemes. In addition, due to growing areal network extension, the transmitters must be able to generate data signals with low chirp that can be sent over distances of up to a few kilometers. This rules out direct modulation concepts using, e.g., compact and efficient vertical-cavity surface-emitting laser (VCSEL) [122], and requires external modulation of continuous-wave carriers.

External modulation schemes can rely on MZMs or on electro-absorption modulators (EAMs). EAMs have been demonstrated both on the InP and the silicon photonic platform, enabling line rates of up to 100 Gbit/s with SiGe BiCMOS signal-conditioning chips [123,124]. However, EAM-based schemes generally suffer from a trade-off between ER and chirp, with typical chirp parameters $\alpha^{(c)}$ of experimentally generated data signals exceeding $|\alpha^{(c)}| > 1$ for an ER of 10 dB [125]. In contrast to that, MZMs may feature arbitrarily high ER while allowing for push-pull operation with zero chirp. High-speed IM/DD transmission has previously been demonstrated using an MZM based on an organic EO polymer for 100 Gbit/s OOK [126, 127]. While this device exploits the Pockels effect in the EO polymer to provide a negligible chirp parameter of $\alpha^{(c)} = -0.02$, it still features a large length in excess of 6 mm, dictated by the comparatively low EO coefficient of $r_{33} = 86$ pm/V as well as by the rather large optical mode field and the associated spacing of the microstrip transmission line electrodes. The device length can be slightly reduced to approximately 4 mm by using high-speed InP-based MZMs [128, 129]. These devices, however, still have rather high voltage-length products of more than 5 Vmm [130], and rely on fabrication processes that are rather expensive and limited in scalability as compared to CMOS-based silicon photonic integration. Silicon photonic depletion-type pn-modulators have been shown to support PAM4 signaling at impressive line rates up to 168 Gbit/s [92]. These devices, however, are subject to the intrinsically limited efficiency of the underlying phase modulators, featuring voltage-length products $U_\pi L$ in excess of 6 Vmm for optimized devices [72] and in excess of 30 Vmm [131] for the 4.8 mm-long high-speed MZM used in [92]. This leads to large device lengths and high drive voltages, which require dedicated amplifiers. Moreover, free carriers in the pn-junction do not only modulate the real part of the refractive index, but also the imaginary part, thereby leading to amplitude-phase coupling and hence to nonzero chirp parameters of, e.g., $|\alpha^{(c)}| = 0.8$ even for well-balanced push-pull devices [132]. Another approach to realize high-speed MZMs relies on the concept of POH integration [133]. POH MZMs combine ultra-small footprint [134] with unprecedented modulation bandwidths that enable data rates of up to 120 Gbit/s for PAM4 signaling [135]. These devices, however, suffer from an inherent trade-off between insertion loss and operation voltage [49], requiring peak-to-peak voltage swings of 8 $\mathrm{V_{pp}}$ that become effective when applying a 4 $\mathrm{V_{pp}}$ drive signal to an unterminated MZM [135]. In addition, with the exception of the all-polymer device [126, 127], all signaling experiments of high-speed MZMs have relied on drive signals generated by benchtoptype laboratory test equipment [128, 129, 135, 136]. The associated electronic circuits feature high power consumption and are unsuited for integration into small form-factor packages.

In this paper, we present a series of IM/DD transmission experiments, showing that these limitations can be overcome by highly efficient SOH MZMs, which can be operated by BiCMOS signal-conditioning chips. SOH modulators rely on silicon photonic slot waveguides that are embedded into organic EO cladding materials, thereby combining the advantages of large-scale CMOS fabrication with the wealth of optical properties obtained by molecular engineering of organic materials [48, 49]. The devices feature small footprints along with low modulation voltages, quantified by small voltage-length products down to 0.32 Vmm [56, 83] – more than an order of magnitude below those of conventional depletion-type pn modulators [72]. We characterize our SOH modulators with respect to ER and chirp and show that the devices can be operated with negligible chirp parameters of $|\alpha^{(c)}| = 0.09$. Moreover, expanding on earlier work [137], we demonstrate IDB as a way to relax the bandwidth requirements for driver electronics, modulators and receivers in IM/DD transmission schemes. We demonstrate 100 Gbit/s IDB transmission over a dispersion-compensated link of 5 km of standard single-mode fiber (SSMF) by operating an SOH MZM with a 130 nm SiGe BiCMOS signal-conditioning chip. We measure a bit error ratio (BER) of 1.6×10^{-3} (8.5×10^{-5}) for the fiber transmission (back-to-back reference), which is well below the threshold of hard-decision forward-error correction (FEC) with 7% overhead [138]. This represents, to the best of our knowledge, the highest data rate that has been achieved with a silicon-based MZM operated by a dedicated signal-conditioning chip. Moreover, we demonstrate generation of PAM4 signals at line rates (symbol rates) up to 120 Gbit/s (60 GBd) using a silicon-based modulator [139]. Despite the small device length of only 0.5 mm, the modulator's energy consumption amounts to $W_{\text{bit}} = 100$ fJ/bit, which is significantly smaller than the 410 fJ/bit demonstrated for a 4.8 mm long depletion-type modulator at a comparable PAM4 line rate of 112 Gbit/s [92]. To the best of our knowledge, our demonstration corresponds to the highest data rate hitherto achieved using a sub-millimeter MZM on the silicon photonic platform. The MZMs are fabricated in a commercial silicon photonics line and along with the full portfolio of standard silicon photonic devices.

This chapter is structured as follows: Section 4.2 introduces the SOH device concept and reports on the characterization of the MZM with respect to chirp. In Section 4.3, we explore OOK using SOH modulators in combination with integrated BiCMOS signal-conditioning chips, achieving error-free transmission at data rates of 50 Gbit/s. As a straightforward way to increase the data rates, we use PAM4 signaling at line rates of up to 120 Gbit/s. These experiments, reported in Section 4.4, however, rely on a high-speed AWG that generates the multi-level drive signals. Section 4.5 finally introduces IDB as an alternative path towards high-speed signaling. IDB significantly relaxes the bandwidth requirements of the driver electronics, enabling data rates of up to 100 Gbit/s IDB with BiCMOS signal-conditioning ICs. Details on the modulation formats and the experimental methods are given in Section 4.7 and 4.8.

4.2 Silicon-organic hybrid Mach-Zehnder modulators

The basic concept of an SOH MZM fabricated in SOI technology is shown in Fig.4.1. Each arm of the modulator consists of a silicon photonic slot waveguide, comprising two 240 nm-wide and 220 nm-high silicon rails which are separated by a 120 nm to 160 nm-wide slot. The modulating drive signal is guided by a coplanar GSG aluminum (Al) transmission line. The modulating RF signal co-propagates with the optical carrier along the (0.5...1.1) mm-long modulator. The electrodes are connected through Al vias to the silicon rails of the slot waveguide by 70 nm-thin conductive n-doped silicon slabs. The electrical RF voltage drops mainly across the narrow slot where the light is highly confined, thus leading to a strong overlap of the optical mode and the modulating electric field – a key advantage in comparison to conventional organic electro-optic modulators [126, 127]. The device is functionalized by filling and coating the slot waveguide with an EO organic cladding material.

This strip-loaded slot waveguide design clad with EO organic material was first demonstrated to work as an EO modulator at RF frequencies by Ding et al. [50]. We use the commercially available EO material SEO100 which combines a large EO coefficient of $r_{33} = 144\,\mathrm{pm/V}$ with good thermal stability. Using this material, high-speed operation of an SOH modulator at 80°C has been

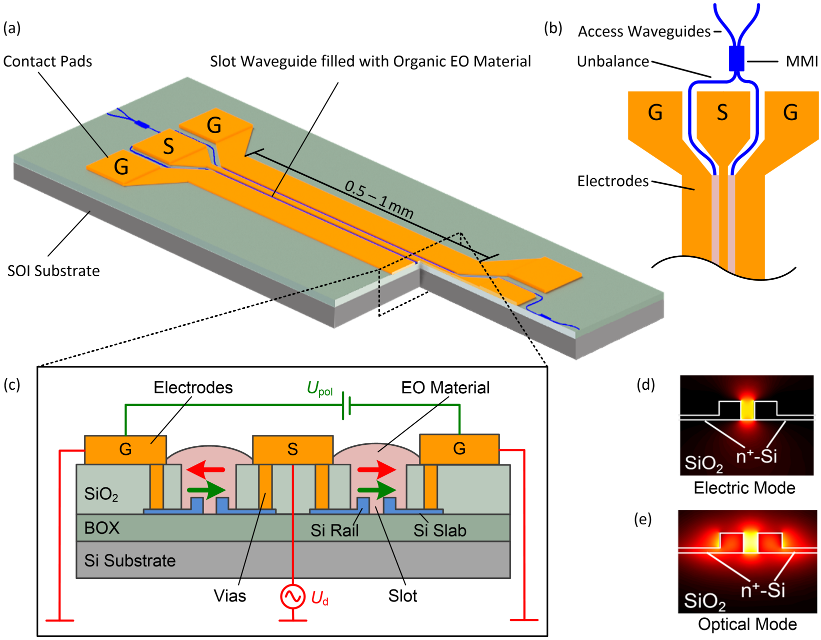

Fig. 4.1: Device concept of an silicon-organic hybrid (SOH) Mach-Zehnder modulator (MZM). (a) The device is fabricated in a standard commercial fabrication run on a silicon-on-insulator wafer. (b) Shows a top view of the electrodes with contact pads in ground-signal-ground configuration. The light is split by a multi-mode-interference (MMI) coupler into the two arms of the MZM. (c) Shows the cross section of the SOH MZM. Each arm comprises an optical slot waveguide filled with an electro-optic organic cladding material. The GSG transmission line for the electrical signal is connected to the rails of the slot waveguide by thin conductive n-doped silicon slabs and aluminum (Al) vias through the protective oxide cladding. During the poling process, a direct current (DC) voltage U_{pol} (green circuit) is applied across the floating ground electrodes at an elevated temperature of the device. The molecules align according to the poling voltage and remain in that orientation (green arrow) after cooling down the device. A modulating voltage U_{d} applied to the signal electrode induces an electric field in the slot (red arrow) that is anti-parallel (parallel) in the left (right) arm of the MZM leading to push-pull operation. Due to the high overlap of the RF electric field (d) and the optical mode (e) in the slot waveguide the modulation is highly efficient.

demonstrated previously [21]. To activate the macroscopic $\chi^{(2)}$-nonlinearity, the microscopic molecular dipoles in the organic material need to be aligned in a dedicated one-time poling process. To this end, a poling voltage U_{pol} is applied across the (floating) ground electrodes at an elevated temperature to align the EO-active chromophores. At the operating temperature and after removal of the poling voltage, the molecule orientation remains in the aligned state indicated by green arrows, Fig.4.1(c). The modulating field (red arrows) induced by the RF drive voltage U_{d} is oriented parallel to the chromophore alignment in one phase modulator and antiparallel in the other phase modulator, which results in a push-pull operation of the MZM. In the devices used for the transmission experiments, we measure an MZM voltage-length product $U_\pi L$ of 1.1 Vmm at DC. This value can be reduced to 0.5 Vmm or below by using more efficient EO materials [56, 83]. Our devices were fabricated in a standard 248 nm deep-UV (DUV) process on a commercial platform, which offers a full portfolio of silicon photonic devices and SiGe detectors.

SOH MZMs exploit the Pockels effects in the organic cladding and should hence allow for chirp-free modulation provided that perfectly balanced push-pull operation is achieved. To experimentally confirm this aspect, we characterized the chirp properties of an SOH MZM. In general, signal chirp is quantified by the chirp parameter $\alpha^{(\mathrm{c})}$, which relates the modulation of the phase ϕ to the modulation of the time-dependent power P of the optical signal averaged over a few optical cycles,

$$\alpha^{(\mathrm{c})} = 2P \frac{\mathrm{d}\phi/\mathrm{d}t}{\mathrm{d}P/\mathrm{d}t}. \tag{4.1}$$

For a direct measurement of the chirp parameter, we exploit the fiber response peak method [140]. To this end, we use a network analyzer to measure the small-signal intensity modulation transfer function of the modulator connected to a 75 km-long fiber span and a calibrated photodiode [99]. The measured frequency response is shown in Fig. 4.2(a). The product of the square of the resonance frequency f_u and the fiber length L is plotted versus the dip order u in Fig. 4.2(b). The chirp parameter $\alpha^{(\mathrm{c})}$ and the fiber dispersion D can then be extracted from the slope and from the vertical offset of a straight line fitted to the data points by using the simple relation $f_u^2 L = \mathrm{c}/(2D\lambda^2)\left(1 + 2u - 2\arctan(\alpha^{(\mathrm{c})})/\pi\right)$ with λ being the wavelength of the optical carrier and c denoting the vacuum speed of light [140]. Our mea-

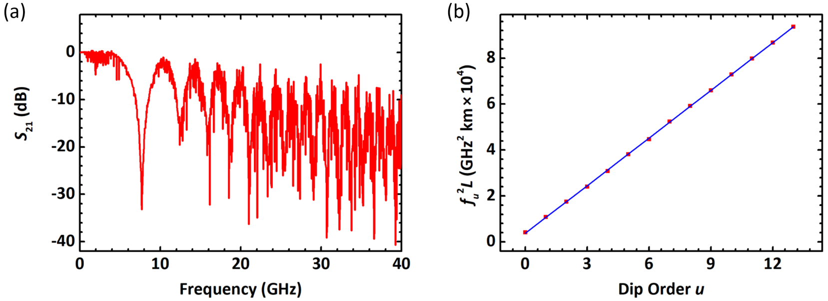

Fig. 4.2: Chirp characterization of an SOH MZM using the fiber response peak method [140]. (a) Transfer function for small-signal intensity modulation of the SOH MZM connected to a 75 km-long fiber span. Dips in the transfer function originate from fiber dispersion. (b) For data evaluation, the product of the square of the resonance frequency f_u and the fiber length L is plotted versus the dip order u. The chirp parameter $\alpha^{(c)}$ and the fiber dispersion D can then be extracted from the slope and from the vertical offset of a straight line fitted to the data points [99, 140]. We find a chirp factor of $|\alpha^{(c)}| \approx 0.09$.

surements lead to a dispersion coefficient of 16.8 ps/(nm km) and a small but nonzero chirp parameter of $|\alpha^{(c)}| = 0.09$, which is attributed to a slight imbalance of the two MZM arms evidenced by a finite static ER of 31 dB, see [99]. The measured chirp parameter is well below the value of $|\alpha^{(c)}| = 0.8$ found for pn-type MZMs [132] and significantly below the chirp parameters $|\alpha^{(c)}| > 1|$ that are expected for EAMs at reasonable extinction ratio [125].

4.3 Non-return-to-zero (NRZ) on-off keying (OOK) with an SOH MZM

In a first set of transmission experiments, we explore the potential of simple non-return-to-zero (NRZ) OOK as a modulation format. For generating the data signal, we bias the MZM at its quadrature point and apply a drive voltage with a swing of U_π. For rectangular pulses the data rate f_d equals the symbol rate f_s, and the required bandwidth is f_d (see Section 4.7)). While the electrical circuit to drive the MZM is relatively simple, OOK is demanding in terms of bandwidth so that it is challenging to move to high symbol rates. Recently, the generation and transmission of NRZ-OOK data at 100 Gbit/s

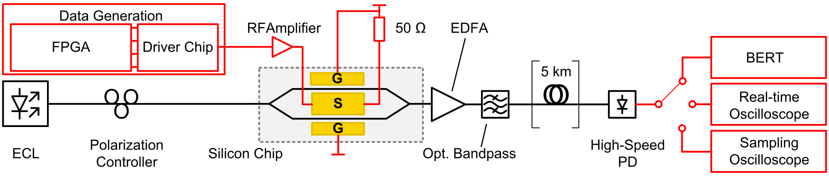

Fig. 4.3: Experimental setup for data transmission with an SOH modulator and a BiCMOS signal-conditioning IC: The signal-conditioning chip is fed by 4×12.5 Gbit/s or 4×25 Gbit/s pseudo-random binary sequences (PRBS) to generate a 50 Gbit/s OOK signal or a 100 Gbit/s duobinary (DB) signal. The output of the IC connects via a coaxial cable to an RF amplifier and a microwave probe to the SOH MZM. The modulator is terminated by a 50 Ω impedance. Light from a laser source is coupled to the silicon chip via grating couplers. After modulation, the optical signal is amplified, optionally transmitted over a 5 km long fiber and detected on a photodiode. The PD can be connected to a bit error ratio tester (BERT), a sampling oscilloscope and a real-time oscilloscope.

using SOH modulators could be shown, where high-performance laboratory equipment controlled the modulator [136]. While this demonstration showed that SOH modulators outperform all alternative semiconductor based modulators in terms of speed and drive voltage, the implementation in a transmitter is rather complicated. First, the generation of electrical 100 Gbit/s signals requires components with high bandwidth. Second, the imperfect signal transmission (e.g. dispersion) requires error correction in the form of FEC, and this asks for digital signal processing (DSP).

In our experiment the 50 Gbit/s OOK signal is conditioned by an integrated circuit which comprises a 4:1 serializer, a 6-tap feed-forward equalizer, and an output stage delivering a voltage of up to 1 V_{pp}. The IC is fabricated in a 0.13-µm SiGe BiCMOS technology. The FFE is realized as a tapped delay line with around 9 ps to 10 ps spacing. More information on the signal-conditioning IC can be found in [124] and [141]. The experimental setup is depicted in Fig. 4.3. A PRBS(length $2^7 - 1$) is generated in an FPGA and feeds the signal-conditioning chip which is embedded in a connectorized testboard. The outputs of the board are connected to an RF amplifier with a bandwidth of 70 GHz, which finally drives the SOH MZM via microwave probes. The modulator is biased at its quadrature point and terminated with an external 50 Ω impedance. An external cavity laser (ECL) provides the optical carrier at a wavelength of 1550 nm. A band-pass filter with a 1.5 nm-wide passband removes out-of-band ASE noise. The photodiode (PD) receives the transmitted signal. The

PD output is connected to a BERT, to a sampling oscilloscope, or to a 62 GHz real-time oscilloscope. In our experiment, the optical signals are coupled to and from the silicon chip via grating couplers and single-mode fibers. The fiber-to-fiber insertion loss of 18 dB is compensated by an EDFA. This insertion loss is caused by non-optimized grating couplers, imperfect strip-to-slot waveguide transitions, and by waveguide losses. The on-chip loss amounts to approximately 9 dB, of which a total of approximately 2.5 dB is attributed to access waveguides, two MMI couplers, and four strip-to-slot converters. The remaining approximately 6.5 dB of loss are caused by the 1.1 mm-long slot-waveguide sections in each arm. With improved processes, the on-chip loss can be significantly reduced: Slot waveguides can be fabricated with propagation losses as low as 0.65 dB/mm [119], and an optimized doping profile can reduce the doping-related losses to below 1 dB/mm [21]. Note that this performance can well compete with the most advanced depletion-type pn modulators. First, the voltage-length product of $U_\pi L = 1.1\,\mathrm{Vmm}$ is significantly lower than $U_\pi L$-products of 6 Vmm that have been reported for advanced depletion-type pn-modulators. Moreover, despite the high slot-waveguide propagation losses of the current device generation, SOH modulators can well compete even with the most advanced depletion-type pn modulators in terms of the voltage-length-loss product $aU_\pi L$, where a denotes the waveguide loss coefficient in the phase shifter section: Best-in-class depletion-type pn modulators feature $aU_\pi L$-products down to 12 dBV [72], whereas 6.5 dBV are obtained for the SOH devices used in the current experiment, with the potential to reduce this value further to below 1 dBV. Regarding device capacitance, values of 400 fF/mm have been demonstrated for SOH modulators [56], which is clearly below the 830 fF/mm measured for highly efficient depletion-type pn devices [142]. This in combination with the higher modulation efficiency leads to clear advantages in terms of the charge that needs to be transferred to the device to achieve a certain phase shift, see [49] for a more detailed discussion.

Figure 4.4 shows eye diagrams recorded with a sampling oscilloscope. The BER is measured with a BERT. At 50 Gbit/s we find no errors in the data transmitted over a 5 km dispersion-compensated fiber link (evaluating 5×10^{10} bit, BER$< 2 \times 10^{-9}$). From the eye diagram we extract the quality factor (Q-factor) which is $Q = 7.0$. For a back-to-back measurement we find no errors in a data stream of 3.4×10^{12} bit (BER$< 3 \times 10^{-11}$) and a Q-factor of $Q = 10.3$. The energy consumption of the modulator is estimated to be 730 fJ/bit, see Section 4.8. Note that the modulator itself would allow even

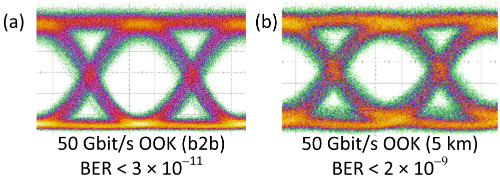

Fig. 4.4: Eye diagrams and BER for 50 Gbit/s OOK signaling. (a) Back-to-back (b2b) configuration (b) Transmission over a 5 km-long dispersion compensated fiber.

higher data rates in the range of 100 Gbit/s if larger BER can be tolerated [136], and also the SiGe BiCMOS circuits can be pushed by a better optimization of the feed-forward equalizer (FFE) coefficients [123]. However, in an integrated system, the electro-optic bandwidth will eventually be limited by the parasitic effects of the RF packaging and assembly concepts. In the subsequent sections, we therefore explore two bandwidth-saving modulation formats for increasing the data rate.

4.4 Non-return-to-zero (NRZ) PAM4 signaling with an SOH MZM

To relax bandwidth requirements for the transmitter and the receiver, multilevel signaling can be employed. With PAM4, four signal levels are used to encode two bit into each symbol. For the same data rate f_d, the symbol rate and hence the bandwidth can be reduced by a factor of two as compared to OOK (see Section 4.7). The required electronic circuitry for PAM4 is, however, more complex than for OOK due to multiple signal levels. For a proof-of-concept demonstration, we use an AWG rather than the BiCMOS IC.

The experimental setup is depicted in Fig. 4.5. The electrical drive signals are generated in a 92 GSa/s AWG (Keysight M8196A). An RF amplifier boosts the output to a peak-to-peak voltage of 2.1 V, which is fed to the Si chip using microwave probes. We use a PRBS with a length of $2^{11} - 1$ along with sinc-like pulse shapes featuring a raised-cosine spectrum with a roll-off factor $\beta^{(\mathrm{ro})} = 0.35$. A pre-compensation flattens the end-to-end frequency response of the setup. As with the previously described experiment, an external 50 Ω

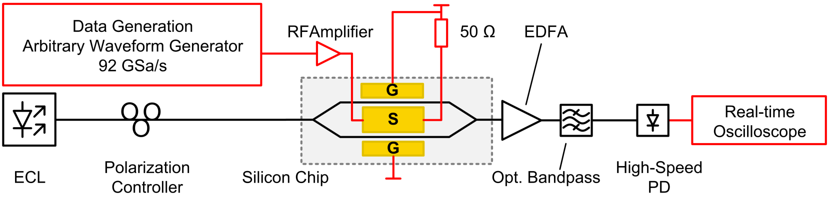

Fig. 4.5: Experimental setup for PAM4 signal generation: The electrical drive signals are generated in an arbitrary waveform generator (AWG), amplified in a radio frequency (RF) amplifier, and fed to the modulator via microwave probes. The modulator is electrically terminated with an external 50 Ω impedance. Light from a laser source is coupled to the chip via grating couplers. After modulation, the optical signal is amplified, band-pass filtered and detected on a photodiode (PD) connected to a high-speed oscilloscope.

impedance terminates the electrical transmission line of the modulator. The optical carrier with a wavelength of 1550 nm is provided by an ECL and coupled to and from the 0.5 mm-long SOH MZM via grating couplers. A subsequent EDFA compensates the modulator's fiber-to-fiber insertion loss, and a 0.6 nm optical bandpass filter is used to remove the out-of-band ASE noise of the EDFA. The signal is detected by a photodiode having a bandwidth of 50 GHz. The data are then recorded by a real-time oscilloscope having a 32 GHz analog bandwidth. The BER is directly measured.

We demonstrate PAM4 modulation for symbol rates up to 60 GBd. The modulator is 0.5 mm long, biased at its quadrature point and driven with a voltage of 2.1 V_{pp}. Figure 4.6 shows the recorded eye diagrams with symbol rates of 28 GBd, 40 GBd, 56 GBd and 60 GBd. For the 28 GBd signal, no bit errors could be measured in our 78 µs long recordings, which corresponds to a BER $< 2.29 \times 10^{-5}$. For 40 GBd, 56 GBd, and 60 GBd, the BER was measured to be 2.4 × 10–4, 9.1×10^{-4} and 3.2×10^{-3}, respectively. The BER increases with increasing symbol rate because the pre-compensation of the low-pass characteristic of driver electronics and modulator emphasizes high-frequency noise. For all symbol rates, the BER is below the threshold 4.4×10^{-3} of hard-decision FEC with 7% overhead [138]. The maximum line rate is 120 Gbit/s, which corresponds to a net data rate of 112 Gbit/s. At the time of initial publication [139], this experiment represented the highest IM/DD data rate achieved on the silicon photonic platform. Despite the small device length of only 0.5 mm, the modulator's energy consumption amounts to $W_{\text{bit}} = 100$ fJ/bit, see Section 4.8. This is significantly smaller than the 410 fJ/bit demonstrated

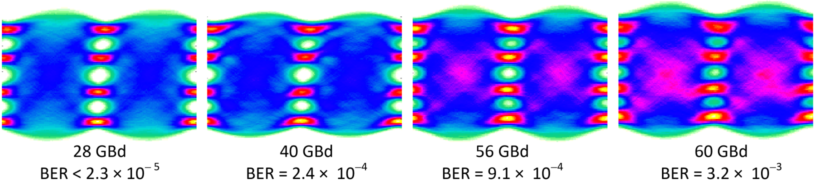

Fig. 4.6: PAM4 eye diagrams for symbol rates of 28 GBd, 40 GBd, 56 GBd and 60 GBd along with the measured bit error ratio. At 28 GBd, no bit error was found in our recording. The BER increases with the symbol rate because the pre-compensation of the low-pass characteristic of driver electronics and modulator emphasizes high-frequency noise. For all measured symbol rates, the BER stays below 4.4×10^{-3}, which represents the threshold for hard-decision forward-error correction with 7% overhead.

for a 4.8 mm-long depletion-type modulator at a comparable PAM4 line rate of 112 Gbit/s [92]. Note that even higher data rates can be achieved by using coherent transmission schemes along with advanced modulation formats such as 16QAM [101, 143, 144]. However, the associated transmitter and receiver circuitry is technically much more demanding than the rather simple IM/DD scheme used here, which does not require powerful DSP or coherent receivers. While the pre-emphasis used in our PAM4 demonstration as well as the coding and decoding of the four-level signal requires some DSP, the processing effort is much reduced compared to coherent modulation formats.

4.5 Demonstration of three-level intensity-modulated duobinary (IDB)

PAM4 signal generation and equalization requires complex signal processing schemes which prevent the construction of simple integrated driver chips. The data rate achieved with OOK, on the other hand, is limited by the bandwidth of the modulator and the driver electronics. To increase the line rate for a given bandwidth, we explore the bandwidth-saving duobinary (DB) modulation format as alternative to PAM4, see Section 4.7. With a setup change of the BiCMOS signal-conditioning chip in Fig. 4.3, three-level duobinary signals are generated. As with OOK, the modulator is biased at its quadrature point and driven with zero, positive and negative voltages. This leads to three optical power levels, which correspond to the signal levels (0, $A/2$, A) used in the

Section 4.7. We refer to this format as intensity-modulated duobinary (IDB). Note that IDB is different from optical duobinary (ODB) [145], where the modulator is biased at the null-point, and the peak-to-peak drive signal swing U_d is twice the π-voltage U_π of the MZM. In ODB, the electrical three-level drive signal is converted into one zero and one non-zero optical power level, with a phase modulation of 0 and π for the non-zero levels. In contrast to ODB, the IDB signal is not optimum in terms of signal-to-noise power ratio and reach, but it allows bandwidth-saving signal processing in the electrical part of the transmitter and receiver.

Using the same devices as for the 50 Gbit/s OOK transmission, IDB transmission is demonstrated at a line rate of 100 Gbit/s. After opto-electric conversion with a photodiode, the received signal is recorded with a real-time oscilloscope at a sampling rate of 160 GSa/s. The BER is measured off-line without any equalization on the receiver side. Figure 4.7 shows the eye diagrams generated from the recordings for a back-to-back measurement, Fig. 4.7(a), and for transmission over a 5 km fiber link, Fig. 4.7(b). For the back-to-back measurement, the BER as extracted from the recordings is 4.3×10^{-4}, which can be improved to 8.5×10^{-5} by using a gate field of 0.1 V/nm to increase the conductivity of the doped silicons slabs of the SOH MZM [81]. In the current design, the gate field of 0.1 V/nm is created by a voltage that is applied to the silicon substrate and drops across the well-isolating, thick buried oxide layer. This requires a high static voltage of 200 V to maintain the gate field. The gate voltage can be reduced by using dedicated gate electrodes [85] or may even be completely omitted by using optimized doping profiles, both of which were not available for our experiments. Note that the gate voltage is not associated with any measurable current flow and does hence not lead to additional power dissipation in the device. After transmission over 5 km, the measured BER is 1.6×10^{-3}, clearly below the hard-decision FEC threshold 4.4×10^{-3} for 7% overhead. The estimated energy consumption of the modulator is 190 fJ/bit, assuming that the electrical energy is dissipated in the terminating resistor (see Section 4.8). The signal-conditioning chip requires a power of 700 mW (incl. 4×25 Gbit/s multiplexer and 6-tap FFE) corresponding to 7 pJ/bit. Previously we showed that SOH modulators can be operated with peak-to-peak voltages well below 1 $\mathrm{V_{pp}}$ [100]. In a fully integrated package, the additional external drive amplifier can hence be omitted, and the total power consumption for the 100 Gbit/s transmitter will stay below 1 W. This is well compatible with the power ratings of highly compact SFP+ packages. Note that for our OOK and

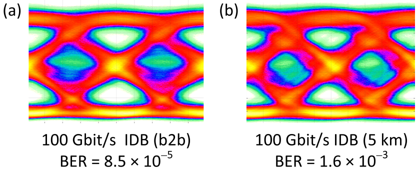

Fig. 4.7: Eye diagrams for 100 Gbit/s IDB signaling. The BER values stay below the FEC threshold 4.4×10^{-3} for 7% overhead. (a) Back-to-back (b2b) measurement (b) Transmission over a 5 km long dispersion-compensated fiber link.

IDB experiments, signal processing comprises low-pass filtering performed by an “analog” equalizer that is directly implemented into the signal-conditioning IC and does not require digital operations, leaving aside any coding and decoding. The processing effort and the associated power consumption are hence expected to be much reduced compared to coherent modulation formats.

4.6 Summary

Figure 4.8 recapitulates the BER for all performed experiments. Due to bandwidth and equipment limitations the BER increases with the line rate. PAM4 presents a viable method to push the line rate beyond 100 Gbit/s when powerful signal processing is available. In contrast to that, the simplicity of OOK and IDB modulation is attractive for integrated driver electronics that are subject to reasonable performance limitations. The excellent energy efficiency of SOH modulators and SiGe BiCMOS driver electronics holds promise for low cost and low power 100 G transmitters with small form factors. At 50 Gbit/s, error-free transmission could be demonstrated. No FEC is needed, which greatly simplifies the transceiver architectures. For 100 Gbit/s transmission using IDB modulation, the BER is below the threshold for hard-decision FEC with 7% overhead. The receiving circuit for IDB is comparatively simple and can be easily co-integrated with the modulator driver on a common transceiver chip [124]. Competing modulator concepts based on conventional pn-type silicon photonic devices, which are currently under development in the industry, struggle to fulfill the stringent requirements with respect to footprint and energy consumption that are associated with small formfactor pluggable (SFP) modules. In contrast to that, the results of our 100 Gbit/s IDB experiments

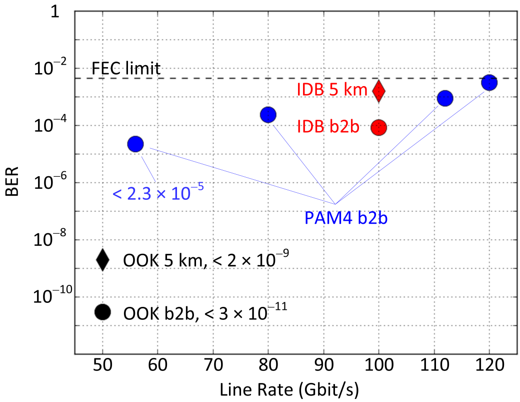

Fig. 4.8: Overview of all measured BER values for comparison. Dots represent the back-to-back (b2b) results for OOK (● black), PAM4 (● blue) and IDB (● red). For OOK and IDB the modulators were operated by a BiCMOS signal-conditioning IC and transmission over a 5 km dispersion compensated fiber link is shown (♦/♦ diamonds). Due to bandwidth limitations of the used components the BER increases with the data rate. All measured BER values stay below the threshold for FEC with 7% overhead. OOK at 50 Gbit/s is found to be error free.

indicate that SOH modulators could be operated by integrated driver chips and allow for IM/DD transmission with disruptive power consumption of less than 1 W. This represents an important step towards silicon photonic 100 Gbit/s and 400 Gbit/s transmitters compatible with SFP+ packages.

4.7 Comparison of IM/DD modulation formats

[This section was published as Appendix A of [J2]]

In this section we discuss three IM/DD modulation formats, namely non-return-to-zero on-off-keying (NRZ-OOK), 4-level pulse amplitude modulation (PAM4), and the duobinary (DB) format. We compare these modulation formats in terms of two main criteria: Spectral efficiency for a given bandwidth which is limited by optical and electronic components, and complexity of the required system, in particular the required electric circuitry and the bandwidth of the components, which has a direct impact on cost, scalability and energy consumption.

In the following discussion we consider rectangular non-return-to-zero (NRZ) pulses with identical peak signal level A. This signal can e.g. refer to a voltage, to a current, or to the envelope of an optical power or intensity. A random bit stream is encoded into a sequence of pulses with a maximum height A.

Figure 4.9(a) shows an exemplary waveform for OOK. The pulse duration T is given by the symbol rate $f_\mathrm{s} = 1/T$. Each symbol contains one bit of information, therefore the data rate f_d equals the symbol rate f_s. The spectrum of the random sequence of rectangular pulses is shown in Fig. 4.9(d) and is given by a sinc^2-function $\mathrm{sinc}^2(f/f_\mathrm{d})$. The first zero $f_\mathrm{d} = 1/T$ of the power spectrum defines the bandwidth $B = f_\mathrm{d}$ for the OOK signal. The level spacing of the signal equals A. The components at the receiver and transmitter side can be very simple as only binary signals are used. However, these components need to operate at high symbol rates, and therefore require a bandwidth in the order of f_d.

To relax bandwidth requirements, one can use multilevel signaling such as PAM4 where four signal levels are used to encode two bit into each symbol. Figure 4.9(b) shows the waveform of the same bit stream as in Fig. 4.9(a), now encoded with four signal levels 0, $A/3$, $2A/3$ and A, using Gray coding to map bit pairs into signal levels. For the same data rate f_d as with OOK, the symbol rate is now reduced by a factor of two. Because the pulse width doubles, the bandwidth of the $\mathrm{sinc}^2(f/(f_\mathrm{d}/2)$ decreases to $B = f_\mathrm{d}/2$ (see Fig. 4.9(d)). However, the level spacing reduces by a factor of three and leads to a smaller eye-opening and more stringent signal-to-noise-ratio (SNR) requirements. While for PAM4 the electronics operates at half the OOK speed, the circuitry becomes significantly more complicated. On the transmitter side, binary inputs have to be converted into a four-level signal requiring a more complex equalizer and a linear driver. On the receiver side, three level slicers and a multi-level clock-and-data-recovery have to convert the signal back into a binary data stream.

An alternative approach to narrow down the spectrum without decreasing the symbol rate is the use of partial response (PR) signaling. In PR signaling schemes, the data to be transmitted are distributed over multiple symbols [146]. A particularly interesting PR format is duobinary modulation (DB) as presented

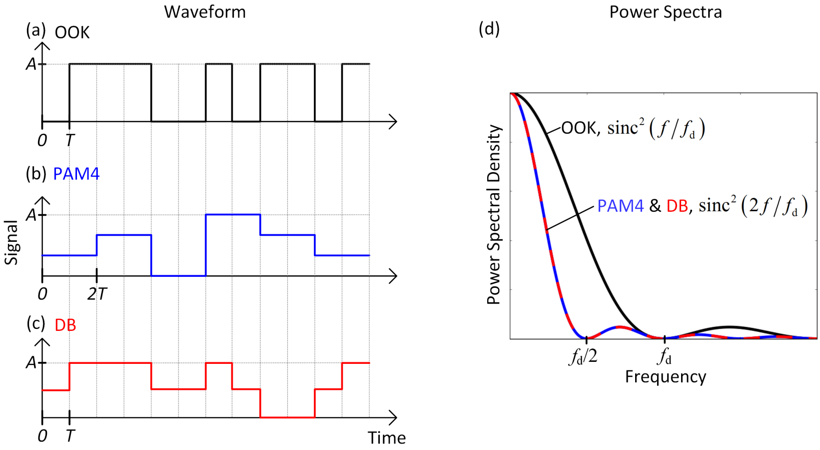

Fig. 4.9: Comparison of non-return-to-zero (NRZ) modulation formats and associated power spectra of random pulse sequences with a fixed data rate f_d. Because rectangular pulses are assumed, all spectra have a sinc^2-shape. Discrete spectral lines are disregarded. (a) Non-return-to-zero on-off keying (NRZ-OOK), (b) 4-level pulse amplitude modulation (PAM4), and (c) three level duobinary (DB), assuming rectangular pulse shapes and identical peak levels A. While OOK and DB operate at the same symbol rate $f_\mathrm{S} = 1/T$, PAM4 encodes two bit per symbol so that the symbol rate can be halved, $f_\mathrm{S} = 1/(2T)$. Duobinary signaling works with three signal levels and a (precoded) binary bit stream is encoded with a, e.g., delay-and-add-circuit. Therefore, starting from rectangular NRZ pulses the DB correlation time is doubled as compared to OOK, and the bandwidth is halved. Since for the same average power the distance between neighboring PAM4 and DB levels is reduced as compared to OOK, the noise tolerance is reduced.

by Lender [147] and Sekey [148]. This format operates at the full OOK symbol rate but encodes one bit per symbol into three levels. A logical “0” is represented by the middle level; and a logical “1” is represented by either the upper or the lower level, depending on the number of logical “0” between two logical “1” [147]: If a logical “1” is represented by an upper (lower) level and an odd number of logical “0” follows, then the next logical “1” is represented by the lower (upper) level. If the number of logical “0” between two logical “1” is even, then the subsequent logical “1” is represented by the previous “1” level. The procedure introduces a correlation between two consecutive symbols, and for a random sequence, the correlation time $2T$ is doubled as compared to OOK with a correlation time of T. The power spectrum of a random data sequence is again a sinc^2-function, but with a bandwidth $B = f_\mathrm{d}/2$ [148]. This statement holds for rectangular symbols. The DB spectrum shown in Fig.4.9(d) is identical with the PAM4 spectrum of the PAM4 signal at the same data rate.

The DB coding can be realized by a pre-coded binary bit stream and a simple delay-and-add circuit, or by a low-pass filter with a bandwidth that resembles the same frequency response as the delay-and-add circuit [146, 149]. Duobinary coding is easy to implement, and even the low-pass characteristic of the transmission channel itself can be used to convert a (precoded) OOK signal into a DB format [149]. Thus, the advantage of a reduced transmission bandwidth does not come at the cost of complicated electronics as with PAM4. At the transmitter, the natural frequency roll-off, often combined with an equalizer can be used to generate the DB signal from an OOK signal. At the receiver two slicers and an XOR-circuit are sufficient to recover the binary data stream [146]. The DB level spacing is $A/2$ and therefore DB is less noise tolerant than OOK, but more resilient than PAM4.

A special case of DB often employed in optical transmission systems is most commonly referred to as optical duobinary (ODB). In ODB, the three levels in the electrical signal are modulated onto an optical carrier such that the optical signal has two intensity levels like OOK, but an additional phase modulation. This gives an advantage in SNR but restricts the bandwidth saving effect of DB to the transmitter. In contrast to that, our experiment relies on three signal levels that are represented by three optical intensities, and we refer to the scheme as intensity-modulated duobinary. We feel that this nomenclature is more precise than the often used naming electrical duobinary (EDB). Intensity-modulated duobinary is advantageous because the electro-optic modulator requires only half the drive voltage swing than with ODB, and because electronic bandwidth requirements are relaxed both at the transmitter and at the receiver side.

As an alternative to the presented modulation formats, it is possible to exploit multicarrier formats such as discrete multitone transmission, also known as orthogonal frequency multiplexing, in an IM/DD transmission scheme [150]. While the spectral efficiency would be better, these schemes require high-speed DACs, ADCs and DSP, which are associated with significant power consumption and technical complexity. Such schemes and are not considered in our work, which focuses on cost and power-efficient solutions for short reach optical interconnects.

Table 4.1: Comparison of OOK, PAM4 and IDB modulation formats

Modulation Format	Pros	Cons
OOK	• Simple modulator drive electronics • Simple receiver architecture (1 slicer) • Large eye opening	• Demanding bandwidth requirement for electronics
PAM4	• Reduced bandwidth requirements • Operation at half the OOK symbol rate	• Complex drive and receiver electronics (3 slicers) • Reduced eye opening (1/3 of OOK)
IDB	• Reduced bandwidth requirement • Simple drive and receiver electronics	• Operation at full OOK symbol rate • Reduced eye opening (1/2 of OOK)

Table 4.1 summarizes the key advantages and disadvantages of OOK, PAM4 and IDB. We show that SOH modulators are suited for all three formats.

To get a more quantitative idea about the SNR tolerance of the three modulation formats we estimate the BER of a rectangular NRZ signal. To this end, we consider the voltage after detection with a photodiode. The lowest signal voltage is 0 and the highest voltage is A as depicted in Fig. 4.9. We assume equidistant signal levels, and Gray coding for the case of PAM4. The decision thresholds are placed in the center between two adjacent levels. Further, we assume additive white Gaussian noise with an average electrical power $P = \sigma^2$ equal to the noise variance σ^2 for all signal levels. The following BER result:

$$\mathrm{BER}_{\mathrm{OOK}} = \frac{1}{2}\mathrm{erfc}\left(\frac{A}{2\sqrt{2}\sigma}\right), \tag{4.2}$$

$$\begin{aligned}\mathrm{BER_{PAM4}} &= \frac{3}{8}\mathrm{erfc}\left(\frac{A}{6\sqrt{2}\sigma}\right) + \frac{1}{4}\mathrm{erfc}\left(\frac{3A}{6\sqrt{2}\sigma}\right) - \frac{1}{8}\mathrm{erfc}\left(\frac{5A}{6\sqrt{2}\sigma}\right) \\ &\approx \frac{3}{8}\mathrm{erfc}\left(\frac{A}{6\sqrt{2}\sigma}\right),\end{aligned} \tag{4.3}$$

$$\mathrm{BER_{IDB}} = \frac{3}{4}\mathrm{erfc}\left(\frac{A}{4\sqrt{2}\sigma}\right) - \frac{1}{4}\mathrm{erfc}\left(\frac{3A}{4\sqrt{2}\sigma}\right) \approx \frac{3}{4}\mathrm{erfc}\left(\frac{A}{4\sqrt{2}\sigma}\right). \tag{4.4}$$

The complementary error function is defined by $\mathrm{erfc} = (2/\sqrt{\pi})\int_z^\infty \exp(-t^2)\mathrm{d}t$. We compare these modulation formats for identical optical average powers which happen to result in identical optical peak powers and therefore identical electrical peak powers A^2. However, the average electrical signal power measured after the photodiode differ,

$$P_{\mathrm{S,OOK}} = \frac{A^2}{2}, \qquad P_{\mathrm{S,PAM4}} = \frac{7A^2}{18}, \qquad P_{\mathrm{S,IDB}} = \frac{3A^2}{8}. \tag{4.5}$$

We define the electrical signal-to-noise power ratio by $\mathrm{SNR} = \mathrm{P_S}/\mathrm{P_N}$. Figure 4.10 shows a plot of the BER as a function of the SNR. The modulation format with the widest level spacing (OOK, level spacing = A) is most tolerant to noise. As the signal spacing is reduced for IDB (level spacing= $A/2$) and for PAM4 (level spacing= $A/3$), the probability to receive erroneous bits increases, and the BER for a given SNR becomes larger.

4.8 Power consumption of SOH modulators

[This section was published as Appendix B of [J2]]

To estimate the power consumption of the SOH modulator, we assume that the traveling-wave electrodes are represented by ideal transmission lines which are perfectly matched at both ends. The terminating AC-coupled load resistance is R. The applied drive voltage drops across the terminating resistor, and the

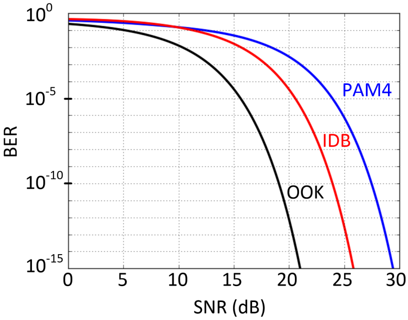

Fig. 4.10: Bit error ratio (BER) calculated by Eq. 4.2, 4.3, and 4.4 for the modulation formats on-off-keying (OOK), four-level pulse-amplitude modulation (PAM4), and intensity-modulated duobinary (IDB) signaling as a function of the electrical signal-to-noise-ratio (SNR). Equal electrical peak powers are assumed, leading to the best noise tolerance for two level OOK. The level spacing becomes smaller for IDB (three signal levels) and PAM4 (four signal levels), and the noise tolerance worsens. For PAM4 we use Gray coding.

modulation signal power is entirely dissipated in the load. The modulator bias voltage fixes the MZM operating point at the quadrature point and is irrelevant for energy considerations because of the AC-coupling of the terminating resistor R. The drive voltage supplied by the amplifier was either directly measured or estimated from the specifications of the amplifier. This estimation of the energy consumption takes only account of the energy dissipated in the modulator's terminating resistor.

For OOK with a data rate r_{OOK}, with binary rectangular signals, equiprobable "ones" and "zeros", and for a DC-free electrical drive signal with a peak-to-peak voltage swing U_{d}, we write for the energy dissipated per bit

$$W_{\text{bit,OOK}} = \frac{(U_{\text{d}}/2)^2}{50\,\Omega}\frac{1}{r_{\text{OOK}}}. \tag{4.6}$$

The 3-level signal for intensity-modulated duobinary is made up from a state with $U = 0$, corresponding to a representation of a "zero" of the binary signal

Table 4.2: Overview of modulator data for three experiments. A DC voltage in the range 0 V...U_π for setting the operating point was applied in all measurements.

Line Rate	Modulation Format	Modulator Length	π-Voltage	Peak-to-Peak Voltage	Energy/bit
50 Gbit/s	OOK	1.1 mm	1.2 V	2.7 $\mathrm{V_{pp}}$	730 fJ/bit
100 Gbit/s	IDB	1.1 mm	1.2 V	2.8 $\mathrm{V_{pp}}$	190 fJ/bit
120 Gbit/s	PAM4	0.5 mm	2.2 V	2.1 $\mathrm{V_{pp}}$	100 fJ/bit

and $U = \pm U_\mathrm{d}/2$ representing a “one”. For the energy dissipated per bit we therefore find the expression

$$W_\mathrm{bit,IDB} = \frac{1}{2}\frac{(U_\mathrm{d}/2)^2}{50\,\Omega}\frac{1}{r_\mathrm{IDB}}. \tag{4.7}$$

The 4-level PAM4 signal consists of the equiprobable states $U = \pm U_\mathrm{d}/2$ and $U = \pm U_\mathrm{d}/6$. The energy consumption per bit is

$$W_\mathrm{bit,PAM4} = \frac{1}{2}\left[\frac{(U_\mathrm{d}/2)^2}{50\,\Omega} + \frac{(U_\mathrm{d}/6)^2}{50\,\Omega}\right]\frac{1}{r_\mathrm{PAM4}}. \tag{4.8}$$

Table 4.2 gives a summary of the modulator data for the various experiments including the energy consumption per bit.

[End of paper [J2]]

5 Packaging of SOH modulators

This chapter reports on electrical packaging of SOH modulators and was published in a scientific journal [J3]. The material from the publication was adapted to comply with the layout and structure of this thesis.

[Beginning of Paper [J3]. Reprinted with permission ©The Optical Society.]

Electrically packaged silicon-organic hybrid (SOH) I/Q-modulator for 64 GBd operation

Optics Express, Vol. 26, Issue 26, pp. 34580-34591 (2018)

DOI: `https://doi.org/10.1364/OE.26.034580`

Heiner Zwickel,[1] Juned N. Kemal,[1] Clemens Kieninger,[1,2]
Yasar Kutuvantavida,[1,2] Jonas Rittershofer,[1] Matthias Lauermann,[1,3]
Wolfgang Freude,[1] Sebastian Randel,[1] and Christian Koos[1,2]

[1] Institute of Photonics and Quantum Electronics (IPQ), Karlsruhe Institute of Technology (KIT), Germany

[2] Institute of Microstructure Technology (IMT), Karlsruhe Institute of Technology (KIT), Germany

[3] Now with Vanguard Photonics GmbH, Karlsruhe, Germany

Silicon-organic hybrid (SOH) electro-optic (EO) modulators combine small footprint with low operating voltage and hence low power dissipation, thus lending themselves to on-chip integration of large-scale device arrays. Here we demonstrate an electrical packaging concept that enables high-density radio frequency (RF) interfaces between on-chip SOH devices and external circuits. The concept combines high-resolution Al_2O_3 printed-circuit boards with technically simple metal wire bonds and is amenable to packaging of device arrays with small on-chip bond pad pitches. In a set of experiments, we characterize the performance of the underlying RF building blocks and we demonstrate the

viability of the overall concept by generation of high-speed optical communication signals. Achieving line rates (symbols rates) of 128 Gbit/s (64 GBd) using quadrature-phase-shift-keying (QPSK) modulation and of 160 Gbit/s (40 GBd) using 16-state quadrature amplitude modulation (16QAM), we believe that our demonstration represents an important step in bringing SOH modulators from proof-of-concept experiments to deployment in commercial environments.

5.1 Introduction

Efficient broadband EO modulators are key components in microwave photonics and in optical communication systems. Over the last decade, the footprint of EO modulators has been radically reduced, moving from centimeter-long $LiNbO_3$-devices to millimeter- or sub-millimeter components that exploit high-index-contrast waveguides on semiconductor substrates [40–42, 151]. In this context SiP has emerged as a particularly promising platform, exploiting advanced CMOS processes for high-yield mass production of modulators – either as standalone devices or as parts of more complex PICs [15,23–25]. To improve the performance of SiP modulators, silicon nanowire waveguides can be combined with highly efficient organic EO materials that have been engineered on a molecular level [48, 49]. This so-called silicon-organic hybrid (SOH) approach allows to reduce the voltage-length product of EO modulators to 0.32 Vmm [18] – more than an order of magnitude below that of conventional depletion-type SiP modulators. SOH integration allows to realize high-speed modulators with sub-millimeter device lengths. The modulators offer line rates up to 120 Gbit/s for IM/DD [86], and up to 400 Gbit/s for coherent 16QAM signaling [93].

However, while reducing the on-chip footprint of EO modulators increases integration density as well as modulation speed, electrical packaging of the devices becomes increasingly difficult [152]. One of the main problems is the vast size mismatch between the ultra-fine features that can be realized by advanced deep-UV lithography on the silicon chip and the much larger dimensions of RF traces that are commonly available on printed circuit boards (PCBs) or interposers. This often results in a mismatch of bond pad pitch, which impedes high-density packaging of large-scale device arrays and must be overcome by excessively long metal wire bonds with limited performance in terms of bandwidth and signal fidelity [153]. In the field of microelectronics, flip-chip bonding is often used for broadband connections between interposers and densely integrated on-chip circuits [154]. This approach has been recently transferred to packaging of advanced SiP transceivers [155–157], enabling transmission of optical signals with data rates of up to 136 Gbit/s using 16QAM signaling at a symbol rate of 34 GBd [157]. However, flip-chip bonding of PICs blocks access to the chip surface and thus complicates optical packaging, often leaving edge coupling to actively aligned optical fibers as the only option [158]. Moreover, flip-chip bonding of photonic devices often requires dedicated processes that need to be adapted to specific optical components in terms of thermal budget or with respect to the deployed flux chemicals [153, 159]. In contrast to flip-chip bonding, accessing high-density PIC by metallic wire bonds leaves the top surface of the chip free and thus offers high flexibility with respect to optical packaging [79, 160–167], exploiting, e.g., highly efficient SiP grating couplers [168], photonic wire bonds [169], or facet-attached micro-lenses [170]. However, published signaling demonstrations using SiP modulators accessed by metal wire bonds have so far been limited to symbol rates of 28 GBd. Moreover, none of the aforementioned approaches have so far been applied to SOH devices.

In this paper, we demonstrate an electrically packaged SOH EO modulator that exploits simple metal wirebonds in combination with a high-resolution ceramic PCB to establish broadband connections from standard coaxial connectors to sub-mm on-chip devices. Our approach allows to adapt the bond-pad pitch on the PCB to that of the PIC, thereby permitting connections through short parallel metal wire bonds that are amenable to broadband packaging of large-scale device arrays. In a set of experiments, we expand upon our earlier work [171] and demonstrate line rates (symbols rates) of 128 Gbit/s (64 GBd) using QPSK modulation, and line rates (symbol rates) of 160 Gbit/s (40 GBd) using 16QAM. This is among the highest symbol and line rates demonstrated so far with electrically packaged SiP modulators. In addition, our devices feature a voltage-length product of only $U_\pi L = 0.9\,\mathrm{Vmm}$, which is well below that of packaged SiP devices that were previously demonstrated. When combined with recent progress in improving thermal stability of organic EO materials [60] and of SOH modulators [20] as well as with novel technologies for hybrid photonic integration [172], we believe that our demonstration represents an important step in bringing SOH modulators from proof-of-concept experiments to deployment in laboratory and commercial environments.

5.2 Concept, fabrication, and assembly

This section introduces the concept of SOH modulators, reports on the fabrication and characterization of the high-frequency PCBs, and shows the assembly of the electrically packaged modulator.

5.2.1 SOH Mach-Zehnder modulator

The concept of a strip-loaded SOH MZM [49–51] is depicted in Fig. 5.1. The basic optical waveguide structure is fabricated on a standard 220 nm SOI wafer using 248 nm deep-UV lithography. The MZM consists of two parallel 0.6 mm-long phase shifter sections. Each phase shifter comprises a silicon slot waveguide filled with an EO organic material. The slot has a width of 120 nm. The 240 nm-wide Si rails of the slot waveguide are connected to the electrodes with thin, doped Si slabs and Al vias. The device is realized as traveling-wave modulator where the optical mode in the slot waveguide co-propagates with the electric (modulating) mode. Both phase shifter sections share the central signal electrode which, together with the outer ground electrodes, form a coplanar ground-signal-ground transmission line. Aluminum vias connect the electrodes to bond pads of the top metal layer at both ends of the transmission line. The electrical RF voltage drops mainly across the narrow slot where the light is highly confined, thus leading to a high overlap of the modulating electric field and the optical mode and a high modulation efficiency. As an EO material, we use the guest-host material SEO250, which is locally deposited on the slot waveguides by a high-resolution dispensing technique. To activate the macroscopic $\chi^{(2)}$-nonlinearity, the microscopic molecular dipole moments of chromophores in the organic EO material need to be aligned in a one-time poling process. To this end, a poling voltage U_pol is applied across the (floating) ground electrodes at an elevated temperature for aligning the EO chromophores. After cooling the device down, the poling voltage is removed, and the molecular orientation is frozen as indicated by the green arrows in Fig. 5.1 (e-3). The modulating field E_mod induced by the RF drive voltage is oriented parallel to the chromophore alignment in one arm of the MZM and antiparallel in the other arm, which leads to chirp-free push-pull operation. The PIC used in this work contains an array of MZMs that are configured as nested pairs to serve as IQ-modulators. Alternatively, the unused ports of the

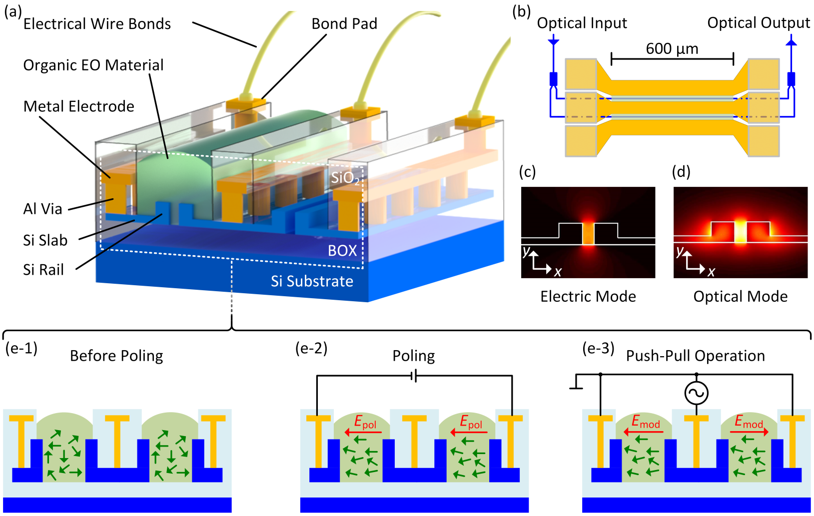

Fig. 5.1: Device concept and operation of an SOH Mach-Zehnder modulator (MZM). (a) Artist's view of the MZM: The organic electro-optic (EO) cladding (green) is shown in one arm only. Aluminum vias connect the doped thin Si slabs to the traveling-wave electrodes and to the bond pads on the top metal layer. (b) Schematic of traveling-wave MZM with electrodes that form a ground-signal-ground coplanar transmission line having bond pads at both ends. (c, d) Color plot of the dominant x-component of the RF electric field and the optical electric field. The strong overlap leads to efficient modulation. (e-1) to (e-3): Poling of the modulator. (e-1) Prior to poling, the molecular dipoles (green arrows) in the organic EO material are randomly oriented such that no macroscopic Pockels effect can be observed. (e-2) At elevated temperatures, a poling voltage induces a poling field E_{pol} which aligns the molecular dipoles predominantly along the electric field. This molecular orientation is frozen when the material is cooled down to room temperature. (e-3) In push-pull operation, the modulating RF voltage is applied to the center signal electrode thereby leading to a modulating field E_{mod} that is oriented parallel to the poling direction in one arm and anti-parallel in the other one. This allows for pure amplitude or intensity modulation without residual phase modulation (chirp-free) [86].

MZM can be accessed directly via attached grating couplers, which allows to use the devices individually for amplitude or intensity modulation.

5.2.2 High-frequency PCB

The PCB traces are realized as 50 Ω coplanar ground-signal-ground (GSG) transmission line (TL). To facilitate electrical board-to-chip connections with short wire bonds and to enable the integration of densely spaced modulator arrays, the spacing of the board-level RF traces must be matched to the pitch of the bond pads on the silicon chip, which is chosen to be 100 µm to save chip area while enabling reliable placement of metal wire bonds. At the same time, the board-level RF traces must allow for easy interfacing to discrete devices such as coaxial connectors or surface mount devices (SMDs), which feature millimeter-size contact spacing. To this end, we use tapered sections of RF traces with impedance-matched transitions between RF traces of different dimensions. Fabrication of the underlying PCB requires structuring techniques that combine micrometer resolution with the ability to process boards with centimeter-scale overall dimensions. To this end, we have developed a direct-laser write (DLW) fabrication process which allows for flexible mask-less fabrication at low cost. The process starts from square 100×100 mm^2 Al_2O_3 ceramic substrates which are covered by a 3 µm-thick electroplated Au layer. The substrates are coated with a positive-tone photoresist (AZ1500) and patterned with a Nd:YAG laser. After development of the exposed structures, the Au layer is wet-etched using a KI solution, and the resist mask is removed.

The performance of the RF building blocks is characterized using dedicated test structures. Figure 5.2(a) shows the TL near the chip edge, Fig. 5.2(b) displays the taper section, and Fig. 5.2(c) illustrates the TL near a coaxial connector. For the characterization, the TL as used near the chip edge is contacted on both sides using GSG microwave probes, and the S-parameters are measured using a VNA. The reference planes are moved to the probe tips by using a short/open/load/through (SOLT) calibration routine with a proper calibration substrate. Using the method described in [173], we extract the characteristic impedance Z_0 and the power loss coefficient a from the measured S-parameters, Fig. 5.2(d). The characteristic impedance Z_0 is well matched to the system impedance of 50 Ω over the entire measurement range. The power loss coefficient a, presumably dominated by conductor loss, increases with frequency due to the skin effect, but stays below 2 dB/cm, which compares well to the losses achieved on state-of-the-art calibration substrates [174]. The characteristic impedance and the power loss coefficient shown in Fig. 5.2(d)

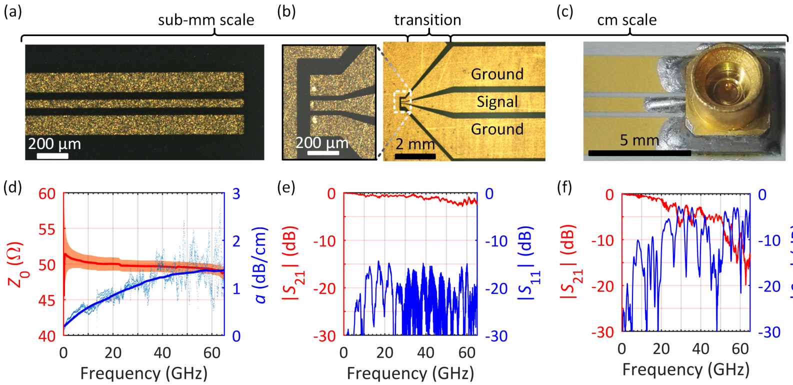

Fig. 5.2: Characterization of the RF building blocks. (a) Micrograph of a coplanar TL with dimensions matching the bond pads on the Si chip. The TL has been fabricated on gold-plated ceramic substrates using direct laser writing and wet etching. (b) Micrograph of a tapered section of the TL. The left-hand side corresponds to the TL shown in (a), the right-hand side matches the TL shown in (c). (c) Test structure to characterize the transition from a surface-mounted coaxial connectors to a TL. (d) Characteristic impedance Z_0 (dark red: mean value from a set of 10 measurements, light red: corresponding standard deviation) and power propagation loss a (light blue dots: measurement data; blue line: moving average as a guide to the eye) extracted from S-parameters of TL with the small cross-section shown in (a). The characteristic impedance Z_0 is well matched to 50 Ω, and the losses stay below 2 dB/cm. (e) S-parameters of a test structure comprising a 9 mm-long TL with large cross section as shown in (c), terminated by a pair of tapers as shown in (b). The measurements exhibit the high transmission and reflection quality of the tapers. (f) S-parameters obtained from a test structure comprising a 7.8 mm-long TL terminated by a pair of coaxial SMP-M connectors as shown in (c). The measurement also comprised the influence of two semi-flexible cable assemblies converting from the 1.85 mm VNA connectors to the SMP-M interface.

were extracted from a set of 10 different TL, all of which yield comparable results.

The transition between TL of different cross sections is realized by an impedance-matched linear taper. Figure 5.2(e) shows the measured S-parameters of the corresponding test structure comprising two tapers at both sides of a 9 mm-long TL section as in Fig. 5.2(b). The 3 dB bandwidth extracted from S_{21} is larger than 60 GHz, and the reflection as expressed by S_{11} stays below −15 dB.

To feed the signal from coaxial cables to the PCB, surface-mounted coaxial connectors are soldered to appropriate pads connected to the centimeter-scale transmission line. Measured S-parameters of a structure comprising two such connectors (surface-mounted type SMP-M) at the ends of a 7.8 mm-long TL indicate good performance up to 20 GHz. However, the increase of the power reflections limits the performance in the 25...40 GHz range, see Fig. 5.2(f). The reduction in transmitted power beyond 25 GHz is attributed to losses in the coaxial connectors and the transition to the on-board pads. Note that our measurements with SMP-M connectors include the influence of two semi-flexible cable assemblies converting from 1.85 mm VNA connectors to the SMP-M interface, which we could not isolate because we lack an SMP-M calibration kit. These assemblies are specified to have a 3 dB bandwidth > 65 GHz such that we do not expect any significant distortions of our measurements.

5.2.3 Assembly

Figure 5.3 shows the module assembly. The SiP chip is glued on a metal sub-mount using a conductive epoxy adhesive, Fig. 5.3. After poling the modulators, two identical ceramic PCB are placed on both sides of the Si chip and are glued to the same metallic sub-mount (see Fig. 5.3(a) and Fig. 5.3(c)). By precise machining of the sub-mount, the surfaces of the Si chip and the PCB are brought to approximately the same height to allow for short wire bonds. To avoid excitation of unwanted substrate modes, the sub-mount features a void below the RF traces, see Fig. 5.3. The traveling-wave electrodes of the modulators are connected to the PCB traces at both ends using Au wires attached by wedge-to-wedge bonding. Wedge bonding was chosen because the wire lengths can be kept shorter than with ball bonding. A short bondwire connection is desirable for high-frequency operation. Surface-mounted GPPO-compatible SMP-M receptacles and coaxial cables are used to connect to the signal source at one end of the transmission line and to a terminating resistor at the other end. The module contains two MZMs that can be used either individually for amplitude or intensity modulation, or, by using a different optical input/output, as two nested MZMs which form an IQ-modulator. Figure 5.3(c) shows an image of the module, and Fig. 5.3(d) displays a micrograph of the bonded chip. Light is coupled to and received from the chip using on-chip grating couplers.

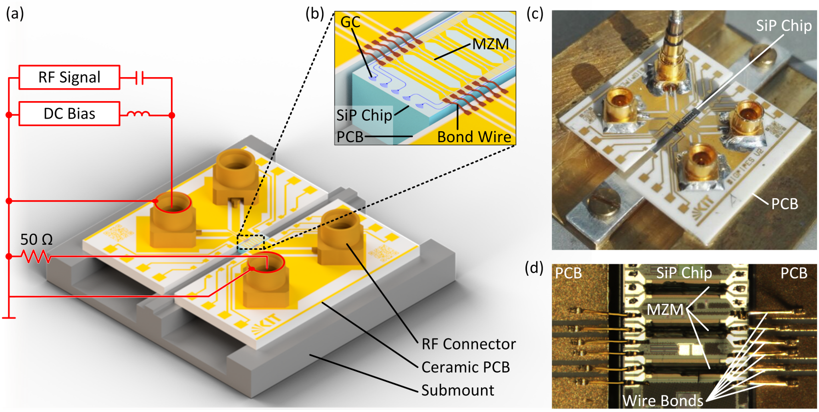

Fig. 5.3: Electrical packaging. (a) Artist's view of the module connecting two SOH MZMs to surface-mounted SMP-M connectors on a ceramic PCB. The external electrical circuit used for experiments is depicted schematically in red for one of the MZMs (b) Two MZMs, connected by bond wires. (c) Image of the complete module. (d) Micrograph of the SiP chip. Wire bonds are used for connecting the chip to the traces on the two ceramic PCBs.

5.3 Optical, DC, and small-signal characterization of module

To measure the optical transmission spectrum of the electrically packaged MZM, we use a tunable laser. The static extinction ratio of the modulator exceeds 30 dB. The fiber-to-fiber insertion loss is 11.6 dB. This includes overall fiber-chip coupling losses of 8.9 dB caused by the two grating couplers, as well as an on-chip device loss of 1.3 dB, caused by passive components, namely two MMI splitters (0.37 dB each), input/output access waveguides (0.2 dB in total), and mode converters at the strip-slot waveguide interface (0.4 dB in total). The remaining 1.4 dB are attributed to slot waveguide loss in the phase shifter sections, which leads to an estimated propagation loss of $a = 2.3$ dB/mm. The π-voltage U_π of the MZM is measured by applying a low-frequency (< 1 kHz) electrical signal, and by recording the applied voltage and the transmitted optical power using an oscilloscope. The π-voltage U_π corresponds to the voltage that needs to be applied to the center electrode of the MZM in the low-frequency limit to induce a relative phase shift of π between the two arms of the device. We find $U_\pi = 1.5\,\mathrm{V}$, leading to a modulation efficiency of the 0.6 mm-long MZM of $U_\pi L = 0.9\,\mathrm{Vmm}$ and a π-voltage-loss product $aU_\pi L = 2.1\,\mathrm{dBV}$ – the best value so far achieved in SOH modulators using an EO material with a high glass transition temperature T_g. Note that this π-voltage-loss product is significantly smaller than the best value achieved in high-speed depletion-type SiP modulators, which amounts to 12 dBV [72]. The low $U_\pi L$-product of the SOH modulator results from the high EO activity of the organic cladding material in combination with the slot-waveguide geometry of the phase shifter [49], which leads to a good overlap of the optical mode and the modulating RF field. To improve the EO modulation bandwidth of the MZM, the conductivity of the doped silicon slabs can be increased by a gate voltage applied between the ground electrode and the Si substrate [81]. This leads to an accumulation layer of electrons at the interface of the doped Si slabs and the buried oxide, thereby increasing the slab conductivity. In the experiment, we use a gate field strength of 50 V/µm, which increases the loss of the slot waveguide only moderately by 0.2 dB. This setting was used for the dynamic analysis shown below, and for the data generation (Section 5.4). Note that the gate voltage can be reduced by using a gate electrode [85] or even omitted by using optimized doping profiles. The dynamic behavior of the MZM is characterized for the small-signal case using a VNA. First, the electrical S-parameters of the unpackaged MZM are measured using microwave probes at both ends of the modulator's coplanar TL. The result is shown in Fig. 5.4(a) along with the S-parameters of the electrically packaged modulator, which were measured by connecting the VNA ports directly to the SMP-M connectors on the ceramic PCB. The package has a significant influence on the electrical transmission spectrum at frequencies larger than 20 GHz. This is in agreement with the finding from Fig. 5.2(f), where a drop of the transmission in the transition to the surface-mounted connectors limits the performance beyond 20 GHz. In the low-frequency range, no significant impact on the EO performance is expected. This is confirmed by a second experiment, in which the electro-optic-electric (EOE) bandwidth is measured using a VNA and a calibrated photodiode. Figure5.4(b) shows the EOE responses of the electrically packaged and unpackaged MZM. As expected, the EOE responses are comparable up to a frequency of 20 GHz, with a rather modest frequency roll-off beyond that frequency. There is even a slight improvement of the frequency roll-off in the low-frequency range for the packaged MZM with respect to the unpackaged device. This observation is attributed to resonant

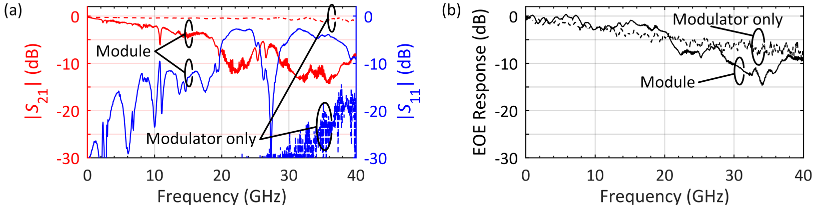

Fig. 5.4: Small-signal characterization of the MZM module. (a) Electrical S-parameters of the unpackaged modulator measured with microwave probes (dashed line), and of the electrically packaged modulator measured by connecting the VNA ports directly to the SMP-M connectors on the ceramic PCB (solid lines). (b) Electro-optical-electrical EOE bandwidth of the unpackaged modulator (dashed line), and of the electrically packaged modulator (solid line). Both S-parameters traces are normalized to the respective value measured at 40 MHz. At frequencies beyond 20 GHz, a slight roll-off is observed for the packaged device with respect to the unpacked device. The electro-optic 3 dB (6 dB) bandwidth for the electrically packaged modulator is 21 GHz (31 GHz). [*Note: The 3 dB EO bandwidth defined here corresponds to the 6 dB EOE bandwidth defined in Section 3.2 as* $f_{6\mathrm{dB,EOE}}$.]

peaking caused by imperfect impedance matching. The electro-optic 3 dB (6 dB) bandwidth for the electrically packaged modulator is 21 GHz (31 GHz). At frequencies between 20 GHz and 30 GHz, only a slight roll-off is observed for the packaged device with respect to the unpacked device. Beyond 30 GHz, the roll-off of the packaged device is more pronounced, thus limiting the achievable symbol rates in comparison to earlier transmission demonstrations that were performed with unpackaged devices contacted by high-frequency microwave probes.

Note that the response of the Pockels-type EO material in the modulator is ultra-fast and would in principle allow for THz modulation bandwidths. In real SOH devices, however, the speed is limited by the capacitance of the slot waveguide that needs to be charged and discharged via the resistive doped silicon slabs [49]. This effect can be mitigated by an improved doping profile for the silicon slabs, which reduces the resistivity and the associated RC time constant and therefore improves the bandwidth of the modulator without an undue increase of the optical loss. In addition, we may improve the bandwidth of the packaged module by using a more elaborate design of the critical transition between the coaxial connector and the coplanar transmission line on the PCB. Note that, besides the EOE bandwidth itself, the characteristic of the transfer function beyond the corner frequency is also important. As an example, a modulator with a bandwidth of 25 GHz but with a moderate roll-off can easily support a 100 Gbit/s OOK modulation [99].

5.4 Intensity-modulated and coherent signaling

Using a single MZM, intensity-modulated signals are generated in a first set of experiments. Four channels of a pulse pattern generator (PPG) are serialized in an electrical 4×1 multiplexer (MUX) to generate a PRBS with a length of $2^{31} - 1$. The output of the MUX delivers a voltage swing of $2\,V_{pp}$ and is directly connected to the input of the module. Light is coupled to the device using grating couplers. After the modulator, the optical signal is amplified by an EDFA. Out-of-band ASE noise is removed using an optical band-pass filter. The signal is detected using a photodiode connected to an equivalent-time sampling oscilloscope (Agilent 86100C), exploiting the repetitive nature of the test pattern for broadband electrical acquisition. Recorded eye diagrams at 20 Gbit/s and 40 Gbit/s are shown in Fig. 5.5(a) and Fig. 5.5(b), respectively. At 20 Gbit/s (40 Gbit/s) the measured Q-factor amounts to 9.8 (4.1). Neglecting inter-symbol interference (ISI) and assuming additive Gaussian noise as the only signal distortion, a BER of $\mathrm{BER_e} = 5.6 \times 10^{-23}$ at 20 Gbit/s is estimated [175], and a $\mathrm{BER_e} = 2.1 \times 10^{-5}$ at 40 Gbit/s. Note that the underlying assumptions might not hold exactly, especially at 40 Gbit/s where ISI might start to play a role. Still, without claiming exact quantitative accuracy of the estimated $\mathrm{BER_e}$ values, we are confident that the true BER falls well below the FEC threshold of 4.40×10^{-3} for less than 7% overhead [176].

In a second set of experiments, an arbitrary waveform generator (AWG, Keysight M8196A) replaces the PPG, and a real-time sampling oscilloscope (Keysight DSO-X 93204A) replaces the equivalent-time sampling oscilloscope of the previous experiment. In a first step, we generate intensity-modulated two- and multilevel signals, record the received data, and apply DSP for equalization and analysis of the received signal. The AWG generates a PRBS with a length of $2^{15} - 1$. The resulting pulses are shaped to have a root-raised cosine spectrum. Figure 5.5(c) shows the eye diagram of a 40 Gbit/s OOK signal, generated with a roll-off factor $\beta^{(\mathrm{ro})} = 1$, after applying an adaptive equalizer to flatten out the end-to-end frequency response of the system using an over-

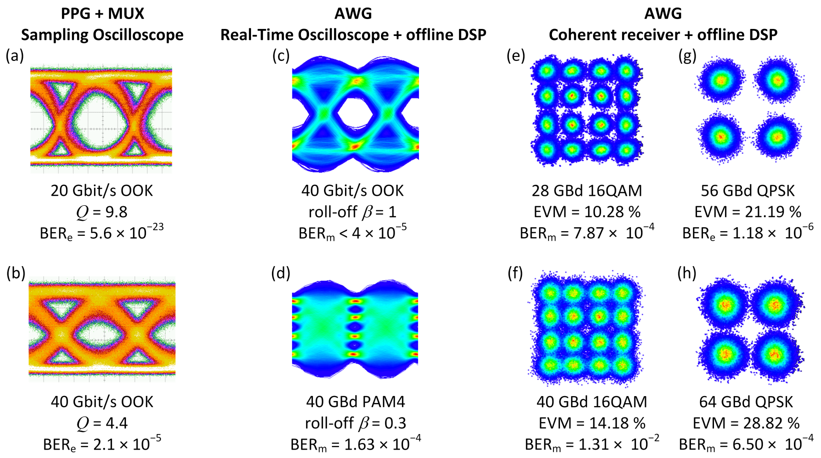

Fig. 5.5: Optical signaling using various modulation formats. (a) Eye diagrams for 20 Gbit/s OOK and (b) 40 Gbit/s OOK without pre-compensation or post-processing using a pulse-pattern generator and an equivalent-time sampling oscilloscope. (c) Eye diagrams for 40 Gbit/s OOK with an adaptive equalizer applied on the recorded data using a real-time sampling oscilloscope and offline DSP. Pulses with a raised-cosine spectrum and a roll-off factor of $\beta^{(\mathrm{ro})} = 1$ were used. (d) Eye diagram for 40 GBd (80 Gbit/s) PAM4 using pulse shaping with $\beta^{(\mathrm{ro})} = 0.3$ and offline DSP. (e-h) Constellation diagrams for (e) 28 GBd 16QAM, (f) 40 GBd 16QAM, (g) 56 GBd QPSK and (h) 64 GBd QPSK.

sampling factor of ten. Here, the SOH MZM was driven with a peak-to-peak voltage swing of 1.4 $\mathrm{V_{pp}}$ at the input coaxial connector of the module. No errors were found in our 62 µs-long recording (2.48×10^6 measured bit), which confirms that the BER is below 4×10^{-5}. For OOK at a line rate of 56 Gbit/s and using $\beta^{(\mathrm{ro})} = 0.1$, a $\mathrm{BER_m} = 1.96 \times 10^{-5}$ is measured (not displayed in the figure). Figure 5.5(d) shows the eye diagram for a PAM4 modulated signal, generated using $\beta^{(\mathrm{ro})} = 0.3$, at a symbol rate of 40 GBd (corresponding to a line rate of 80 Gbit/s). The BER is measured to be $\mathrm{BER_m} = 1.63 \times 10^{-4}$, well below the 7% overhead FEC threshold.

The IM/DD data generation is complemented by the generation of QAM signals, driving the electrically packaged SOH IQ modulator by a two-channel AWG and detecting the signal by a coherent receiver. Figure 5.5(e) shows the constellation diagrams for a 28 GBd 16QAM signal. The BER is measured to be $\mathrm{BER_m} = 7.87 \times 10^{-4}$. For 40 GBd, see Fig. 5.5(f), the BER increases to 1.31×10^{-2} but stays below the threshold of soft-decision FEC codes with a 20% overhead [176]. This results in a line rate of 160 Gbit/s and a post-FEC net data rate of 133 Gbit/s on a single polarization. Using QPSK signals, symbol rates of 56 Gbd and 64 GBd were generated with a BER below the threshold for a hard-decision FEC with 7% overhead, see Fig. 5.5(g) and Fig. 5.5(h). Note that at a symbol rate of 64 GBd, we used a PRBS of length $2^{11} - 1$ due to hardware limitations of our AWG. In all data generation experiments, a gate field of 50 V/µm has been applied to the modulator substrate [85].

These results compare well with previously published signaling demonstrations using SiP modulators accessed by metal wire bonds, for which 16QAM symbol rates of 28 GBd and line rates of 112 Gbit/s were demonstrated for a single polarization. Relying on the published state-of-the art, we believe that our demonstrations of 64 GBd QPSK and of 40 GBd 16QAM correspond to the highest symbol rate and the highest line rate achieved so far with a wire-bonded SiP modulators [166] and that the approach can well compete with more complex packaging concepts based on flip-chip bonding [157]. In comparison to earlier demonstrations of packaged pn-depletion-type MZMs, our SOH device features a significantly lower voltage-length product of only $U_\pi L = 0.9\,\mathrm{Vmm}$, well below that of best-in-class depletion-type SiP modulators with $U_\pi L = 6\,\mathrm{Vmm}$ [72].

5.5 Summary

We demonstrate for the first time that electrical packaging of high-speed SOH modulators is possible without significantly degrading the performance of the devices. To this end, we developed a dedicated packaging concept that utilizes technically simple metal wire bonding for packaging of highly compact SOH devices. The concept relies on high-resolution ceramic PCBs that allow to adapt the interposer bond-pad pitch to that of the PIC, thereby permitting connections through short parallel metal wire bonds that are amenable to broadband packaging of densely integrated device arrays. The modulators feature a π-voltage-length product of $U_\pi L = 0.9\,\mathrm{Vmm}$ and a π-voltage-loss product of $aU_\pi L = 2.1\,\mathrm{dBV}$, thereby outperforming conventional depletion-type pn-modulators. In our experiments, we demonstrate generation of intensity modulated signals with line rates of up to 80 Gbit/s as well as of QPSK and 16QAM signals with symbol rates up to 64 GBd and line rates up to 160 Gbit/s, respectively. In combination with recent progress regarding EO material stability [20] and novel technologies for hybrid photonic integration [172], our concept builds upon the intrinsic efficiency and performance advantages demonstrated for die-level SOH devices and allows to exploit them on the level of electrically packaged communication modules.

[End of paper [J3]]

6 Summary and outlook

Silicon photonics exploits highly sophisticated fabrication processes developed for the CMOS microelectronics industry and stands out due to high integration densities, high yield, and scalable low-cost manufacturing. As electro-optic (EO) modulators translate electrical signals into the optical domain, they are key components in optical communication systems. However, the energy efficiency even of highly-optimized all-silicon EO modulators is moderate due to the limited efficiency of the underlying plasma-dispersion effect. This can be overcome by combining the silicon platform with advanced organic EO materials that offer EO coefficients in excess of 300 pm/V. The resulting silicon-organic hybrid (SOH) EO modulators offer high energy efficiency combined with ease of fabrication, high modulation speeds and small footprints. In this work, aspects that are specifically relevant for the use of SOH modulators in high-speed optical communication systems were addressed.

For an accurate understanding and a quantitatively reliable description of the dynamic EO properties of SOH modulators, a model that accounts for the various bandwidth-limiting effects was formulated and experimentally verified. To the best of our knowledge, this represents the first experimental verification of a general model of slot-waveguide modulators. Based on this model, design guidelines for optimized modulators trading optical loss due to free-carrier absorption, for EO bandwidth, and for energy efficiency were derived. The model allows to derive EO properties from purely electrical measurements, which is key for fast wafer-level characterization of SOH modulators. To test SOH modulators with technically relevant intensity-modulation and direct-detection (IM/DD) formats, a number of experimental demonstrations was performed. Intensity-modulated duobinary (IDB) signaling with electrical drive signals generated by a BiCMOS signal conditioning chip was demonstrated with a line rate of 100 Gbit/s. The demonstration based on the BiCMOS chip represents the first demonstration of signaling using SOH modulators without laboratory-style test and measurement equipment for signal generation. Using four-level pulse-amplitude modulation (PAM4), a line rate of 120 Gbit/s was demonstrated using a modulator of only 0.5 mm in length. This represented the highest line rate achieved with a sub-millimeter Mach-Zehnder modulator (MZM) on the silicon photonic platform. To enable electrical packaging of densely integrated SOH modulators, an electrical packaging concept based on high-resolution ceramic printed circuit boards (PCBs) was developed. This concept was validated by demonstrating line rates up to 160 Gbit/s using an electrically packaged SOH in-phase/quadrature-phase (IQ) modulator.

The experimental and theoretical findings of this work advance the SOH technology and are of relevance for bringing SOH modulators from a pure research topic closer to practical application. The work documented in this thesis will have to be complemented by a few further steps to bridge final gaps towards practical deployment. As an example, the performance of the modulator can be further improved. Based on the theoretical model derived in this work, optimized designs can be fabricated and a larger space of parameter variations could be explored experimentally. Theoretical considerations in this work suggest that SOH modulators with π-voltages smaller than 1 V, EOE bandwidths larger than 100 GHz and low optical losses should be feasible with devices shorter than 1 mm.

Additionally, future work will focus on testing and demonstrating improved thermal and photo-chemical stability. While there has been remarkable progress in terms of reliability of organic EO materials in recent years, more extensive testing has to be done to fulfill industrial requirements. Further, for practical applications and potential commercial use, fabrication, packaging and testing processes have to be developed and improved.

If these steps are successful, SOH modulators have great potential to be used in commercial communication, metrology and sensing applications. Beyond these more traditional applications, SOH modulators are promising candidates for the emerging fields of quantum computing and quantum communications, as well as for low-temperature microwave experiments and for cryogenic computing. Here, broadband links with high thermal isolation are required to transport data from low-temperature regions, e.g., from superconducting circuits operating at 4 K or less, to room-temperature receivers connected to conventional electronic circuits. Optical links are the ideal solution to this problem because glass fibers offer large bandwidths and low thermal conductivity. However, the optical transmitter in the cryostat has to be extremely power-efficient to avoid any detrimental thermal load. Conventional all-Si EO modulators have limited efficiency and suffer from carrier freeze-out if operated at cryogenic temperatures. In contrast, SOH modulators exploiting the Pockels effect show excellent energy-efficiency along with low optical loss and could fulfill all of these requirements ideally.

Bibliography

[1] P. Jonsson, S. Carson, J. Sethi, M. Arvedson, R. Svenningsson, P. Lindberg, K. Öhman, and P. Hedlund, “Ericsson mobility report,” *Ericsson: Stockholm, Sweden*, 2018.

[2] K. Kao and G. Hockham, “Dielectric-fibre surface waveguides for optical frequencies,” *Proceedings of the Institution of Electrical Engineers*, vol. 113, pp. 1151–1158(7), 1966.

[3] “https://www.nobelprize.org/prizes/physics/2009/kao/facts/,” 2019. [Online; accessed 30-July-2019].

[4] G. P. Agrawal, *Optical Communication: Its History and Recent Progress*, pp. 177–199. Cham: Springer International Publishing, 2016.

[5] T. Miya, Y. Terunuma, T. Hosaka, and T. Miyashita, “Ultimate low-loss single-mode fibre at 1.55 µm,” *Electronics Letters*, vol. 15, no. 4, pp. 106–108, 1979.

[6] Z. Alferov, “Double heterostructure lasers: early days and future perspectives,” *IEEE Journal of Selected Topics in Quantum Electronics*, vol. 6, no. 6, pp. 832–840, 2000.

[7] I. Hayashi, M. Panish, P. Foy, and S. Sumski, “Junction lasers which operate continuously at room temperature,” *Applied Physics Letters*, vol. 17, no. 3, pp. 109–111, 1970.

[8] P. Becker, A. Olsson, and J. Simpson, *Erbium-Doped Fiber Amplifiers: Fundamentals and Technology*. Optics and Photonics, Elsevier Science, 1999.

[9] S. E. Miller, “Integrated optics: An introduction,” *The Bell System Technical Journal*, vol. 48, no. 7, pp. 2059–2069, 1969.

[10] R. Soref and J. Larenzo, “All-silicon active and passive guided-wave components for λ=1.3 and 1.6 µm,” *IEEE Journal of Quantum Electronics*, vol. 22, no. 6, pp. 873–879, 1986.

[11] M. Smit, J. van der Tol, and M. Hill, “Moore’s law in photonics,” *Laser & Photonics Reviews*, vol. 6, no. 1, pp. 1–13, 2012.

[12] R. Nagarajan, C. H. Joyner, R. P. Schneider, J. S. Bostak, T. Butrie, A. G. Dentai, V. G. Dominic, P. W. Evans, M. Kato, M. Kauffman, D. J. H. Lambert, S. K. Mathis, A. Mathur, R. H. Miles, M. L. Mitchell, M. J. Missey, S. Murthy, A. C. Nilsson, F. H. Peters, S. C. Pennypacker, J. L. Pleumeekers, R. A. Salvatore, R. K. Schlenker, R. B. Taylor, Huan-Shang Tsai, M. F. Van Leeuwen, J. Webjorn, M. Ziari, D. Perkins, J. Singh, S. G. Grubb, M. S. Reffle, D. G. Mehuys, F. A. Kish, and D. F. Welch, “Large-scale photonic integrated circuits,” *IEEE Journal of Selected Topics in Quantum Electronics*, vol. 11, no. 1, pp. 50–65, 2005.

[13] Cisco Global Cloud Index, “Forecast and methodology, 2015-2020 white paper,” 2016.

[14] T. Tsuchizawa, K. Yamada, H. Fukuda, T. Watanabe, Jun-ichi Takahashi, M. Takahashi, T. Shoji, E. Tamechika, S. Itabashi, and H. Morita, “Microphotonics devices based on silicon microfabrication technology,” *IEEE Journal of Selected Topics in Quantum Electronics*, vol. 11, no. 1, pp. 232–240, 2005.

[15] D. Inniss and R. Rubenstein, *Silicon Photonics: Fueling the Next Information Revolution*. Morgan Kaufmann, 2016.

[16] J. Witzens, “High-speed silicon photonics modulators,” *Proceedings of the IEEE*, vol. 106, no. 12, pp. 2158–2182, 2018.

[17] O. Marshall, M. Hsu, Z. Wang, B. Kunert, C. Koos, and D. Van Thourhout, “Heterogeneous integration on silicon photonics,” *Proceedings of the IEEE*, vol. 106, no. 12, pp. 2258–2269, 2018.

[18] C. Kieninger, Y. Kutuvantavida, D. L. Elder, S. Wolf, H. Zwickel, M. Blaicher, J. N. Kemal, M. Lauermann, S. Randel, W. Freude, L. R. Dalton, and C. Koos, “Ultra-high electro-optic activity demonstrated in a silicon-organic hybrid modulator,” *Optica*, vol. 5, no. 6, p. 739, 2018.

[19] S. Wolf, *Silicon-organic hybrid (SOH) electro-optic modulators for high-speed and power-efficient communications*, vol. 23 of *Karlsruhe series in photonics & communications*. KIT Scientific Publishing, 2018.

[20] C. Kieninger, Y. Kutuvantavida, H. Miura, J. N. Kemal, H. Zwickel, F. Qiu, M. Lauermann, W. Freude, S. Randel, S. Yokoyama, and C. Koos, “Demonstration of long-term thermally stable silicon-organic hybrid modulators at 85°C,” *Optics Express*, vol. 26, no. 21, pp. 27955–27964, 2018.

[21] M. Lauermann, S. Wolf, W. Hartmann, R. Palmer, Y. Kutuvantavida, H. Zwickel, A. Bielik, L. Altenhain, J. Lutz, R. Schmid, T. Wahlbrink,

J. Bolten, A. L. L. Giesecke, W. Freude, and C. Koos, “Generation of 64 GBd 4ASK signals using a silicon-organic hybrid modulator at 80°C,” *Optics Express*, vol. 24, no. 9, p. 9389, 2016.

[22] S. M. Sze and K. K. Ng, *Physics of Semiconductor Devices*. Wiley-Interscience, 2006.

[23] A. Rickman, “The commercialization of silicon photonics,” *Nature Photonics*, vol. 8, no. 8, pp. 579–582, 2014.

[24] A. H. Atabaki, S. Moazeni, F. Pavanello, H. Gevorgyan, J. Notaros, L. Alloatti, M. T. Wade, C. Sun, S. A. Kruger, H. Meng, K. Al Qubaisi, I. Wang, B. Zhang, A. Khilo, C. V. Baiocco, M. A. Popović, V. M. Stojanović, and R. J. Ram, “Integrating photonics with silicon nanoelectronics for the next generation of systems on a chip,” *Nature*, vol. 556, no. 7701, pp. 349–354, 2018.

[25] T. Baehr-Jones, T. Pinguet, P. Lo Guo-Qiang, S. Danziger, D. Prather, and M. Hochberg, “Myths and rumours of silicon photonics,” *Nature Photonics*, vol. 6, no. 4, pp. 206–208, 2012.

[26] R. W. Boyd, *Nonlinear Optics*. Academic Press, third ed., 2008.

[27] R. Soref and B. Bennett, “Electrooptical effects in silicon,” *IEEE Journal of Quantum Electronics*, vol. 23, no. 1, pp. 123–129, 1987.

[28] W. Franz, “Einfluß eines elektrischen Feldes auf eine optische Absorptionskante,” *Zeitschrift Naturforschung Teil A*, vol. 13, pp. 484–489, 1958.

[29] G. T. Reed and C. J. Png, “Silicon optical modulators,” *Materials Today*, vol. 8, no. 1, pp. 40 – 50, 2005.

[30] R. S. Jacobsen, K. N. Andersen, P. I. Borel, J. Fage-Pedersen, L. H. Frandsen, O. Hansen, M. Kristensen, A. V. Lavrinenko, G. Moulin, H. Ou, C. Peucheret, B. Zsigri, and A. Bjarklev, “Strained silicon as a new electro-optic material,” *Nature*, vol. 441, no. 7090, pp. 199–202, 2006.

[31] P. Damas, M. Berciano, G. Marcaud, C. A. Ramos, D. Marris-Morini, E. Cassan, and L. Vivien, “Comprehensive description of the electro-optic effects in strained silicon waveguides,” *Journal of Applied Physics*, vol. 122, no. 15, p. 153105, 2017.

[32] C. Klingshirn, *Semiconductor optics*. Graduate texts in physics, Springer, 4. ed., 2012.

[33] G. T. Reed, *Silicon photonics : the state of the art*. Wiley, 2008.

[34] E. L. Wooten, K. M. Kissa, A. Yi-Yan, E. J. Murphy, D. A. Lafaw, P. F. Hallemeier, D. Maack, D. V. Attanasio, D. J. Fritz, G. J. McBrien, and D. E. Bossi, “A review of lithium niobate modulators for fiber-optic communications systems,” *IEEE Journal of Selected Topics in Quantum Electronics*, vol. 6, no. 1, pp. 69–82, 2000.

[35] E. H. Voges and K. Petermann, eds., *Optische Kommunikationstechnik: Handbuch für Wissenschaft und Industrie*. Springer, 2002.

[36] C. Wang, M. Zhang, X. Chen, M. Bertrand, A. Shams-Ansari, S. Chandrasekhar, P. Winzer, and M. Lončar, “Integrated lithium niobate electro-optic modulators operating at CMOS-compatible voltages,” *Nature*, vol. 562, no. 7725, pp. 101–104, 2018.

[37] S. Abel, T. Stöferle, C. Marchiori, C. Rossel, M. D. Rossell, R. Erni, D. Caimi, M. Sousa, A. Chelnokov, B. J. Offrein, and J. Fompeyrine, “A strong electro-optically active lead-free ferroelectric integrated on silicon,” *Nature Communications*, vol. 4, no. 1, 2013.

[38] S. Abel, F. Eltes, J. E. Ortmann, A. Messner, P. Castera, T. Wagner, D. Urbonas, A. Rosa, A. M. Gutierrez, D. Tulli, P. Ma, B. Baeuerle, A. Josten, W. Heni, D. Caimi, L. Czornomaz, A. A. Demkov, J. Leuthold, P. Sanchis, and J. Fompeyrine, “Large Pockels effect in micro- and nanostructured barium titanate integrated on silicon,” *Nature Materials*, vol. 18, no. 1, pp. 42–47, 2018.

[39] A. Messner, F. Eltes, P. Ma, S. Abel, B. Baeuerle, A. Josten, W. Heni, D. Caimi, J. Fompeyrine, and J. Leuthold, “Plasmonic ferroelectric modulators,” *Journal of Lightwave Technology*, vol. 37, no. 2, pp. 281–290, 2019.

[40] S. Lange, S. Wolf, J. Lutz, L. Altenhain, R. Schmid, R. Kaiser, M. Schell, C. Koos, and S. Randel, “100 GBd intensity modulation and direct detection with an InP-based monolithic DFB laser Mach-Zehnder modulator,” *Journal of Lightwave Technology*, vol. 36, no. 1, pp. 97–102, 2018.

[41] P. C. Schindler, D. Korn, C. Stamatiadis, M. F. OKeefe, L. Stampoulidis, R. Schmogrow, P. Zakynthinos, R. Palmer, N. Cameron, Y. Zhou, R. G. Walker, E. Kehayas, S. Ben-Ezra, I. Tomkos, L. Zimmermann, K. Petermann, W. Freude, C. Koos, and J. Leuthold, “Monolithic GaAs electro-optic IQ modulator demonstrated at 150 Gbit/s with 64QAM,” *Journal of Lightwave Technology*, vol. 32, no. 4, pp. 760–765, 2014.

[42] A. Abbasi, J. Verbist, L. A. Shiramin, M. Verplaetse, T. De Keulenaer, R. Vaernewyck, R. Pierco, A. Vyncke, X. Yin, G. Torfs, G. Morthier, J. Bauwelinck, and G. Roelkens, “100-Gb/s electro-absorptive duobinary modulation of an InP-on-Si DFB laser,” *IEEE Photonics Technology Letters*, vol. 30, no. 12, pp. 1095–1098, 2018.

[43] J. Witzens, “Silicon photonics: Modulators make efficiency leap,” *Nature Photonics*, vol. 11, no. 8, p. 459, 2017.

[44] J. Pfeifle, L. Alloatti, W. Freude, J. Leuthold, and C. Koos, “Silicon-organic hybrid phase shifter based on a slot waveguide with a liquid-crystal cladding,” *Optics Express*, vol. 20, no. 14, pp. 15359–15376, 2012.

[45] D. Korn, *Silicon-organic hybrid platform for photonic integrated circuits*, vol. 15 of *Karlsruhe series in photonics and communications*. KIT Scientific Publishing, 2015.

[46] L. R. Dalton, P. A. Sullivan, and D. H. Bale, “Electric field poled organic electro-optic materials: State of the art and future prospects,” *Chemical Reviews*, vol. 110, no. 1, pp. 25–55, 2010.

[47] W. Jin, P. V. Johnston, D. L. Elder, A. F. Tillack, B. C. Olbricht, J. Song, P. J. Reid, R. Xu, B. H. Robinson, and L. R. Dalton, “Benzocyclobutene barrier layer for suppressing conductance in nonlinear optical devices during electric field poling,” *Applied Physics Letters*, vol. 104, no. 24, p. 243304, 2014.

[48] W. Heni, Y. Kutuvantavida, C. Haffner, H. Zwickel, C. Kieninger, S. Wolf, M. Lauermann, Y. Fedoryshyn, A. F. Tillack, L. E. Johnson, D. L. Elder, B. H. Robinson, W. Freude, C. Koos, J. Leuthold, and L. R. Dalton, “Silicon-organic and plasmonic-organic hybrid photonics,” *ACS Photonics*, vol. 4, no. 7, pp. 1576–1590, 2017.

[49] C. Koos, J. Leuthold, W. Freude, M. Kohl, L. Dalton, W. Bogaerts, A. L. Giesecke, M. Lauermann, A. Melikyan, S. Koeber, S. Wolf, C. Weimann, S. Muehlbrandt, K. Koehnle, J. Pfeifle, W. Hartmann, Y. Kutuvantavida, S. Ummethala, R. Palmer, D. Korn, L. Alloatti, P. C. Schindler, D. L. Elder, T. Wahlbrink, and J. Bolten, “Silicon-organic hybrid (SOH) and plasmonic-organic hybrid (POH) integration,” *Journal of Lightwave Technology*, vol. 34, no. 2, pp. 256–268, 2016.

[50] R. Ding, T. Baehr-Jones, Y. Liu, R. Bojko, J. Witzens, S. Huang, J. Luo, S. Benight, P. Sullivan, J.-M. Fedeli, M. Fournier, L. Dalton, A. Jen, and M. Hochberg, “Demonstration of a low $V_\pi L$ modulator with GHz

bandwidth based on electro-optic polymer-clad silicon slot waveguides," *Optics Express*, vol. 18, no. 15, p. 15618, 2010.

[51] C. Koos, J. Brosi, M. Waldow, W. Freude, and J. Leuthold, "Silicon-on-insulator modulators for next-generation 100 Gbit/s-Ethernet," in *European Conference on Optical Communication (ECOC)*, vol. 2007, pp. P056–P056, 2007.

[52] J. J. Wolff and R. Wortmann, "Organic materials for non-linear optics: The 2D approach," *Journal für Praktische Chemie/Chemiker-Zeitung*, vol. 340, no. 2, pp. 99–111, 1998.

[53] R. Palmer, *Silicon photonic modulators for low-power applications*, vol. 18 of *Karlsruhe series in photonics & communications*. KIT Scientific Publishing, 2015.

[54] F. Qiu, H. Miura, A. M. Spring, J. Hong, D. Maeda, M. aki Ozawa, K. Odoi, and S. Yokoyama, "An electro-optic polymer-cladded TiO_2 waveguide modulator," *Applied Physics Letters*, vol. 109, no. 17, p. 173301, 2016.

[55] W. Heni, C. Haffner, D. L. Elder, A. F. Tillack, Y. Fedoryshyn, R. Cottier, Y. Salamin, C. Hoessbacher, U. Koch, B. Cheng, B. Robinson, L. R. Dalton, and J. Leuthold, "Nonlinearities of organic electro-optic materials in nanoscale slots and implications for the optimum modulator design," *Optics Express*, vol. 25, no. 3, pp. 2627–2653, 2017.

[56] S. Koeber, R. Palmer, M. Lauermann, W. Heni, D. L. Elder, D. Korn, M. Woessner, L. Alloatti, S. Koenig, P. C. Schindler, H. Yu, W. Bogaerts, L. R. Dalton, W. Freude, J. Leuthold, and C. Koos, "Femtojoule electro-optic modulation using a silicon-organic hybrid device," *Light: Science & Applications*, vol. 4, no. 2, p. e255, 2015.

[57] Y. Enami, J. Luo, and A. K.-Y. Jen, "Short hybrid polymer/sol-gel silica waveguide switches with high in-device electro-optic coefficient based on photostable chromophore," *AIP Advances*, vol. 1, no. 4, p. 042137, 2011.

[58] Y.-J. Cheng, J. Luo, S. Huang, X. Zhou, Z. Shi, T.-D. Kim, D. H. Bale, S. Takahashi, A. Yick, B. M. Polishak, S.-H. Jang, L. R. Dalton, P. J. Reid, W. H. Steier, and A. K.-Y. Jen, "Donor-acceptor thiolated polyenic chromophores exhibiting large optical nonlinearity and excellent photostability," *Chemistry of Materials*, vol. 20, no. 15, pp. 5047–5054, 2008.

[59] X. Piao, X. Zhang, Y. Mori, M. Koishi, A. Nakaya, S. Inoue, I. Aoki, A. Otomo, and S. Yokoyama, “Nonlinear optical side-chain polymers post-functionalized with high-β chromophores exhibiting large electro-optic property,” *Journal of Polymer Science Part A: Polymer Chemistry*, vol. 49, no. 1, pp. 47–54, 2010.

[60] H. Miura, F. Qiu, A. M. Spring, T. Kashino, T. Kikuchi, M. Ozawa, H. Nawata, K. Odoi, and S. Yokoyama, “High thermal stability 40 GHz electro-optic polymer modulators,” *Optics Express*, vol. 25, no. 23, p. 28643, 2017.

[61] “GR-468-CORE: Generic reliability assurance requirements for optoelectronic devices used in telecommunications equipment,” *Telcordia*, 2004.

[62] G. Gupta, W. H. Steier, Y. Liao, J. Luo, L. R. Dalton, and A. K.-Y. Jen, “Modeling photobleaching of optical chromophores: Light-intensity effects in precise trimming of integrated polymer devices,” *The Journal of Physical Chemistry C*, vol. 113, no. 28, pp. 12615–12615, 2009.

[63] L. Soldano and E. Pennings, “Optical multi-mode interference devices based on self-imaging: principles and applications,” *Journal of Lightwave Technology*, vol. 13, no. 4, pp. 615–627, 1995.

[64] H. Chung, W. S. C. Chang, and E. L. Adler, “Modeling and optimization of traveling-wave $LiNbO_3$ interferometric modulators,” *IEEE Journal of Quantum Electronics*, vol. 27, pp. 608–617, 1991.

[65] F. Merget, S. S. Azadeh, J. Mueller, B. Shen, M. P. Nezhad, J. Hauck, and J. Witzens, “Silicon photonics plasma-modulators with advanced transmission line design,” *Optics Express*, vol. 21, no. 17, pp. 19593–19607, 2013.

[66] D. A. B. Miller, “Energy consumption in optical modulators for interconnects,” *Optics Express*, vol. 20, no. S2, pp. A293–A308, 2012.

[67] T. Pinguet, B. Analui, E. Balmater, D. Guckenberger, M. Harrison, R. Koumans, D. Kucharski, Y. Liang, G. Masini, A. Mekis, S. Mirsaidi, A. Narasimha, M. Peterson, D. Rines, V. Sadagopan, S. Sahni, T. J. Sleboda, D. Song, Y. Wang, B. Welch, J. Witzens, J. Yao, S. Abdalla, S. Gloeckner, P. De Dobbelaere, and G. Capellini, “Monolithically integrated high-speed CMOS photonic transceivers,” in *2008 5th IEEE International Conference on Group IV Photonics*, pp. 362–364, 2008.

[68] M. T. Wade, F. Pavanello, J. Orcutt, R. Kumar, J. M. Shainline, V. Stojanović, R. Ram, and M. A. Popović, “Scaling zero-change photonics: An

active photonics platform in a 32 nm microelectronics SOI CMOS process," in *2015 Conference on Lasers and Electro-Optics (CLEO)*, pp. 1–2, 2015.

[69] V. S. Jason S. Orcutt, Rajeev J. Ram, "Integration of silicon photonics into electronic processes," in *Silicon Photonics VIII (March 14, 2013), San Francisco, California, United States. (Proceedings of SPIE)*, vol. 8629, 2013.

[70] D. Patel, A. Samani, V. Veerasubramanian, S. Ghosh, and D. V. Plant, "Silicon photonic segmented modulator-based electro-optic DAC for 100 Gb/s PAM-4 generation," *IEEE Photonics Technology Letters*, vol. 27, no. 23, pp. 2433–2436, 2015.

[71] S. S. Azadeh, F. Merget, S. Romero-García, A. Moscoso-Mártir, N. von den Driesch, J. Müller, S. Mantl, D. Buca, and J. Witzens, "Low V_π silicon photonics modulators with highly linear epitaxially grown phase shifters," *Optics Express*, vol. 23, no. 18, pp. 23526–23550, 2015.

[72] J. Fujikata, M. Noguchi, J. Han, S. Takahashi, M. Takenaka, and T. Nakamura, "Record-high modulation-efficiency depletion-type Si-based optical modulator with in-situ B doped strained SiGe layer on Si waveguide for 1.3 μm wavelength," in *European Conference on Optical Communications (ECOC)*, p. Tu.3.A.4, 2016.

[73] J. Fujikata, M. Takahashi, S. Takahashi, T. Horikawa, and T. Nakamura, "High-speed and high-efficiency Si optical modulator with MOS junction, using solid-phase crystallization of polycrystalline silicon," *Japanese Journal of Applied Physics*, vol. 55, no. 4, p. 042202, 2016.

[74] T. Hiraki, T. Aihara, K. Hasebe, K. Takeda, T. Fujii, T. Kakitsuka, T. Tsuchizawa, H. Fukuda, and S. Matsuo, "Heterogeneously integrated III–V/Si MOS capacitor Mach–Zehnder modulator," *Nature Photonics*, vol. 11, no. 8, p. 482, 2017.

[75] J.-H. Han, F. Boeuf, J. Fujikata, S. Takahashi, S. Takagi, and M. Takenaka, "Efficient low-loss InGaAsP/Si hybrid MOS optical modulator," *Nature Photonics*, vol. 11, no. 8, p. 486, 2017.

[76] V. Sorianello, M. Midrio, G. Contestabile, I. Asselberghs, J. Van Campenhout, C. Huyghebaert, I. Goykhman, A. Ott, A. C. Ferrari, and M. Romagnoli, "Graphene–silicon phase modulators with gigahertz bandwidth," *Nature Photonics*, vol. 12, no. 1, p. 40, 2018.

[77] S. Abel, F. Eltes, J. E. Ortmann, A. Messner, P. Castera, T. Wagner, D. Urbonas, A. Rosa, A. M. Gutierrez, D. Tulli, P. Ma, B. Baeuerle, A. Josten, W. Heni, D. Caimi, L. Czornomaz, A. A. Demkov, J. Leuthold, P. Sanchis, and J. Fompeyrine, “Large pockels effect in micro-and nanostructured barium titanate integrated on silicon,” *Nature Materials*, vol. 18, no. 1, p. 42, 2019.

[78] K. Alexander, J. P. George, J. Verbist, K. Neyts, B. Kuyken, D. Van Thourhout, and J. Beeckman, “Nanophotonic Pockels modulators on a silicon nitride platform,” *Nature Communications*, vol. 9, no. 1, p. 3444, 2018.

[79] C. Hoessbacher, Y. Salamin, Y. Fedoryshyn, W. Heni, B. Baeuerle, A. Josten, C. Haffner, M. Zahner, H. Chen, D. L. Elder, S. Wehrli, D. Hillerkuss, D. Van Thourhout, J. Van Campenhout, L. R. Dalton, C. Hafner, and J. Leuthold, “Optical interconnect solution with plasmonic modulator and Ge photodetector array,” *IEEE Photonics Technology Letters*, vol. 29, no. 21, pp. 1760–1763, 2017.

[80] M. Burla, C. Hoessbacher, W. Heni, C. Haffner, Y. Fedoryshyn, D. Werner, T. Watanabe, H. Massler, D. L. Elder, L. R. Dalton, and J. Leuthold, “500 GHz plasmonic Mach-Zehnder modulator enabling sub-THz microwave photonics,” *APL Photonics*, vol. 4, no. 5, p. 056106, 2019.

[81] L. Alloatti, R. Palmer, S. Diebold, K. P. Pahl, B. Chen, R. Dinu, M. Fournier, J.-M. Fedeli, T. Zwick, W. Freude, C. Koos, and J. Leuthold, “100 GHz silicon-organic hybrid modulator,” *Light: Science & Applications*, vol. 3, no. 5, p. e173, 2014.

[82] V. R. Almeida, Q. Xu, C. A. Barrios, and M. Lipson, “Guiding and confining light in void nanostructure,” *Optics Letters*, vol. 29, no. 11, pp. 1209–1211, 2004.

[83] C. Kieninger, Y. Kutuvantavida, H. Zwickel, S. Wolf, M. Lauermann, D. L. Elder, L. R. Dalton, W. Freude, S. Randel, and C. Koos, “Record-high in-device electro-optic coefficient of 359 pm/V in a silicon-organic hybrid (SOH) modulator,” *Conference on Lasers and Electro-Optics (CLEO)*, p. STu3N, 2017.

[84] R. Palmer, L. Alloatti, D. Korn, W. Heni, P. C. Schindler, J. Bolten, M. Karl, M. Waldow, T. Wahlbrink, W. Freude, C. Koos, and J. Leuthold, “Low-loss silicon strip-to-slot mode converters,” *IEEE Photonics Journal*, vol. 5, no. 1, pp. 2200409–2200409, 2013.

[85] L. Alloatti, D. Korn, R. Palmer, D. Hillerkuss, J. Li, A. Barklund, R. Dinu, J. Wieland, M. Fournier, J. Fedeli, H. Yu, W. Bogaerts, P. Dumon, R. Baets, C. Koos, W. Freude, and J. Leuthold, "42.7 Gbit/s electro-optic modulator in silicon technology," *Optics Express*, vol. 19, no. 12, p. 11841, 2011.

[86] H. Zwickel, S. Wolf, C. Kieninger, Y. Kutuvantavida, M. Lauermann, T. de Keulenaer, A. Vyncke, R. Vaernewyck, J. Luo, A. K.-Y. Jen, W. Freude, J. Bauwelinck, S. Randel, and C. Koos, "Silicon-organic hybrid (SOH) modulators for intensity-modulation / direct-detection links with line rates of up to 120 Gbit/s," *Optics Express*, vol. 25, no. 20, p. 23784, 2017.

[87] D. M. Pozar, *Microwave engineering*. Hoboken, NJ: Wiley, 4. ed., 2012.

[88] H.-J. Michel, *Zweitor-Analyse mit Leistungswellen (Teubner Studienbücher der Elektrotechnik)*. Teubner, 1981.

[89] W. Eisenstadt and Y. Eo, "S-parameter-based IC interconnect transmission line characterization," *IEEE Transactions on Components, Hybrids, and Manufacturing Technology*, vol. 15, no. 4, pp. 483–490, 1992.

[90] N. J. Parsons, A. C. O'Donnell, and K. K. Wong, "Design of efficient and wideband travelling-wave modulators," in *Society of Photo-Optical Instrumentation Engineers (SPIE) Conference Series* (R. T. Kersten, ed.), vol. 0651, p. 148, International Society for Optics and Photonics, 1986.

[91] J. Witzens, T. Baehr-Jones, and M. Hochberg, "Design of transmission line driven slot waveguide Mach-Zehnder interferometers and application to analog optical links," *Optics Express*, vol. 18, no. 16, p. 16902, 2010.

[92] A. Samani, D. Patel, M. Chagnon, E. El-Fiky, R. Li, M. Jacques, N. Abadía, V. Veerasubramanian, and D. V. Plant, "Experimental parametric study of 128 Gb/s PAM-4 transmission system using a multi-electrode silicon photonic Mach-Zehnder modulator," *Optics Express*, vol. 25, no. 12, p. 13252, 2017.

[93] S. Wolf, H. Zwickel, C. Kieninger, M. Lauermann, W. Hartmann, Y. Kutuvantavida, W. Freude, S. Randel, and C. Koos, "Coherent modulation up to 100 GBd 16QAM using silicon-organic hybrid (SOH) devices," *Optics Express*, vol. 26, no. 1, p. 220, 2018.

[94] S. Ummethala, T. Harter, K. Koehnle, Z. Li, S. Muehlbrandt, Y. Kutuvantavida, J. Kemal, P. Marin-Palomo, J. Schaefer, A. Tessmann, S. K. Garlapati, A. Bacher, L. Hahn, M. Walther, T. Zwick, S. Randel, W. Freude,

and C. Koos, “THz-to-optical conversion in wireless communications using an ultra-broadband plasmonic modulator,” *Nature Photonics*, vol. 13, no. 8, pp. 519–524, 2019.

[95] M. Lauermann, C. Weimann, A. Knopf, W. Heni, R. Palmer, S. Koeber, D. L. Elder, W. Bogaerts, J. Leuthold, L. R. Dalton, C. Rembe, W. Freude, and C. Koos, “Integrated optical frequency shifter in silicon-organic hybrid (SOH) technology,” *Optics Express*, vol. 24, no. 11, pp. 11694–11707, 2016.

[96] S. Shimotsu, S. Oikawa, T. Saitou, N. Mitsugi, K. Kubodera, T. Kawanishi, and M. Izutsu, “Single side-band modulation performance of a $LiNbO_3$ integrated modulator consisting of four-phase modulator waveguides,” *IEEE Photonics Technology Letters*, vol. 13, no. 4, pp. 364–366, 2001.

[97] X. Chen, M. M. Milosevic, S. Stanković, S. Reynolds, T. D. Bucio, K. Li, D. J. Thomson, F. Gardes, and G. T. Reed, “The emergence of silicon photonics as a flexible technology platform,” *Proceedings of the IEEE*, vol. 106, no. 12, pp. 2101–2116, 2018.

[98] L. Dalton and S. Benight, “Theory-guided design of organic electro-optic materials and devices,” *Polymers*, vol. 3, no. 3, pp. 1325–1351, 2011.

[99] S. Wolf, H. Zwickel, W. Hartmann, M. Lauermann, Y. Kutuvantavida, C. Kieninger, L. Altenhain, R. Schmid, J. Luo, A. K.-Y. Jen, S. Randel, W. Freude, and C. Koos, “Silicon-Organic Hybrid (SOH) Mach-Zehnder Modulators for 100 Gbit/s on-off Keying,” *Scientific Reports*, vol. 8, no. 1, p. 2598, 2018.

[100] S. Wolf, M. Lauermann, P. Schindler, G. Ronniger, K. Geistert, R. Palmer, S. Kober, W. Bogaerts, J. Leuthold, W. Freude, and C. Koos, “DAC-less amplifier-less generation and transmission of QAM signals using sub-volt silicon-organic hybrid modulators,” *Journal of Lightwave Technology*, vol. 33, no. 7, pp. 1425–1432, 2015.

[101] M. Lauermann, S. Wolf, P. C. Schindler, R. Palmer, S. Koeber, D. Korn, L. Alloatti, T. Wahlbrink, J. Bolten, M. Waldow, M. Koenigsmann, M. Kohler, D. Malsam, D. L. Elder, P. V. Johnston, N. Phillips-Sylvain, P. A. Sullivan, L. R. Dalton, J. Leuthold, W. Freude, and C. Koos, “40 GBd 16QAM signaling at 160 Gb/s in a silicon-organic hybrid modulator,” *Journal of Lightwave Technology*, vol. 33, no. 6, pp. 1210–1216, 2015.

[102] H. Zwickel, J. N. Kemal, C. Kieninger, Y. Kutuvantavida, J. Rittershofer, M. Lauermann, W. Freude, S. Randel, and C. Koos, “Electrically packaged silicon-organic hybrid (SOH) I/Q-modulator for 64 GBd operation,” *Optics Express*, vol. 26, no. 26, pp. 34580–34591, 2018.

[103] R. Ding, Y. Liu, Y. Ma, Y. Yang, Q. Li, A. E.-J. Lim, G.-Q. Lo, K. Bergman, T. Baehr-Jones, and M. Hochberg, “High-speed silicon modulator with slow-wave electrodes and fully independent differential drive,” *Journal of Lightwave Technology*, vol. 32, no. 12, pp. 2240–2247, 2014.

[104] M. Streshinsky, R. Ding, Y. Liu, A. Novack, Y. Yang, Y. Ma, X. Tu, E. K. S. Chee, A. E.-J. Lim, P. G.-Q. Lo, T. Baehr-Jones, and M. Hochberg, “Low power 50 Gb/s silicon traveling wave Mach-Zehnder modulator near 1300 nm,” *Optics Express*, vol. 21, no. 25, pp. 30350–30357, 2013.

[105] H. Yu and W. Bogaerts, “An equivalent circuit model of the traveling wave electrode for carrier-depletion-based silicon optical modulators,” *Journal of Lightwave Technology*, vol. 30, no. 11, pp. 1602–1609, 2012.

[106] R. Ding, Y. Liu, Q. Li, Y. Yang, Y. Ma, K. Padmaraju, A. E.-J. Lim, G.-Q. Lo, K. Bergman, T. Baehr-Jones, and M. Hochberg, “Design and characterization of a 30-GHz bandwidth low-power silicon traveling-wave modulator,” *Optics communications*, vol. 321, pp. 124–133, 2014.

[107] Y. Zhou, L. Zhou, H. Zhu, C. Wong, Y. Wen, L. Liu, X. Li, and J. Chen, “Modeling and optimization of a single-drive push–pull silicon Mach–Zehnder modulator,” *Photonics Research*, vol. 4, no. 4, pp. 153–161, 2016.

[108] J. Zhou, Q. Zhang, J. Wang, L. Zhu, and J. Hong, “Model and design of silicon photonic carrier-depletion Mach-Zehnder modulators for 400 Gb/s and beyond PAM and QAM applications,” in *Silicon Photonics XIV*, vol. 10923, p. 1092318, International Society for Optics and Photonics, 2019.

[109] J. Zhou, J. Wang, L. Zhu, and Q. Zhang, “High baud rate all-silicon photonics carrier depletion modulators,” *Journal of Lightwave Technology*, 2019.

[110] D. Patel, S. Ghosh, M. Chagnon, A. Samani, V. Veerasubramanian, M. Osman, and D. V. Plant, “Design, analysis, and transmission system performance of a 41 GHz silicon photonic modulator,” *Optics Express*, vol. 23, no. 11, pp. 14263–14287, 2015.

[111] D. Petousi, L. Zimmermann, A. Gajda, M. Kroh, K. Voigt, G. Winzer, B. Tillack, and K. Petermann, “Analysis of optical and electrical tradeoffs of traveling-wave depletion-type Si Mach–Zehnder modulators for high-speed operation,” *IEEE Journal of Selected Topics in Quantum Electronics*, vol. 21, no. 4, pp. 199–206, 2015.

[112] Y. R. Kwon, V. M. Hietala, and K. S. Champlin, “Quasi-TEM analysis of “slow-wave” mode propagation on coplanar microstructure MIS transmission lines.,” *IEEE transactions on microwave theory and techniques*, vol. 35, no. 6, pp. 545–551, 1987.

[113] M. Bass, *Handbook of optics*. McGraw-Hill, 1995.

[114] C. Haffner, W. Heni, D. L. Elder, Y. Fedoryshyn, N. Dordević, D. Chelladurai, U. Koch, K. Portner, M. Burla, B. Robinson, L. R. Dalton, and J. Leuthold, “Harnessing nonlinearities near material absorption resonances for reducing losses in plasmonic modulators,” *Opt. Mater. Express*, vol. 7, no. 7, pp. 2168–2181, 2017.

[115] P. D. Hale and D. F. Williams, “Calibrated measurement of optoelectronic frequency response,” *IEEE transactions on microwave theory and techniques*, vol. 51, no. 4, pp. 1422–1429, 2003.

[116] P. Steglich, C. Villringer, S. Pulwer, M. Casalboni, and S. Schrader, “Design optimization of silicon-on-insulator slot-waveguides for electro-optical modulators and biosensors,” in *Photoptics 2015* (R. M. Ribeiro P., ed.), vol. 181 of *Springer Proceedings in Physics*, pp. 173–187, Springer, 2016.

[117] J. Degallaix, R. Flaminio, D. Forest, M. Granata, C. Michel, L. Pinard, T. Bertrand, and G. Cagnoli, “Bulk optical absorption of high resistivity silicon at 1550 nm,” *Optics letters*, vol. 38, no. 12, pp. 2047–2049, 2013.

[118] L. Alloatti, M. Lauermann, C. Sürgers, C. Koos, W. Freude, and J. Leuthold, “Optical absorption in silicon layers in the presence of charge inversion/accumulation or ion implantation,” *Applied Physics Letters*, vol. 103, no. 5, p. 051104, 2013.

[119] R. Ding, T. Baehr-Jones, W.-J. Kim, X. Xiong, R. Bojko, J.-M. Fedeli, M. Fournier, and M. Hochberg, “Low-loss strip-loaded slot waveguides in Silicon-on-Insulator,” *Optics Express*, vol. 18, no. 24, p. 25061, 2010.

[120] J. D. Ambrosia and S. G. Kipp, “The 2015 Ethernet Roadmap,” *Ethernet Alliance White Paper (2015)*, 2015.

[121] "IEEE P802.3bs 400 Gb/s Ethernet Task Force."

[122] D. M. Kuchta, "Directly modulated VCSELs at ⩾ 50 Gb/s for short reach data communications," in *2016 IEEE Optical Interconnects Conference (OI)*, p. MD1, IEEE, 2016.

[123] J. Verbist, M. Verplaetse, A. Srinivasan, P. De Heyn, T. De Keulenaer, R. Pierco, R. Vaernewyck, A. Vyncke, P. Absil, G. Torfs, X. Yin, G. Roelkens, J. Van Campenhout, and J. Bauwelinck, "First real-time 100-Gb/s NRZ-OOK transmission over 2 km with a silicon photonic electro-absorption modulator," in *Optical Fiber Communication Conference (OFC) Postdeadline Papers*, p. Th5C.4, OSA, 2017.

[124] M. Verplaetse, R. Lin, J. Van Kerrebrouck, O. Ozolins, T. De Keulenaer, X. Pang, R. Pierco, R. Vaernewyck, A. Vyncke, R. Schatz, U. Westergren, G. Jacobsen, S. Popov, J. Chen, G. Torfs, J. Bauwelinck, and X. Yin, "Real-time 100 Gb/s transmission using three-level electrical duobinary modulation for short-reach optical interconnects," *Journal of Lightwave Technology*, vol. 35, no. 7, pp. 1313–1319, 2017.

[125] Y. Cheng, Q. J. Wang, and J. Pan, "1.55 µm high speed low chirp electroabsorption modulated laser arrays based on SAG scheme," *Optics Express*, vol. 22, no. 25, p. 31286, 2014.

[126] V. Katopodis, P. Groumas, Z. Zhang, R. Dinu, E. Miller, A. Konczykowska, J.-Y. Dupuy, A. Beretta, A. Dede, J. Choi, P. Harati, F. Jorge, V. Nodjiadjim, M. Riet, G. Cangini, A. Vannucci, N. Keil, H.-G. Bach, N. Grote, H. Avramopoulos, and C. Kouloumentas, "Polymer enabled 100 Gbaud connectivity for datacom applications," *Optics Communications*, vol. 362, pp. 13–21, 2016.

[127] P. Groumas, Z. Zhang, V. Katopodis, A. Konczykowska, J. Y. Dupuy, A. Beretta, A. Dede, J. H. Choi, P. Harati, F. Jorge, V. Nodjiadjim, M. Riet, R. Dinu, G. Cangini, E. Miller, A. Vannucci, N. Keil, H. G. Bach, N. Grote, M. Spyropoulou, H. Avramopoulos, and C. Kouloumentas, "Tunable 100 Gbaud transmitter based on hybrid polymer-to-polymer integration for flexible optical interconnects," *Journal of Lightwave Technology*, vol. 34, no. 2, pp. 407–418, 2016.

[128] S. Lange, S. Wolf, J. Lutz, L. Altenhain, R. Schmid, R. Kaiser, C. Koos, S. Randel, M. Schell, C. Koos, and S. Randel, "100 GBd intensity modulation and direct detection with an InP-based monolithic DFB laser Mach-

Zehnder modulator," in *Optical Fiber Communication Conference (OFC)*, vol. 36, p. Th5C.5, OSA, 2017.

[129] Y. Ogiso, J. Ozaki, N. Kashio, N. Kikuchi, H. Tanobe, Y. Ohiso, and M. Kohtoku, "100 Gb/s and 2 V V_π InP Mach-Zehnder modulator with an n-i-p-n heterostructure," *Electronics Letters*, vol. 52, no. 22, pp. 1866–1867, 2016.

[130] Y. Ogiso, T. Yamada, J. Ozaki, Y. Ueda, N. Kashio, N. Kikuchi, E. Yamada, H. Mawatari, H. Tanobe, S. Kanazawa, H. Yamazaki, Y. Ohiso, T. Fujii, M. Ishikawa, and M. Kohtoku, "Ultra-high bandwidth InP IQ modulator with 1.5 V V_π," in *ECOC 2016; 42nd European Conference on Optical Communication*, pp. 1–3, 2016.

[131] A. Samani, M. Chagnon, D. Patel, V. Veerasubramanian, S. Ghosh, M. Osman, Q. Zhong, and D. V. Plant, "A low-voltage 35-GHz silicon photonic modulator-enabled 112-Gb/s transmission system," *IEEE Photonics Journal*, vol. 7, no. 3, pp. 1–13, 2015.

[132] L. Chen, P. Dong, and Y.-K. Chen, "Chirp and dispersion tolerance of a single-drive push-pull silicon modulator at 28 Gb/s," *IEEE Photonics Technology Letters*, vol. 24, no. 11, pp. 936–938, 2012.

[133] A. Melikyan, K. Koehnle, M. Lauermann, R. Palmer, S. Koeber, S. Muehlbrandt, P. C. Schindler, D. L. Elder, S. Wolf, W. Heni, C. Haffner, Y. Fedoryshyn, D. Hillerkuss, M. Sommer, L. R. Dalton, D. Van Thourhout, W. Freude, M. Kohl, J. Leuthold, and C. Koos, "Plasmonic-organic hybrid (POH) modulators for OOK and BPSK signaling at 40 Gbit/s," *Optics Express*, vol. 23, no. 8, p. 9938, 2015.

[134] C. Haffner, W. Heni, Y. Fedoryshyn, J. Niegemann, A. Melikyan, D. L. Elder, B. Baeuerle, Y. Salamin, A. Josten, U. Koch, C. Hoessbacher, F. Ducry, L. Juchli, A. Emboras, D. Hillerkuss, M. Kohl, L. R. Dalton, C. Hafner, and J. Leuthold, "All-plasmonic Mach-Zehnder modulator enabling optical high-speed communication at the microscale," *Nature Photonics*, vol. 9, no. 8, pp. 525–528, 2015.

[135] C. Hoessbacher, A. Josten, B. Baeuerle, Y. Fedoryshyn, H. Hettrich, Y. Salamin, W. Heni, C. Haffner, C. Kaiser, R. Schmid, D. L. Elder, D. Hillerkuss, M. Möller, L. R. Dalton, and J. Leuthold, "Plasmonic modulator with >170 GHz bandwidth demonstrated at 100 GBd NRZ," *Optics Express*, vol. 25, no. 3, p. 1762, 2017.

[136] W. Hartmann, M. Lauermann, S. Wolf, H. Zwickel, Y. Kutuvantavida, J. Luo, A.-Y. Jen, W. Freude, and C. Koos, "100 Gbit/s OOK using a silicon-organic hybrid (SOH) modulator," in *European Conference on Optical Communication, ECOC*, 2015.

[137] H. Zwickel, T. De Keulenaer, S. Wolf, C. Kieninger, Y. Kutuvantavida, M. Lauermann, M. Verplaetse, R. Pierco, R. Vaernewyck, A. Vyncke, X. Yin, G. Torfs, W. Freude, E. Mentovich, J. Bauwelinck, and C. Koos, "100 Gbit/s serial transmission using a silicon-organic hybrid (SOH) modulator and a duobinary driver IC," in *Optical Fiber Communication Conference (OFC)*, p. W4I.5, OSA, 2017.

[138] M. Scholten, T. Coe, and J. Dillard, "Continuously-interleaved BCH (CI-BCH) FEC delivers best-in-class NECG for 40G and 100G metro applications," in *National Fiber Optic Engineers Conference*, p. NTuB3, OSA, 2010.

[139] H. Zwickel, S. Wolf, Y. Kutuvantavida, C. Kieninger, M. Lauermann, W. Freude, and C. Koos, "120 Gbit/s PAM-4 signaling using a silicon-organic hybrid (SOH) Mach-Zehnder modulator," in *European Conference on Optical Communication, ECOC*, 2016.

[140] F. Devaux, Y. Sorel, and J. Kerdiles, "Simple measurement of fiber dispersion and of chirp parameter of intensity modulated light emitter," *Journal of Lightwave Technology*, vol. 11, no. 12, pp. 1937–1940, 1993.

[141] Y. Ban, T. De Keulenaer, Z. Li, J. Van Kerrebrouck, J. H. Sinsky, B. Kozicki, J. Bauwelinck, and G. Torfs, "A wide-band, 5-tap transversal filter with improved testability for equalization up to 84 Gb/s," *IEEE Microwave and Wireless Components Letters*, vol. 25, no. 11, pp. 739–741, 2015.

[142] M. Watts, W. Zortman, D. Trotter, R. Young, and A. Lentine, "Low-voltage, compact, depletion-mode, silicon Mach-Zehnder modulator," *IEEE Journal of Selected Topics in Quantum Electronics*, vol. 16, no. 1, pp. 159–164, 2010.

[143] M. Lauermann, R. Palmer, S. Koeber, P. C. Schindler, D. Korn, T. Wahlbrink, J. Bolten, M. Waldow, D. L. Elder, L. R. Dalton, J. Leuthold, W. Freude, and C. Koos, "Low-power silicon-organic hybrid (SOH) modulators for advanced modulation formats," *Optics Express*, vol. 22, no. 24, p. 29927, 2014.

[144] S. Wolf, H. Zwickel, C. Kieninger, Y. Kutuvantavida, M. Lauermann, J. Lutz, L. Altenhain, R. Schmid, W. Freude, C. Koos, and S. Randel,

"Silicon-organic hybrid (SOH) IQ modulator for 100 GBd 16QAM operation," in *2017 Optical Fiber Communications Conference and Exhibition, OFC 2017 - Proceedings*, 2017.

[145] P. Winzer and R.-J. Essiambre, "Advanced optical modulation formats," *Proceedings of the IEEE*, vol. 94, no. 5, pp. 952–985, 2006.

[146] T. De Keulenaer, J. De Geest, G. Torfs, J. Bauwelinck, Y. Ban, J. Sinsky, and B. Kozicki, "56+ Gb/s serial transmission using duo-binary signaling," in *DesignCon*, pp. 10TH–3, 2015.

[147] A. Lender, "The duobinary technique for high-speed data transmission," *Transactions of the American Institute of Electrical Engineers, Part I: Communication and Electronics*, vol. 82, no. 2, pp. 214–218, 1963.

[148] A. Sekey, "An analysis of the duobinary technique," *IEEE Transactions on Communications*, vol. 14, no. 2, pp. 126–130, 1966.

[149] J. V. Kerrebrouck, J. Van Kerrebrouck, T. De Keulenaer, J. De Geest, R. Pierco, R. Vaernewyck, A. Vyncke, M. Fogg, M. Rengarajan, G. Torfs, and J. Bauwelinck, "100 Gb/s serial transmission over copper using duobinary signaling," in *DesignCon*, 2016.

[150] P. Dong, J. Lee, Y.-k. Chen, L. L. Buhl, S. Chandrasekhar, J. H. Sinsky, and K. Kim, "Four-channel 100-Gb/s per channel discrete multi-tone modulation using silicon photonic integrated circuits," in *Optical Fiber Communication Conference (OFC)*, p. Th5B.4, OSA, 2015.

[151] G. T. Reed, G. Mashanovich, F. Y. Gardes, and D. J. Thomson, "Silicon optical modulators," *Nature Photonics*, vol. 4, no. 8, pp. 518–526, 2010.

[152] T. Tekin, "Review of packaging of optoelectronic, photonic, and MEMS components," *IEEE Journal of Selected Topics in Quantum Electronics*, vol. 17, no. 3, pp. 704–719, 2011.

[153] L. Carroll, J.-S. Lee, C. Scarcella, K. Gradkowski, M. Duperron, H. Lu, Y. Zhao, C. Eason, P. Morrissey, M. Rensing, S. Collins, H. Hwang, and P. O'Brien, "Photonic packaging: Transforming silicon photonic integrated circuits into photonic devices," *Applied Sciences*, vol. 6, no. 12, p. 426, 2016.

[154] P. Elenius and L. Levine, "Comparing flip-chip and wire-bond interconnection technologies," *Chip Scale Review*, vol. 4, no. August, p. 81, 2000.

[155] D.-W. Kim, A. L. E. Jin, M. K. Raja, V. V. Kulkarni, L. C. Wai, J. L. T. Yang, and P. L. G. Qiang, “Compactly packaged high-speed optical transceiver using silicon photonics ICs on ceramic submount,” in *2016 IEEE 66th Electronic Components and Technology Conference (ECTC)*, pp. 1075–1080, IEEE, 2016.

[156] C. Doerr, J. Heanue, L. Chen, R. Aroca, S. Azemati, G. Ali, G. McBrien, L. Chen, B. Guan, H. Zhang, X. Zhang, T. Nielsen, H. Mezghani, M. Mihnev, C. Yung, and M. Xu, “Silicon photonics coherent transceiver in a ball-grid array package,” in *Optical Fiber Communication Conference (OFC)*, p. Th5D.5, OSA, 2017.

[157] A. Novack, M. Streshinsky, T. Huynh, T. Galfsky, H. Guan, Y. Liu, Y. Ma, R. Shi, A. Horth, Y. Chen, A. Hanjani, J. Roman, Y. Dziashko, R. Ding, S. Fathololoumi, A. E.-J. Lim, K. Padmaraju, R. Sukkar, R. Younce, H. Rohde, R. Palmer, G. Saathoff, T. Wuth, M. Bohn, A. Ahmed, M. Ahmed, C. Williams, D. Lim, A. Elmoznine, A. Rylyakov, T. Baehr-Jones, P. Magill, D. Scordo, and M. Hochberg, “A silicon photonic transceiver and hybrid tunable laser for 64 Gbaud coherent communication,” in *Optical Fiber Communication Conference Postdeadline Papers*, p. Th4D.4, OSA, 2018.

[158] C. Kopp, S. Bernabé, B. B. Bakir, J. Fedeli, R. Orobtchouk, F. Schrank, H. Porte, L. Zimmermann, and T. Tekin, “Silicon photonic circuits: On-CMOS integration, fiber optical coupling, and packaging,” *IEEE Journal of Selected Topics in Quantum Electronics*, vol. 17, no. 3, pp. 498–509, 2011.

[159] E. Higurashi, T. Imamura, T. Suga, and R. Sawada, “Low-temperature bonding of laser diode chips on silicon substrates using plasma activation of Au films,” *IEEE Photonics Technology Letters*, vol. 19, no. 24, pp. 1994–1996, 2007.

[160] S. Bernabe, B. Blampey, A. Myko, B. Charbonnier, K. Frigui, S. Bila, A. Mottet, J. Hauden, S. Jillard, B. Frigui, G. Duan, X. Pommarede, and G. Charlet, “Packaging of photonic integrated circuit based high-speed coherent transmitter module,” in *2016 IEEE 66th Electronic Components and Technology Conference (ECTC)*, pp. 1081–1086, IEEE, 2016.

[161] S. Bernabé, S. Olivier, A. Myko, M. Fournier, B. Blampey, A. Abraham, S. Menezo, J. Hauden, A. Mottet, K. Frigui, S. Ngoho, B. Frigui, S. Bila, D. Marris-Morini, D. Pérez-Galacho, P. Brindel, and G. Charlet,

"High-speed coherent silicon modulator module using photonic integrated circuits: from circuit design to packaged module," in *Proceedings of SPIE - The International Society for Optical Engineering*, vol. 9891, p. 98910Z, SPIE Photonics Europe, 2016.

[162] D. Celo, D. J. Goodwill, J. Jiang, P. Dumais, C. Zhang, F. Zhao, X. Tu, C. Zhang, S. Yan, J. He, M. Li, W. Liu, Y. Wei, D. Geng, H. Mehrvar, and E. Bernier, "32x32 silicon photonic switch," in *OptoElectronics and Communications Conference (OECC) held jointly with 2016 International Conference on Photonics in Switching (PS)*, pp. WF1–4, 2016.

[163] D. Vermeulen, R. Aroca, L. Chen, L. Pellach, G. McBrien, and C. Doerr, "Demonstration of silicon photonics push-pull modulators designed for manufacturability," *IEEE Photonics Technology Letters*, vol. 28, no. 10, pp. 1127–1129, 2016.

[164] C. Lacava, I. Cardea, I. Demirtzioglou, A. Khoja, L. Ke, D. J. Thomson, X. Ruan, F. Zhang, G. T. Reed, D. Richardson, and P. Petropoulos, "49.6 Gb/s direct detection DMT transmission over 40 km single mode fibre using an electrically packaged silicon photonic modulator," *Optics Express*, vol. 25, no. 24, p. 29798, 2017.

[165] X. Ruan, K. Li, D. J. Thomson, C. Lacava, F. Meng, I. Demirtzioglou, P. Petropoulos, Y. Zhu, G. T. Reed, and F. Zhang, "Experimental comparison of direct detection Nyquist SSB transmission based on silicon dual-drive and IQ Mach-Zehnder modulators with electrical packaging," *Optics Express*, vol. 25, no. 16, p. 19332, 2017.

[166] P. Dong, X. Liu, S. Chandrasekhar, L. L. Buhl, R. Aroca, and Y.-k. Chen, "Monolithic silicon photonic integrated circuits for compact 100+Gb/s coherent optical receivers and transmitters," *IEEE Journal of Selected Topics in Quantum Electronics*, vol. 20, no. 4, pp. 1–8, 2014.

[167] N. Qi, X. Xiao, S. Hu, X. Li, H. Li, L. Liu, Z. Li, N. Wu, and P. Y. Chiang, "Co-design and demonstration of a 25-Gb/s silicon-photonic Mach-Zehnder modulator with a CMOS-based high-swing driver," *IEEE Journal of Selected Topics in Quantum Electronics*, vol. 22, no. 6, pp. 131–140, 2016.

[168] Y. Ding, C. Peucheret, H. Ou, and K. Yvind, "Fully etched apodized grating coupler on the SOI platform with −0.58 dB coupling efficiency," *Optics Letters*, vol. 39, no. 18, p. 5348, 2014.

[169] N. Lindenmann, S. Dottermusch, M. L. Goedecke, T. Hoose, M. R. Billah, T. P. Onanuga, A. Hofmann, W. Freude, and C. Koos, "Connecting silicon photonic circuits to multicore fibers by photonic wire bonding," *Journal of Lightwave Technology*, vol. 33, no. 4, pp. 755–760, 2015.

[170] P.-I. Dietrich, M. Blaicher, I. Reuter, M. Billah, T. Hoose, A. Hofmann, C. Caer, R. Dangel, B. Offrein, U. Troppenz, M. Moehrle, W. Freude, and C. Koos, "In situ 3D nanoprinting of free-form coupling elements for hybrid photonic integration," *Nature Photonics*, vol. 12, no. 4, pp. 241–247, 2018.

[171] H. Zwickel, J. N. Kemal, C. Kieninger, Y. Kutuvantavida, M. Lauermann, J. Rittershofer, R. Pajković, D. Lindt, S. Randel, W. Freude, and C. Koos, "Electrically packaged silicon-organic hybrid modulator for communication and microwave photonic applications," in *Conference on Lasers and Electro-Optics*, p. SM3B.1, OSA, 2018.

[172] M. Billah, J. N. Kemal, M. Blaicher, Y. Kutuvantavida, C. Kieninger, H. Zwickel, P.-I. Dietrich, S. Wolf, T. Hoose, Y. Xu, U. Troppenz, M. Möhrle, S. Randel, W. Freude, and C. Koos, "Four-channel 784 Gbit/s transmitter module enabled by photonic wire bonding and silicon-organic hybrid modulators," in *European Conference on Optical Communication (ECOC)*, p. Th.PDP.C.1, 2017.

[173] M. J. Degerstrom, B. K. Gilbert, and E. S. Daniel, "Accurate resistance, inductance, capacitance, and conductance (RLCG) from uniform transmission line measurements," in *2008 IEEE-EPEP Electrical Performance of Electronic Packaging*, pp. 77–80, IEEE, 2008.

[174] F. J. Schmückle, R. Doerner, G. N. Phung, W. Heinrich, D. Williams, and U. Arz, "Radiation , multimode propagation , and substrate modes in W-band CPW calibrations," in *41st European Microwave Conference*, pp. 297–300, 2011.

[175] W. Freude, R. Schmogrow, B. Nebendahl, M. Winter, A. Josten, D. Hillerkuss, S. Koenig, J. Meyer, M. Dreschmann, M. Huebner, C. Koos, J. Becker, and J. Leuthold, "Quality metrics for optical signals: Eye diagram, Q-factor, OSNR, EVM and BER," in *International Conference on Transparent Optical Networks (ICTON)*, IEEE, 2012.

[176] L. M. Zhang and F. R. Kschischang, "Staircase codes with 6% to 33% overhead," *Journal of Lightwave Technology*, vol. 32, no. 10, pp. 1999–2002, 2014.

Glossary

List of Abbreviations

16QAM	16-state quadrature amplitude modulation
ADC	digital-to-analog converter
ASE	amplified spontaneous emission
AWG	arbitrary waveform generator
b2b	back-to-back
BEOL	back end of line
BER	bit error ratio
BERT	bit error ratio tester
BiCMOS	bipolar CMOS
BOX	burried-oxide-layer
BTO	barium titanate $BaTiO_3$
CMOS	complementary metal-oxide-semiconductor
CPU	central processing unit
DAC	digital-to-analog converter
DB	duobinary
DC	direct current
DLW	direct laser writing
DMT	discrete multitone
DOI	digital object identifier
DSP	digital signal processing

DUT	device under test
DUV	deep-UV
EAM	electro-absorption modulator
ECL	external cavity laser
EDB	electrical duobinary
EDFA	erbium-doped fiber amplifier
EIC	electronic integrated circuit
EO	electro-optic
EOE	electro-optic-electric
ER	extinction ratio
FCA	free-carrier absorption
FEC	forward-error correction
FEOL	front end of line
FFE	feed-forward equalizer
FOM	figure of merit
FPGA	field-programmable gate array
GSG	ground-signal-ground
IC	integrated circuit
IDB	intensity-modulated duobinary
IL	insertion loss
IoT	internet of things
IPQ	Institute of Photonics and Quantum Electronics
IQ	in-phase/quadrature-phase
ISI	inter-symbol interference
IM/DD	intensity-modulation and direct-detection
KIT	Karlsruhe Institute of Technology
LC	liquid crystal

MMA	methyl methacrylate
MMI	multi-mode-interference
MUX	multiplexer
MZI	Mach-Zehnder interferometer
MZM	Mach-Zehnder modulator
NRZ	non-return-to-zero
ODB	optical duobinary
OFDM	orthogonal frequency multiplexing
OLED	organic light-emitting diode
OOK	on-off-keying
PAM4	four-level pulse-amplitude modulation
PCB	printed circuit board
PD	photodiode
PDM	polarization division multiplexing
PIC	photonic integrated circuit
PIN	p-doped-intrinsic-n-doped
POH	plasmonic-organic hybrid
PPG	pulse pattern generator
PR	partial response
PRBS	pseudo-random binary sequences
PVT	phenyl vinylene thiophene
PZT	lead zirconate titanate
QAM	quadrature amplitude modulation
QPSK	quadrature-phase-shift-keying
RF	radio frequency
SFP	small formfactor pluggable

SI	International System of Units (abbreviated from the French Système international (d'unités))
SiP	silicon photonics
SIS	silicon-insulator-silicon
SISCAP	silicon-insulator-silicon capacitor
SMD	surface mount device
SNR	signal-to-noise-ratio
SOH	silicon-organic hybrid
SOI	silicon-on-insulator
SOLT	short-open-load-through
SSMF	standard single-mode fiber
TL	transmission line
TPA	two-photon absorption
TW	traveling wave
VNA	vector network analyzer
VCSEL	vertical-cavity surface-emitting laser
WDM	wavelength-division multiplexing

List of symbols

Uppercase

$A(t)$ complex amplitude

BER bit error ratio

C capacitance

C' capacitance per infinitesimal length Δz; $C' = C/\Delta z$

D dispersion coefficient

E electric field

G conductance

G' conductance per infinitesimal length Δz; $G' = G/\Delta z$

I current or I-component of an IQ-signal

I_p photocurrent

I_opt intensity of an optical signal

L inductance

L' inductance per infinitesimal length Δz; $L' = L/\Delta z$

M number of symbols

N number density of chromophores

N_e free electron concentration

N_h free hole concentration

P power

Q Q-factor or Q-component of an IQ-signal

R ohmic resistance

R' resistance per infinitesimal length Δz; $R' = R/\Delta z$

R_trm terminating resistance

R_src source resistance

$\mathbf{S}$ S-parameter matrix

SNR signal-to-noise power ratio

$\mathbf{T}$ transmission matrix ($ABCD$-matrix)

T_g glass-transition temperature

U voltage

U_π π-voltage of an MZM

W_bit energy dissipated, e.g. in an EO modulator, per bit

Y admittance

Y' admittance per infinitesimal length Δz; $Y' = Y/\Delta z$

Z_0 characteristic impedance

Z_in input impedance

Z_L load impedance

Z_ref reference impedance (usually $50\,\Omega$)

Z_src source impedance

Z_trm impedance of termination

Lowercase

$a^{(\mathrm{IL})}$ optical insertion loss expressed in dB

a power propagation loss expressed in dB/m

a_k symbol

c speed of light in vacuum (SI defined constant)

d distance between electrodes

e elementary charge (SI defined constant)

f_d data rate

g Lorentz-Onsager local field factor

f_s symbol rate

m number of bits

m_e^* electron conductivity effective mass

m_h^* hole conductivity effective mass

n refractive index

$n_\mathrm{g,opt}$ effective group-refractive index of a waveguide mode

$\hbar$ reduced Planck constant (SI defined constant)

i time dependent current

j imaginary unit

k wave number, $k = 2\pi/\lambda$

ℓ length of a transmission line or a traveling wave modulator

m_PH frequency response of a phase modulator

m_EOE small-signal intensity frequency response of an MZM modulator

$\mathbf{p}$ molecular dipole moment

$p(t)$ time-domain pulse shape

r_{33} EO coefficient

$s(t)$ signal

t time

u time dependent voltage

v_g group velocity

Greek symbols and variables

α real part of propagation parameter γ

$\alpha^{(\mathrm{pwr})}$ power attenuation parameter expressed in 1/m, $\alpha^{(\mathrm{pwr})} = 2\alpha$

$\alpha^{(\mathrm{c})}$ chirp parameter

$\alpha^{(\mathrm{fs})}$ fine-structure constant, $\alpha^{(\mathrm{fs})} = \mathrm{e}^2/4\pi\epsilon_0\hbar\mathrm{c}$

$\check{\alpha}$ first-order polarizability

β imaginary part of propagation parameter γ

$\check{\beta}$ microscopic nonlinearity of EO molecules

$\beta^{(\mathrm{ro})}$ roll-off factor

γ complex propagation parameter (propagation "constant"), $\gamma = \alpha + \mathrm{j}\beta$

Γ reflection coefficient

ϵ_0 vacuum electric permittivity constant (electrical constant), $\epsilon_0 = 1/\mu_0\mathrm{c}^2$

λ medium wavelength

λ_0 vacuum wavelength

μ_0 vacuum magnetic permeability constant (magnetic constant), $\mu_0 = 4\pi\alpha^{(\mathrm{fs})}\hbar/(\mathrm{e}^2\mathrm{c})$

μ_e electron mobility

μ_h hole mobility

$\check{\mu}$ molecular electric-dipole moment

π "pi", Archimedes' constant

ρ electrical resistivity

φ, ϕ phase

$\hat{\varphi}$ complex amplitude of time dependent phase shift

$\chi^{(n)}$ nth-order susceptibility

ω angular frequency

ω_RF angular frequency of an RF signal

Danksagung

Die vorliegende Dissertation entstand während meiner Tätigkeit am Institut für Photonik und Quantenelektronik (IPQ) am Karlsruher Institut für Technologie (KIT). Die wissenschaftliche Arbeit war eingebettet in die öffentlich geförderten Forschungsprojekte PhoxTroT und BigPipes, beide gefördert von der Europäischen Union (EU) sowie das Projekt HIPES, gefördert vom Bundesministerium für Bildung und Forschung (BMBF).

Eine Vielzahl an Personen hat mich in der Entstehung der vorliegenden Arbeit unterstützt und diese ermöglicht. Ihnen allen gilt mein herzlicher Dank. Einigen möchte ich an dieser Stelle meinen ganz besonderen Dank entgegenbringen.

Meinem Doktorvater Professor Christian Koos möchte ich besonders für das mir entgegengebrachte Vertrauen danken. Seine Ideen, Vorschläge und Ratschläge haben wesentlich zur Entstehung dieser Arbeit beigetragen. Ich konnte sehr viel von ihm lernen und seine schnelle Auffassungsgabe hat mich immer wieder erstaunt. Häufig konnte er mir schon mit einer Antwort weiterhelfen, ehe ich in der Lage war, die Frage verständlich zu formulieren.

Herrn Professor Wolfgang Freude gilt mein herzlicher Dank für die geduldige Durchsicht meiner Arbeiten und die offenen und fruchtbaren Diskussionen sowie die wertvolle Kritik und Ermutigung. Seine konsequente Arbeitsweise hat mich inspiriert und ich bin dankbar, dass ich mit ihm zusammenarbeiten durfte.

Herrn Professor Thomas Zwick danke ich herzlich für die gute Zusammenarbeit und besonders für die Betreuung als Korreferent.

Ganz besonderer Dank gilt meinem Kollegen Stefan Wolf, der in meiner Anfangszeit sowohl fachlich als auch menschlich eine große Unterstützung war. Ebenso großer Dank gebührt Clemens Kieninger, der seit dem ersten Semester eine wichtige Stütze für mich ist. Es war fantastisch, dass wir nun auch als Kollegen am IPQ eng zusammenarbeiten konnten. Ihm und Yasar Kutuvantavida danke ich insbesondere für die tatkräftige Unterstützung beim Herstellen der SOH Proben. Matthias Lauermann danke ich dafür, dass er mir

das Forschungsthema der SOH-Modulatoren ebenso wie zahlreiche Proben in tadellosem Zustand überlassen hat.

Auch Tobias Harter danke ich besonders für seine außerordentliche Unterstützung auch außerhalb des IPQ. Ihm, Clemens Kieninger, Philipp Trocha, Christoph Füllner und Stefan Singer danke ich ganz besonders für die besonders enge Zusammenarbeit am IPQ, auf Summer Schools, privat oder beim alljährlichen Kampf mit der HLB Klausur. Juned Nassir Kemal gilt mein besonderer Dank für seine Unterstützung bei vielen Messungen und für seine Begleitung auf der Reise durch Kalifornien. Andrea Riemensperger danke ich besonders für die Unterstützung bei der Organisation zahlreicher Förderanträge und Projekte. Tatiana Gassmann danke ich besonders für die Organisation von allem was mit HLB zu tun hat. Oswald Speck danke ich besonders für die Unterstützung in der Aufbau- und Verbindungstechnik. Marco Hummel, Martin Winkeler und Andreas Lipp danke ich für die Anfertigung von allerlei elektronischen und feinmechanischen Aufbauten. David Guder danke ich für den exzellenten IT Support und die quasi augenblickliche und pragmatische Lösung vieler Probleme. Maria-Luise Koch und Bernadette Lehmann danke ich für ihre Unterstützung bei sämtlichen administrativen Herausforderungen. Professor Sebastian Randel danke ich für die kritische Durchsicht meiner Manuskripte und die lehrreichen Erläuterungen zur Nachrichtentechnik und Signalprozessierung.

Meinen Kollegen Tobias Hoose, Matthias Blaicher, Sentayehu Wondimu, Sascha Mühlbrandt, Simon Schneider, Claudius Weimann, Nicole Lindenmann, Jörg Pfeifle, Norbert Schneider, Wladislaw Hartmann, Manfred Hirsch, Kira Köhnle, Carsten Eschenbaum, Lothar Hahn, Adib Md Mosaddek Hossain, Muhammad Rodlin (Oding) Billah, Philipp-Immanuel Dietrich, Dengyang Fang, Denis Ganin, Tilahun Gutema, Daria Kohler, Alexander Kotz, MD Salek Mahmut, Pascal Maier, Pablo Marin-Palomo, Aleksandar Nesic, Mareike Trappen, Sandeep Ummethala und Yilin Xu gebührt ebenso mein großer Dank. Sie alle haben die Arbeit am Institut ausgemacht, ich konnte viel von ihnen lernen und es war großartig, die Zeit mit ihnen zu verbringen.

Christian von Vangerow, Christian Bohn, Florian Boes und Professor Thomas Zwick danke ich für die gute Zusammenarbeit, unter anderem im HIPES Projekt. Professor Shiyoshi Yokoyama und seiner Arbeitsgruppe danke ich für die gute Zusammenarbeit und die Bereitstellung von exzellenten organischen elektro-optischen Materialien.

Ich danke Daniel Lindt, Rastko Pajković, Jonas Rittershofer, Daniel Gil und Narek Muradyan, deren Abschlussarbeit ich betreuen durfte, für ihre Arbeit. Herzlichen Dank auch an Julian Töpfer und Ahmed Shariful Alam für die ausgezeichnete Arbeit als HiWi. Sie alle haben durch ihre Arbeiten auch zu den Erfolgen der vorliegenden Arbeit beigetragen.

Vielen Dank an Julia Haug, Tobias Harter, Clemens Kieninger, Carsten Eschenbaum und Philipp Trocha für das Korrekturlesen in letzter Minute.

Großer Dank gilt meinen Freunden aus Schopfheim und Karlsruhe, die mich seit Jahren begleiten. Ohne sie wäre vieles nicht möglich und unter anderem diese Arbeit nicht entstanden.

Ganz besonderer Dank gilt meinen Eltern und meiner Schwester. Danke, dass ihr mich immer, bei allem was ich tat oder seinließ, unterstützt habt, hinter mir steht und so vieles erst ermöglicht habt. Ebenso danke ich meinen Großeltern, die mich stets sehr interessiert begleitet und unterstützt haben.

Tausend Dank an Julia! Danke, dass du auf unserem gemeinsamen Weg auch die Last dieser Arbeit mitgetragen hast und so viel Verständnis gezeigt und mich unterstützt hast.

List of publications

Journal publications

[J1] **H. Zwickel**, S. Singer, C. Kieninger, Y. Kutuvantavida, N. Muradyan, T. Wahlbrink, S. Yokoyama, S. Randel, W. Freude, and C. Koos, “A verified equivalent-circuit model for slot-waveguide modulators,” *Optics Express*, vol. 28, no. 9, pp. 12951–12976, 2020.
DOI: `https://doi.org/10.1364/OE.383120`.

[J2] **H. Zwickel**, S. Wolf, C. Kieninger, Y. Kutuvantavida, M. Lauermann, T. de Keulenaer, A. Vyncke, R. Vaernewyck, J. Luo, A. K.-Y. Jen, W. Freude, J. Bauwelinck, S. Randel, and C. Koos, “Silicon-organic hybrid (SOH) modulators for intensity-modulation/direct-detection links with line rates of up to 120 Gbit/s,” *Optics Express*, vol. 25, no. 20, pp. 23784–23800, 2017.
DOI: `https://doi.org/10.1364/OE.25.023784`.

[J3] **H. Zwickel**, J. N. Kemal, C. Kieninger, Y. Kutuvantavida, J. Rittershofer, M. Lauermann, W. Freude, S. Randel, and C. Koos, “Electrically packaged silicon-organic hybrid (SOH) I/Q-modulator for 64 GBd operation,” *Optics Express*, vol. 26, no. 26, pp. 34580–34591, 2018.
DOI: `https://doi.org/10.1364/OE.26.034580`.

[J4] S. Wolf†, **H. Zwickel**†, W. Hartmann†, M. Lauermann, Y. Kutuvantavida, C. Kieninger, L. Altenhain, R. Schmid, J. Luo, A. K. Y. Jen, S. Randel, W. Freude, and C. Koos, “Silicon-organic hybrid (SOH) Mach-Zehnder modulators for 100 Gbit/s on-off keying,” *Scientific Reports*, vol. 8, no. 1, p. 2598, 2018.
† **authors contributed equally to the work**
DOI: `https://doi.org/10.1038/s41598-017-19061-8`.

[J5] S. Wolf, **H. Zwickel**, C. Kieninger, M. Lauermann, W. Hartmann, Y. Kutuvantavida, W. Freude, S. Randel, and C. Koos, “Coherent modulation up to 100 GBd 16QAM using silicon-organic hybrid (SOH)

devices," *Optics Express*, vol. 26, no. 1, p. 220, 2018.
DOI: `https://doi.org/10.1364/OE.26.000220`.

[J6] S. Gudyriev, C. Kress, **H. Zwickel**, J. N. Kemal, S. Lischke, L. Zimmermann, C. Koos, and J. C. Scheytt, "Coherent ePIC receiver for 64 GBaud QPSK in 0.25 µm photonic BiCMOS technology," *Journal of Lightwave Technology*, vol. 37, no. 1, pp. 103–109, 2019.
DOI: `https://doi.org/10.1109/JLT.2018.2881107`.

[J7] W. Heni, Y. Kutuvantavida, C. Haffner, **H. Zwickel**, C. Kieninger, S. Wolf, M. Lauermann, Y. Fedoryshyn, A. F. Tillack, L. E. Johnson, D. L. Elder, B. H. Robinson, W. Freude, C. Koos, J. Leuthold, and L. R. Dalton, "Silicon-organic and plasmonic-organic hybrid photonics," *ACS Photonics*, vol. 4, no. 7, pp. 1576–1590, 2017.
DOI: `https://doi.org/10.1021/acsphotonics.7b00224`.

[J8] T. Hoose, M. Blaicher, J. Nassir Kemal, **H. Zwickel**, M. Rodlin Billah, P.-I. Dietrich, A. Hofmann, W. Freude, S. Randel, and C. Koos, "Hardwire-configurable photonic integrated circuits enabled by 3D nano-printing," *submitted for publication*, 2019. preprint available: arXiv:1912.09942
DOI: `https://arxiv.org/abs/1912.09942`.

[J9] C. Kieninger, Y. Kutuvantavida, D. L. Elder, S. Wolf, **H. Zwickel**, M. Blaicher, J. N. Kemal, M. Lauermann, S. Randel, W. Freude, L. R. Dalton, and C. Koos, "Ultra-high electro-optic activity demonstrated in a silicon-organic hybrid modulator," *Optica*, vol. 5, no. 6, pp. 739–748, 2018.
DOI: `https://doi.org/10.1364/OPTICA.5.000739`.

[J10] C. Kieninger, Y. Kutuvantavida, H. Miura, J. N. Kemal, **H. Zwickel**, F. Qiu, M. Lauermann, W. Freude, S. Randel, S. Yokoyama, and C. Koos, "Demonstration of long-term thermally stable silicon-organic hybrid modulators at 85°C," *Optics Express*, vol. 26, no. 21, pp. 27955–27964, 2018.
DOI: `https://doi.org/10.1364/OE.26.027955`.

[J11] M. Lauermann, S. Wolf, W. Hartmann, R. Palmer, Y. Kutuvantavida, **H. Zwickel**, A. Bielik, L. Altenhain, J. Lutz, R. Schmid, T. Wahlbrink, J. Bolten, A. L. Giesecke, W. Freude, and C. Koos, "Generation of 64 GBd 4ASK signals using a silicon-organic hybrid modulator at 80°C," *Optics Express*, vol. 24, no. 9, pp. 9389–9396, 2016.
DOI: `https://doi.org/10.1364/OE.24.009389`.

Conference publications

[C1] S. Ummethala, J. N. Kemal, M. Lauermann, A. S. Alam, **H. Zwickel**, T. Harter, Y. Kutuvantavida, L. Hahn, S. H. Nandam, D. L. Elder, L. R. Dalton, W. Freude, S. Randel, and C. Koos, "Capacitively coupled silicon-organic hybrid modulator for 200 Gbit/s PAM-4 signaling," in *Conference on Lasers and Electro-Optics*, p. JTh5B.2, Optical Society of America, 2019.

[C2] C. v. Vangerow, C. Bohn, **H. Zwickel**, C. Koos, and T. Zwick, "50 Gbit/s PAM-4 driver circuit based on variable gain distributed power combiner," in *2019 IEEE 19th Topical Meeting on Silicon Monolithic Integrated Circuits in RF Systems (SiRF)*, pp. 1–3, Jan 2019.

[C3] T. Hoose, M. Blaicher, J. N. Kemal, **H. Zwickel**, M. R. Billah, P. Dietrich, A. Hofmann, W. Freude, S. Randel, and C. Koos, "Hardwired configurable photonic integrated circuits enabled by 3D nanoprinting," *2018 European Conference on Optical Communication (ECOC)*, pp. 1–3, 2018.

[C4] C. Koos, S. Randel, W. Freude, L. R. Dalton, S. Wolf, C. Kieninger, Y. Kutuvantavida, M. Lauermann, D. L. Elder, S. Muehlbrandt, **H. Zwickel**, A. Melikyan, T. Harter, S. Ummethala, M. R. Billah, M. Blaicher, P.-I. Dietrich, and T. Hoose, "Hybrid photonic integration and plasmonic devices: New perspectives for high-speed communications and ultra-fast signal processing," in *CLEO Pacific Rim Conference 2018*, p. W4J.1, Optical Society of America, 2018.

[C5] C. Kieninger, Y. Kutuvantavida, J. N. Kemal, **H. Zwickel**, H. Miura, S. Randel, W. Freude, S. Yokoyama, and C. Koos, "Demonstration of long-term thermal stability of a silicon-organic hybrid (SOH) modulator at 85°C," in *Conference on Lasers and Electro-Optics*, p. SM3B.3, Optical Society of America, 2018.

[C6] **H. Zwickel**, J. N. Kemal, C. Kieninger, Y. Kutuvantavida, M. Lauermann, J. Rittershofer, R. Pajković, D. Lindt, S. Randel, W. Freude, and C. Koos, "Electrically packaged silicon-organic hybrid modulator for communication and microwave photonic applications," in *Conference on Lasers and Electro-Optics*, p. SM3B.1, Optical Society of America, 2018. (invited).

[C7] C. Kress, S. Gudyriev, **Heiner Zwickel**, J. N. Kemal, S. Lischke, L. Zimmermann, C. Koos, and J. C. Scheytt, "64 GBd monolithically integrated coherent QPSK single polarization receiver in 0.25 µm SiGe-photonic technology," in *Optical Fiber Communication Conference Postdeadline Papers*, p. Th4A.6, Optical Society of America, 2018.

[C8] M. R. Billah, J. N. Kemal, P. Marin-Palomo, M. Blaicher, Y. Kutuvantavida, C. Kieninger, **H. Zwickel**, P. . Dietrich, S. Wolf, T. Hoose, Y. Xu, U. Troppenz, M. Moehrle, S. Randel, W. Freude, and C. Koos, "Four-channel 784 Gbit/s transmitter module enabled by photonic wire bonding and silicon-organic hybrid modulators," in *2017 European Conference on Optical Communication (ECOC)*, pp. 1–3, Sep. 2017.

[C9] C. Kieninger, Y. Kutuvantavida, **H. Zwickel**, S. Wolf, M. Lauermann, D. L. Elder, L. R. Dalton, W. Freude, S. Randel, and C. Koos, "Record-high in-device electro-optic coefficient of 359 pm/V in a silicon-organic hybrid (SOH) modulator," in *Conference on Lasers and Electro-Optics*, p. STu3N.2, Optical Society of America, 2017.

[C10] M. R. Billah, M. Blaicher, J. N. Kemal, T. Hoose, **H. Zwickel**, P.-I. Dietrich, U. Troppenz, M. Moehrle, F. Merget, A. Hofmann, J. Witzens, S. Randel, W. Freude, and C. Koos, "8-channel 448 Gbit/s silicon photonic transmitter enabled by photonic wire bonding," in *Optical Fiber Communication Conference Postdeadline Papers*, p. Th5D.6, Optical Society of America, 2017.

[C11] S. Wolf, **H. Zwickel**, C. Kieninger, Y. Kutuvantavida, M. Lauermann, J. Lutz, L. Altenhain, R. Schmid, W. Freude, C. Koos, and S. Randel, "Silicon-organic hybrid (SOH) IQ modulator for 100 GBd 16QAM operation," in *Optical Fiber Communication Conference Postdeadline Papers*, p. Th5C.1, Optical Society of America, 2017.

[C12] **H. Zwickel**, T. D. Keulenaer, S. Wolf, C. Kieninger, Y. Kutuvantavida, M. Lauermann, M. Verplaetse, R. Pierco, R. Vaernewyck, A. Vyncke, X. Yin, G. Torfs, W. Freude, E. Mentovich, J. Bauwelinck, and C. Koos, "100 Gbit/s serial transmission using a silicon-organic hybrid (SOH) modulator and a duobinary driver IC," in *Optical Fiber Communication Conference*, p. W4I.5, Optical Society of America, 2017.

[C13] C. Koos, W. Freude, J. Leuthold, L. R. Dalton, S. Wolf, S. Muehlbrandt, A. Melikyan, **H. Zwickel**, T. Harter, Y. Kutuvantavida, C. Kieninger, M. Lauermann, and D. Elder, "Nanophotonic modulators and photodetectors using silicon photonic and plasmonic device concepts," in *SPIE OPTO 2017*, vol. 10098, 2017.

[C14] S. Wolf, W. Hartmann, M. Lauermann, **H. Zwickel**, Y. Kutuvantavida, C. Kieninger, W. Freude, and C. Koos, “High-speed silicon-organic hybrid (SOH) modulators,” in *ECOC 2016; 42nd European Conference on Optical Communication*, pp. 1–3, Sep. 2016. (invited).

[C15] **H. Zwickel**, S. Wolf, Y. Kutuvantavida, C. Kieninger, M. Lauermann, W. Freude, and C. Koos, “120 Gbit/s PAM-4 signaling using a silicon-organic hybrid (SOH) Mach-Zehnder modulator,” in *ECOC 2016; 42nd European Conference on Optical Communication*, pp. 1–3, Sep. 2016.

[C16] C. Koos, W. Freude, L. Dalton, T. J. Kippenberg, L. P. Barry, A. Ramdane, F. Lelarge, S. Wolf, **H. Zwickel**, M. Lauermann, C. Weimann, W. Hartmann, J. N. Kemal, P. Marin, P. Trocha, J. Pfeifle, T. Herr, V. Brasch, R. T. Watts, D. Elder, A. Martinez, V. Panapakkam, and N. Chimot, “Silicon-organic hybrid (SOH) devices and their use in comb-based communication systems,” in *2016 IEEE 13th International Conference on Group IV Photonics (GFP)*, pp. 56–57, Aug 2016.

[C17] C. Koos, W. Freude, J. Leuthold, L. R. Dalton, S. Wolf, **H. Zwickel**, T. Hoose, M. R. Billah, M. Lauermann, C. Weimann, W. Hartmann, A. Melikyan, N. Lindenmann, S. Koeber, R. Palmer, D. Korn, L. Alloatti, A. L. Giesecke, and T. Wahlbrink, “Silicon-organic hybrid (SOH) integration and photonic multi-chip systems: Technologies for high-speed optical interconnects,” in *2016 IEEE Optical Interconnects Conference (OI)*, pp. 86–87, May 2016.

[C18] S. Wolf, M. Lauermann, W. Hartmann, **H. Zwickel**, Y. Kutuvantavida, M. Koenigsmann, M. Gruen, J. Luo, A. K.-Y. Jen, W. Freude, and C. Koos, “An energy-efficient 252 Gbit/s silicon-based IQ-modulator,” in *Optical Fiber Communication Conference*, p. Th3J.2, Optical Society of America, 2016.

[C19] W. Hartmann, M. Lauermann, S. Wolf, **H. Zwickel**, Y. Kutuvantavida, J. Luo, A. K. . Jen, W. Freude, and C. Koos, “100 Gbit/s OOK using a silicon-organic hybrid (SOH) modulator,” in *2015 European Conference on Optical Communication (ECOC)*, pp. 1–3, Sep. 2015.